„Microscopic heterogeneities and macroscopic physical properties in filled elastomers“

Von der Fakultät für Mathematik, Informatik und Naturwissenschaften der RWTH Aachen University zur Erlangung des akademischen Grades eines Doktors der Naturwissenschaften genehmigte Dissertation

vorgelegt von

Master of Science

Robert Ferencz

aus Bistrița, Rumänien

Berichter: Prof. Dr. Bernhard Blümich

Dr. Wolfram Herrmann

Tag der mündlichen Prüfung: 12.11.2013

Microscopic heterogeneities and macroscopic physical properties in filled elastomers.

Von der Fakultät für Mathematik, Informatik und Naturwissenschaften der RWTH Aachen

Universität zur Erlangung des akademischen Grades eines

Doktors der Naturwissenschaften genehmigte Dissertation

vorgelegt von

Master of Science

Robert Ferencz

geboren am 11. September 1982 in Bistrița, Rumänien

Berichter: Prof. Dr. Dr. h.c. Bernhard Blümich

Dr. Wolfram Herrmann

Tag der mündlichen Prüfung: 12.11.2013

“Always aim for the moon, even if you miss, you'll land among the stars.”

(W. Clement Stone)

Acknowledgements

I would like to thank my advisors Prof. Dr. Bernhard Blümich and Dr. Wolfram Herrmann for all their support over the years. They have been a great intellectual resource. I would especially like to recognize Dr. Wolfram Herrmann for all the work he does as an instructor, an advisor and coordinator. The R&D Materials Department at ContiTech Hannover has been a wonderful place to call home. This is due in part to the tremendous contributions of an individual who has made my time here run much more smoothly. Dr. Jorge Sanchez has been a big resource for equipment and practical knowledge; thank you Jorge for all of your help.

I would like to thank to all friends who contributed directly or indirectly with ideas and suggestions that helped me during my time spent as a Ph.D student. I owe Cristina Gruian special thanks for helping me to improve the grammar and spelling of this thesis.

At least but not last I do not know if I can articulate the importance of my relationship with my wife and friend Alexandra Ferencz. She has helped to keep me sane when all others had lost all hope. She has been a sounding board when I need it most. She has reminded me of who I am when I no longer remember. She has been the definition of a true friend.

List of symbols

θ	Poisson's ratio
A	Area
D	Distance
E	Young's modulus
F	Force
G	Shear modulus
k_c	Spring constant
L -	Length
S	Stiffness
t_c	Cantilever thickness
w	Width
Z_c	Static cantilever deflection
Z_p	Distance between the sample surface and the cantilever rest position
δ	Deformation
σR	Tensile strength

List of abbreviations

AC	Alternative curent
AFM	Atomic Force Microscope
BR	Polybutadiene rubber
DCP	Dicyclopentadiene
DMA	Dynamic Mechanical Analysis
DSC	Differential Scanning Calorimetry
ENB	Ethylidene norbornene
EPDM	Ethylene propylene diene monomer
EPM	Ethylene propylene rubber
F-D	Force-Distance curve
FEM	Field Emission Microscopy
FHC100	Filled highly crystalline polymer cured to 100%
FHC50	Filled highly crystalline polymer cured to 50%
FLC100	Filled amorphous polymer cured to 100%
FLC50	Filled amorphous polymer cured to 50%
HX	Trans-1,4 Hexadiene
MI	Maximum Indentation
MW	Molecular weight
NMR	Nuclear Magnetic Resonance
MOUSE	Mobile Universal Surface Explorer
NR	Natural rubber
phr	Parts per Hundred Rubber
RPA	Rubber Process Analyzer
SBR	Styrene-butadiene rubber
SEM	Scanning Electron Microscope
SFA	Surface Force Apparatus
SNOM	Scanning Near-field Optical Microscope

SPM	Scanning Probe Microscope
SSBR	Solution Styrene Butadiene Rubber
STM	Scanning Tunnelling Microscope
TEOS	Ttetraethyl orthosilicate
TESPT	3-Triethoxysilypropil tetrasulphane
UV	Ultraviolet light

Table of contents

1. Introduction

Perhaps one of the most decisive aspects of the humankind evolution is its curiosity, a drive to know, to learn new things; to observe how thinks work, to find out "what lies behind that corner"; a drive to adapt to new situations, new environments, to make mistakes and learn from them. This drive allowed the humankind to evolve, to search for solutions that could make life easier. The man discovered that the nature can support him with "raw materials" which he later used them to build houses, weapons, ships etc. Then, he discovered that he is not alone, that there are continents and seas, that the world is spherical. When the world was completely known, he decided to look what is beyond the globe, so he did the first step on the moon. Further on, he realized that it is of the same importance to investigate the opposite scale as well, to see and understand what the materials consist of and how can be better combined to achieve superior materials that are designed to help him on his path. Thus, was raised the constant need to understand how things work at small scales, to be able to produce at bigger scales.

Perhaps one of the most precious raw material that the men discovered during his expansion was rubber. The first attempts to use rubber in industrial purposes were failures since the cold weather transformed the goods into brittle materials, while storage in the sun or at higher temperatures leads to tendency to gum together. The accidental discovery of the vulcanization by Charles Goodyear in 1839 [1] was followed by an industrial boom in the rubber industry.

Since then, rubber became an indispensable material in almost all industries (automobile, aerospace, household etc.). The rubbery materials reinforced with fillers were able to fulfill a wide range of applications such as tires, hoses, belts, transport bands etc. Reinforced rubber

products combine the properties of rubbers and the reinforcing materials together, so high strength materials with a proper flexibility can be obtained. The reinforcing materials, usually carbon black or silica based fillers, provide the strength and stiffness of the composite. Filled elastomer materials are nearly a precondition to produce rubber products for the well known applications.

The interaction that governs such composites can be mainly classified in filler-filler interactions and polymer-filler interactions. Filler-filler interactions were first experimentally evidenced by Payne in 1962 (known as Payne effect) [2]. He demonstrated that under dynamic cyclical stress experiments the storage modulus of reinforced rubber material decreases with increasing the amplitude of the oscillation. This behaviour was attributed to the destruction of the existing filler-filler networks. Accordingly, bound rubber is considered as a macroscopic result of rubber-filler interaction [3]. The polymer chains are trapped between the filler particles by chemical or physical bonds, conferring to the composite material an additive reinforcement.

Due to nowadays standards in high performance materials, the requirements from such materials are always increasing. Having new materials developed, they also require new or improved testing methods. So, the development of new materials attracts the development of new testing techniques as well.

As a tribute to the trend of building smaller and smaller parts, the understanding of the micromechanical behaviour of size reduced materials has become a necessity. A view at a reduced scale may reveal material properties different from those of the bulk state. For example standard hardness measurements can be adjusted to nanoindentation measurements, and heterogeneities at nanoscales can be mapped. It is of critical importance to locate the nanoscale heterogeneities, to accurately be able to predict the behaviour of the bulk material.

This thesis focuses on the development of new testing method, applicable to the characterization of elastomers, i.e. filled rubber composites. AFM nanoindentation is used as a method to determine micromechanical properties of polymers. It is generally accepted that the shape of the tip during a standard AFM experiment changes. Since the shape defines the projected contact area, it is a parameter that is directly proportional to the elastic modulus. Any change of the shape of the indenter affects the accuracy of the results. The method suggested in the present work relies on the introduction of an experimentally determined tip-area function. Values for Young's modulus were calculated for samples with different degrees of curing and different degrees of crystallinity.

Mappings of E-modulus with micrometer scaling were generated using the above described procedure. As an application, the method is suited for characterization of mechanical properties of rubber composites at micro and nanoscales. Filler dispersion heterogeneities could be observed even when macroscopic standard physical tests show no or minimal differences.

The procedure of determining the E-modulus using AFM nanoindentation is described in chapter 2, together with the theory regarding the Atomic Force Microscopy (AFM). Force-distance curves and the properties extracted from such curves are also explained. Special attention was directed to the estimation of the shape of the tip on a cantilever. We were able to evidence that any change in the tip shape results in strong deviations of the calculated moduli. For comparison with AFM nanoindentation, the Profile NMR MOUSE (Mobile Universal Surface Explorer) is described in Chapter 3. The next chapter, 4, describes shortly the theory behind the interactions that occur in a filled rubber material.

The materials used in this work, together with the influence of tips and sample preparation on the obtained results, are described in the experimental section of the thesis (Chapter 5).

Chapter 6 focuses on the development of a new testing method to determine the E-modulus of elastomers at nano- and micrometer scales. Thus, it was shown that the moduli calculated from single force curves performed over soft areas of the sample (polymer matrix) are comparable to the values obtained by DMA measurements upon extrapolation to zero amplitude.

Issues concerning heterogeneities induced in filled EPDM elastomers are further presented in Chapter 7. Thereby, mappings of E-Moduli with 2 micrometers scales were acquired by using the method described in the previous chapter. Even the hard structures (represented by the filler agglomerates, and crystallites) could be considered in the E-modulus correlation with the DMA through an average value. As before, extrapolating the moduli calculated from AFM to zero amplitude gives values comparable to the ones measured by DMA.

Chapter 8 is focused on the development of a new material with barrier effects, which can be used in applications such as hoses, where the permeability of the rubber matrix pays an important role. These effects were investigated with both, AFM and NMR techniques, and a good correlation between the results obtained with these two methods could be observed.

2. Background information

2.1 Atomic Force Microscopy (AFM)

The invention of the scanning tunnelling microscope (STM) in 1981 by Bining et al. [4] improved significantly the resolution of microscopic techniques. Images of conducting and semiconducting materials with atomic resolution were reported for the first time. As a consequence, a series of scanning probe microscopes (SPM) were invented in the 1980s. STM was shortly followed in 1984 by developing of scanning near-field optical microscope (SNOM), which allowed microscopy with light acquisitions to range above the optical resolution limit [5-7]. In 1986 Binning and his co-workers [5, 8], invented the **atomic force microscope (AFM)**. Instrumental improvements and novel applications of AFM have broadened very fast in the last twenty years, so that different AFM techniques became important tools to study local nano- and micromechanical properties by means of force-distance (FD) curves [5, 9]. AFM allows to obtain images of the sample surfaces using a physical probe (very sharp tip with radius of 10 nm), by moving the sample in a raster scan and recording the tip-sample interactions as a function of the location.

Contrary to STM, which senses the tunnelling current between the conducting tip and the specimen, AFM can be used also to analyze non-conducting materials, such as polymers and biological samples [9-11]. Forces order of 10^{-12} to 10^{-4} N magnitude order can be measured with a lateral resolution of several Angstroms [12].

From the very first time it was obvious that AFM was not only able to map the sample topography but also to detect a variety of different forces, such adhesion and repulsive forces, van der Waals, magnetic, electrostatic and frictional forces [9-11].

A few other methods can be used to study the surface interaction, one of the most popular being the surface force apparatus (SFA) [13]. SFA has a vertical resolution of 0.1 nm and a force resolution of 10 nN. Although it can only be used on surfaces of known geometry, it leads to precise measurements of surface and force energies [9]. However, only a limited number of systems could be investigated because of the complexity of the instrument and the restrictions imposed on the material properties. The major disadvantage of the SFA is that it cannot be used to scan the sample surface, so that no topography can be acquired. Moreover, AFM offers more versatility than SFA because AFM measurements can work with smaller interacting surfaces (10^4 to 10^6 times smaller), with opaque substrates, in several environments, and can be used to characterize indentations as well [9]. Due to its high lateral resolution, AFM can be also used to map inhomogeneities at submicron scales, or variations in sample properties over the scanned area.

AFM is a local probe technique, designed to measure interaction forces between a sharp tip and the surface of the investigated sample. The principle of operation in an atomic force microscope is presented in Fig. 2.1. The “heart” of an atomic force microscope is a cantilever with a sharp micro fabricated tip, whose edge radius is on the order of several nanometres. The tip is attached to a cantilever that is fixed in a solid support (chip). In order to acquire a topography image or the interaction forces between the tip and the sample, the sample must be moved with a high precision and high lateral resolution in the x and y directions. For this purpose, the sample is mounted on a piezo scanner that can move in the x, y, and z directions in a very precise and accurate way. A laser beam is focused onto the back surface of the cantilever and the cantilever reflects the laser on to a segmented photodiode. While performing the measurement, the tip interacts with the sample, causing a deflection of the

cantilever, and, accordingly, the laser spot on the photodiode moves proportional to the cantilever displacement, returning the deflection value. A feedback mechanism keeps the tip-sample distance constant by adjusting the measured quantity (deflection or oscillation amplitude, depending on the operation mode), and thus preventing the tip and the sample from being damaged. A controller is used to collect and process the data, and to drive the piezo scanner.

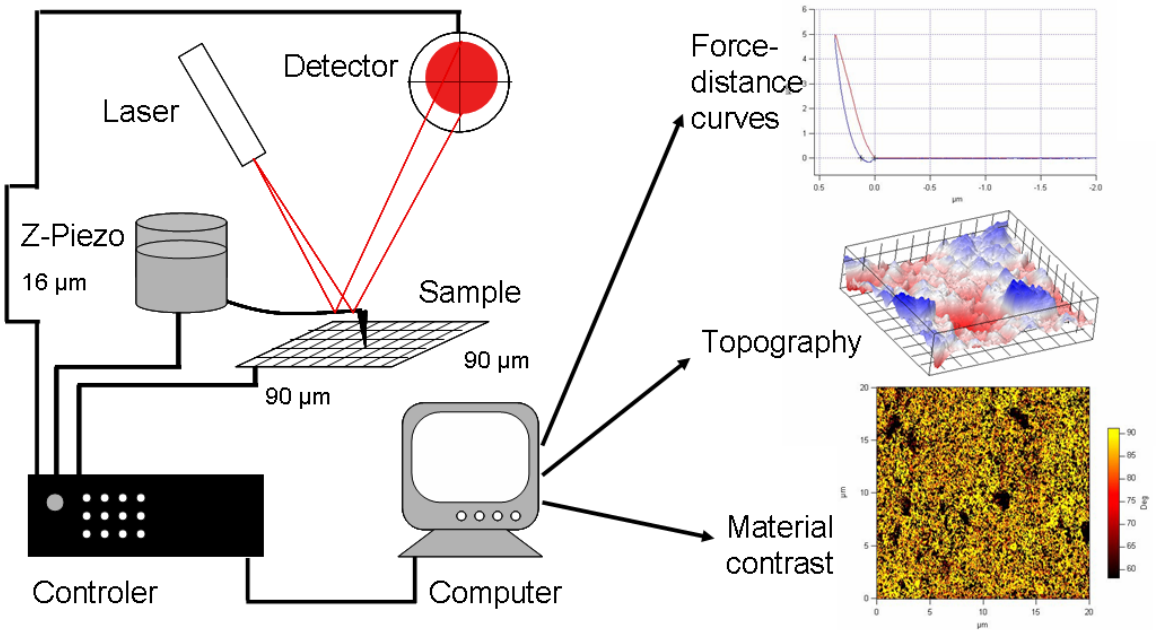

-1-

Figure 2.1 *Schematic representation of an atomic force microscope (AFM). The cantilever follows the surface of the sample with the help of the piezo scanner which is able to perform small displacements in x, y, and z directions. The cantilever deflection caused by the tip-sample interaction is detected using the laser beam reflected on the photodiode detector. A controller is used to collect and process the data and to drive the piezo scanner.*

AFM can be operated in a variety of environments such as air, different gases, vacuum or liquids. Today, commercially available AFM are equipped with environmental cells in which the temperature and the environment can be controlled.

2.1.1 Modes of operation

AFM can be operated in various modes to measure the interaction forces as a function of the tip position over the entire scanned area. These modes differ according to the force between the tip and the sample.

Contact mode

In contact mode, as the tip is raster scanned across the surface, it is deflected as it moves over the surface as shown in Figure 2.2a. In constant force mode, the tip is constantly adjusted using a feedback mechanism to maintain a constant deflection, and therefore constant height above the surface. The changes in the feedback signal required to maintain the force constant are used to reconstruct the topography. However, the ability to track the surface in this manner is limited by the feedback circuit. Sometimes the tip is allowed to scan without this adjustment; in this case the measured value is the deflection. This is useful for small, high-speed atomic resolution scans, and is known as variable-deflection mode. As the tip is in hard contact with the surface, the spring constant of the cantilever needs to be smaller than 1 nN/nm, so that materials are not damaged.

Non-contact mode

The non-contact mode belongs to the category of AC modes, which refers to the use of an oscillating cantilever. A stiff cantilever is oscillated in the attractive regime, in the very

vicinity of the sample, but not touching it, as illustrated in Fig. 2.2b. The forces between the tip and the sample are quite low, on the order of pN (10-12 N). The oscillation amplitude, phase and resonance frequency are changed by the different tip-sample interaction forces; these changes in oscillation with respect to the external reference oscillation provide information about several properties of the sample. The detection scheme is based on measuring changes to the resonance frequency or amplitude of the cantilever. Frequency can be measured with very high sensitivity and thus the frequency modulation mode allows for the use of very stiff cantilevers. Stiff cantilevers provide stability very close to the surface and, as a result, this technique was the first technique to provide atomic resolution in ultra high vacuum conditions. For specimens absorbed poorly on a substrate surface the advantage is clearly seen in this mode of operation since the tip of the cantilever does not touch the sample [14].

Intermittent contact mode

The intermittent contact mode, commonly referred to as TappingMode^{TM} is the most popular mode of operation especially for the analysis of polymer materials. A stiff cantilever is oscillated closer to the sample than in non-contact mode. Part of the oscillation extends into the repulsive regime, so the tip intermittently touches or taps the surface. Very stiff cantilevers are typically used, as tips can get “stuck” in the water layer absorbed on the sample surface. The advantage of tapping the surface consists of improved lateral resolution on soft samples. Lateral forces such as drag, common in contact mode, are virtually eliminated.

Figure 2.2: *Modes of operation: contact mode (A), non-contact mode (B), and intermittent contact (C). In contact mode the tip is scanned across the surface, the cantilever being deflected as it closely follows the surface topography. In non-contact mode a stiff cantilever is oscillated in the vicinity of the sample, while the sample is raster scanned. In picture C the tip taps the sample during each oscillation and it is restored to the original position at the end of each cycle, operation called intermittent contact [14].*

2.1.2 Determination of the spring constant of the cantilevers

AFM cantilevers are usually made out of silicon or silicon nitride. To improve their reflectivity, they are usually coated with a thin metallic layer, on the top surface, the other side than the one facing the surface. Commercially several types of cantilevers are available from the shape point of view mostly used, being the rectangular and V-shaped ones. Since in this work rectangular shaped cantilevers were used, all the discussions will refer to this kind of cantilever.

The spring constant k_c of a cantilever is

$$k_c = \frac{E_t t_c^3 w}{4L^3} \tag{2.1}$$

in which t_c is the thickness of the cantilever, E_t is Young's modulus of silicon nitride, L and w are the length and width of the cantilever. Sadder and White [12, 15] have demonstrated the inaccuracy of the approximation using finite element analysis, and a more accurate formula is given by Neumeister and Ducker [13]. All these formulas are only approximations and they show the truth in ideal conditions. In our case, each individual cantilever has its own spring

constant, even if they come from the same wafer. Hence, if a quantitative estimation of forces has to be achieved, it is necessary to measure the spring constant of each cantilever. There are several methods to do this as mentioned above, but only the one used in this work will be further presented.

The most common method used for determination of the spring constant of a cantilever is by modelling the cantilever as a simple harmonic oscillator with an angular frequency. The main advantages of the method are the quickness of the experiment, and that it is non-destructive. The method is largely described by Hutter and Bechhoefer [15], where they show that the spring constant can be measured from the power spectral density of cantilever fluctuations due to thermal noise.

Generally atomic force microscopes have a built in procedure to evaluate the spring constant of the cantilever using the thermal noise method. Figure 2.3 shows the thermal noise power spectrum of a commercial rectangular cantilever, like the ones used in this work.

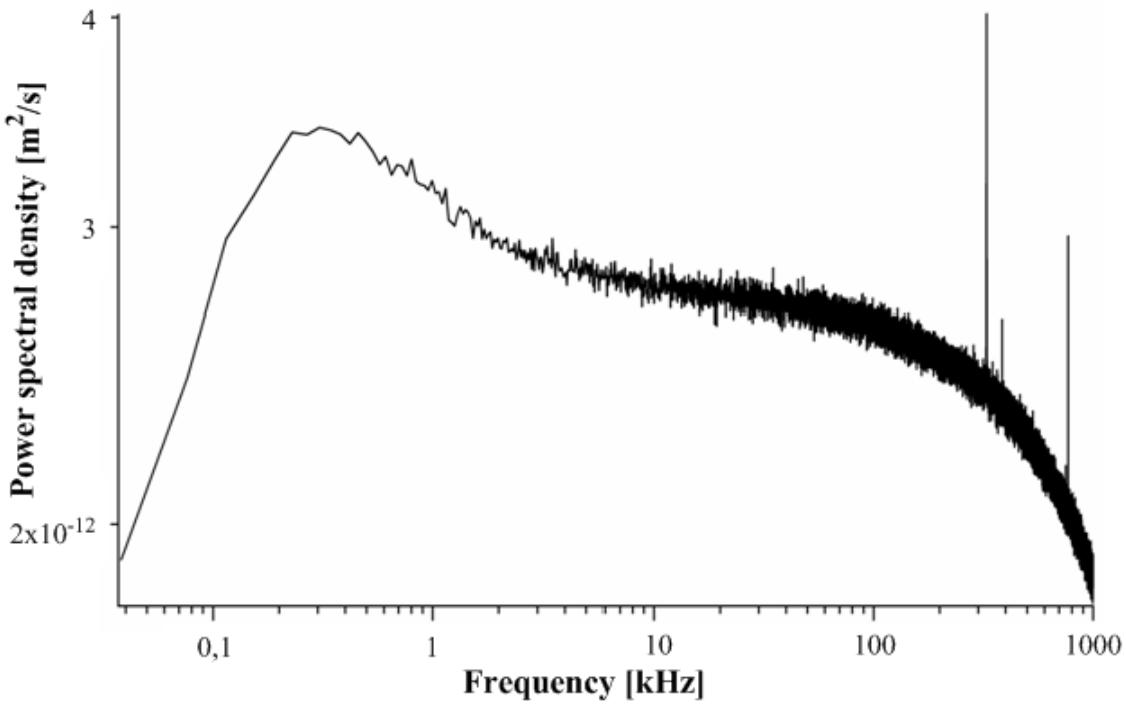

Figure 2.3: *Thermal noise power spectrum density plot measured in order to quantify the resonance frequency of a cantilever.*

A peak at around 327 kHz can be observed, but a closer look, on a smaller scale, reveals a peak like the one presented in Fig. 2.4, which corresponds to the resonance frequency of the cantilever. A simple fit using a harmonic oscillator fit will return the spring constant of the cantilever (Fig. 2.3). Further on, by having the experimental set-up calibrated and the spring constant of the cantilever known, we can proceed with the analysis of the force-distance curves.

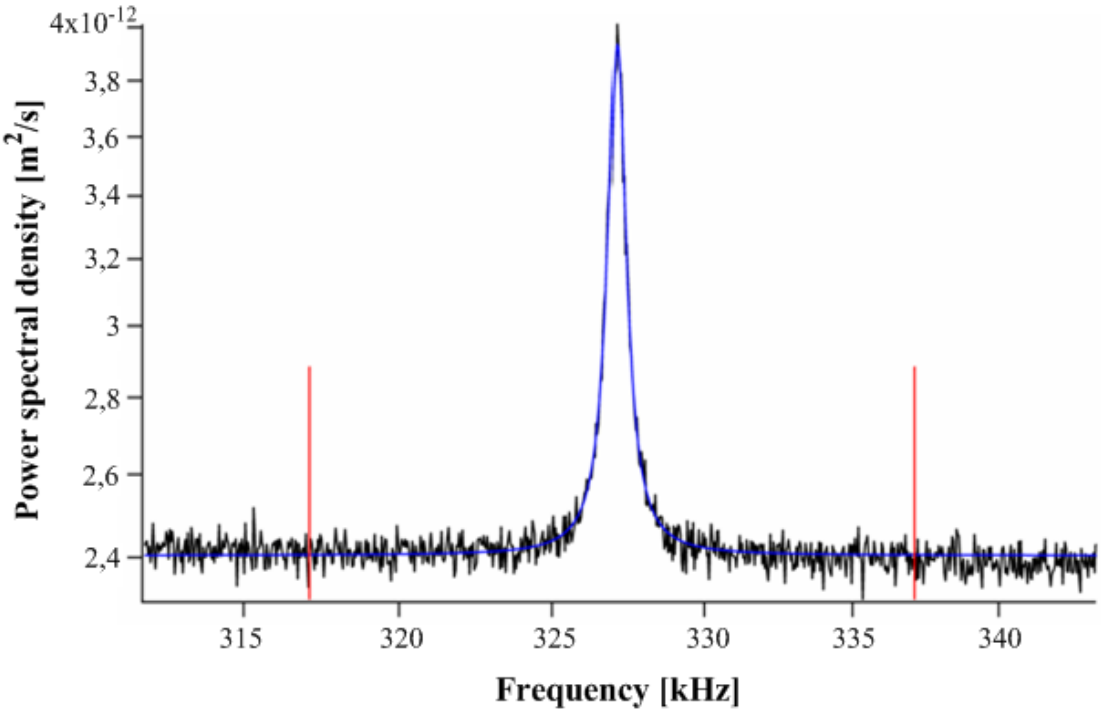

Figure 2.4: *A zoom in on the spectrum presented in Fig. 2.3.*

2.1.3 AFM force-distance curves

Another major application of the AFM, besides imaging, is to characterize the tip-sample interaction by using force-distance curves. A force distance-curve is a plot of tip-sample interaction forces vs. tip-sample distance. This plot is obtained by moving the sample towards and away from the cantilever, while measuring the static cantilever deflection Z_c by applying a voltage to the piezoelectric translator where the sample is mounted. The tip sample force F is obtained by multiplying the cantilever deflection with the cantilever spring constant k_c:

$$F = -k_c Z_c \tag{2.2}$$

The distance between the sample surface and the cantilever rest position Z_p, the tip-sample separation distance D, the cantilever deflection Z_c, and the sample deformation δ are related as follows:

$$D = Z_p + Z_c + \delta \tag{2.3}$$

Z_p is assumed to take positive values when the sample approaches the tip, Z_c is positive as the cantilever deflects upwards, D decreases as the sample approaches the tip and δ is positive when the tip indents the sample.

The distance controlled during the acquisition of force-distance curves is the distance between the sample surface and the cantilever rest position Z_p, and not the tip sample separation distance D. That is because the cantilever deflection Z_c and the sample deformation δ are not known before the measurement. Therefore, the curves obtained from the raw data using AFM should be called *deflection-displacement curves* or *force-displacement curves* rather than force-distance curves. At the beginning of the curve the piezo is at its rest position $(Z_p)_0$ and the cantilever deflection is zero as there is no interaction between the tip and the sample. When the tip and the sample are in contact, the cantilever deflects by Z_c and the piezo is displaced by Z_p (Fig. 2.4, 2.5). The tip sample distance D and the sample deformation δ are obtained from Eq. 2.3. Since the contact area and sample deformation vary as a function of load and sample properties, it is more appropriate to use deformation rather than tip-sample distance, once the tip and the sample are in contact. Also, the term force distance curves should be employed only when the force is plotted vs. the true tip-distance D. In this work, if not mentioned particularly to a specific type of plot, the term force-distance curve is used. It should be understood that an AFM force-displacement curve does not reproduce tip-sample interactions but it is the result of several contributions, such as the tip-sample interaction, elastic force of the cantilever and stiffness of the sample.

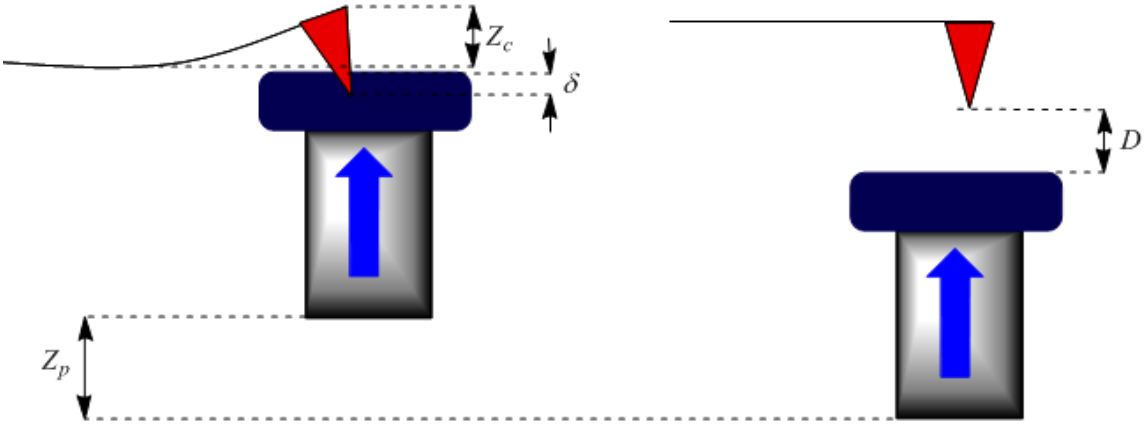

Figure 2.4: *Cantilever deflection while performing an indentation on the sample. At the beginning of an indentation the z-piezo is in the rest position* $(Z_p)_0$ *and the deflection is 0 (left). As the tip indents the sample a deformation of the sample (δ) and a deflection occurs* (Z_c).

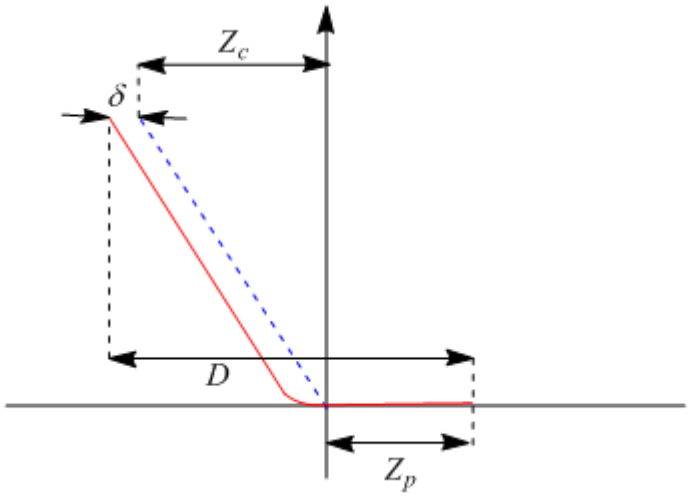

Figure 2.5: *Schematically representation of a force distance curve performed on a material which suffers a deformation δ (red line) related to an indentation on an infinite rigid material (blue). The parameters on the graph are explained in Fig. 2.4.*

2.1.4 Properties extracted from a force-distance curve

A typical force-distance curve can be generally separated into three main regions, the contact region subdivided in the approach and the withdrawal, the approach in the air, and the withdrawal in air (Fig. 2.6). The initial part of the curve, called the zero line approach, is given by the approach of the sample towards the tip. It is characterized by zero deflection, as there are no tip sample interactions. During this initial part the sample and the tip are considered to be in equilibrium.

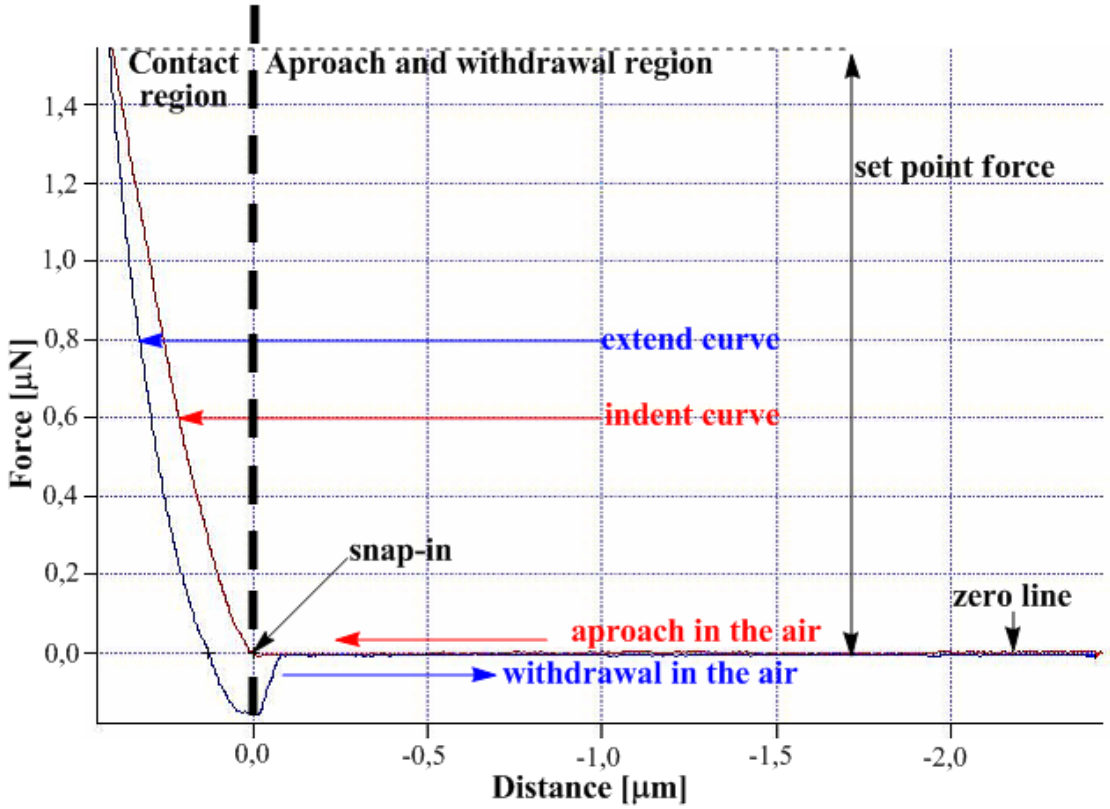

Figure 2.6: *The three main regions of a typical force-distance curve: the approach in the air, the contact region and the withdrawal in the air. As the sample approaches the tip of the cantilever there is no interaction recorded between the tip and the sample (zero line). In the vicinity of the sample attraction forces occur between the tip and the sample, and a so called snap-in occurs. The tip indents into the sample until the set-point is reached.*

As the sample approaches the tip of the cantilever the so called contact region is reached. The contact regime is preceded by a jump-to-contact phenomenon also called snap-in. This occurs at the moment when the attractive forces between the tip and the sample exceed the elastic constant of the cantilever, the moment when the equilibrium is lost and the tip "jumps" onto the surface. The maximum value of the cantilever deflection at the snap-in of the attractive forces can be estimated.

After the snap-in the tip and the sample will remain in contact, the tip will indent into the sample until a certain force value (set-point) will be reached. This value can be manually set by the user and is called maximum force, or set-point force. During this approach the cantilever will suffer the highest deflection from a force distance cycle. The first derivative of the approach line gives information about the stiffness of the sample.

When the set point for maximum force is reached (Fig. 2.6) the sample is retracted. During the withdrawal, the tip and the sample will remain in contact until the withdrawal force is higher than the adhesion force between the tip and the sample. The withdrawal curve will generally not overlap with the approach curve, unless there is no plastic deformation of the sample. The comparison of the approach and the withdrawal curves will provide information about the elastic-plastic properties of the sample.

The adhesion force is a combination of electrostatic forces, Van der Waals forces and capillary forces. It can be calculated as the area under the base line of a force-distance curve (Fig. 2.7). Force-distance curves have become a very important method to characterize adhesive properties of different materials [6].

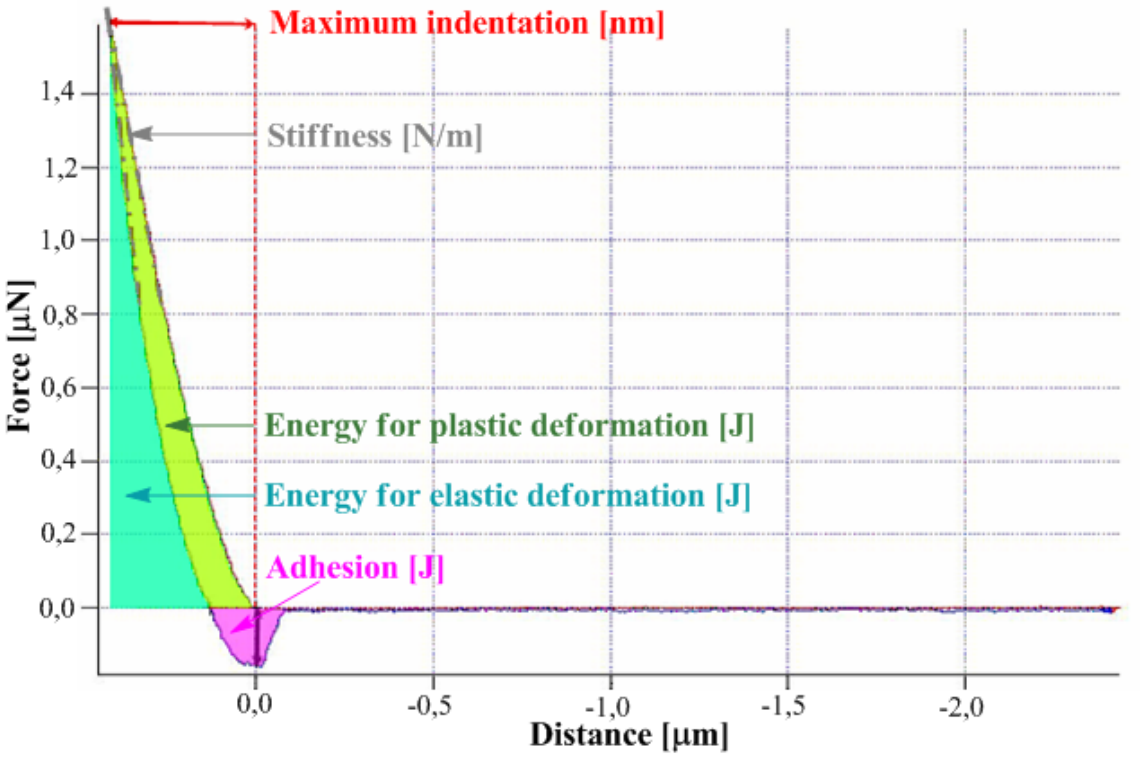

Figure 2.7: *The main properties which can be extracted from a typical force-distance curve.*

Perhaps one of the most important parameter which can be extracted from a force curve is the maximum indentation (MI) since it is used in the calculation of the elastic modulus (Fig. 2.7). The maximum indentation is calculated from the maximum deflection reached at the maximum set-point force. However, the maximum indentation can be divided into two components, indentation of the tip into the sample, and the deformation of the sample. The value for maximum indentation can be directly computed from the force-distance curve. The real indentation and the deformation require a special procedure which will be largely described in a following chapter.

2.1.5 Force Mappings

It is of a great importance to characterize different regions of the investigated sample, in order to compare heterogeneities at submicron scale and to observe changes in the properties as a function of the investigated location. To be able to image micromechanical properties at nano- and microscales, a collection of force-distance curves should be employed (the so- called force-mapping). The F-D curves are taken at prespecified distances from each other, forming a grid of equally spaced force curves across a surface (in our case a square with a predetermined length).

The microscope has a standard procedure to produce such a force-mapping. It allows the user to input the number of points in both x and y directions on the preselected image, where the curves should be performed. A force set-point can be chosen, allowing thus the cantilever to indent the sample until that set point is reached. Setting this set-point constant to each indentation, can provide valuable information regarding the micromechanical properties of the sample in each spot.

A schematic representation of a 10x10 force mapping matrix can be seen in Fig. 2.8. The curves acquisition order is shown by the arrows. In the mapping procedure, all the force-distance curves start at fixed height, followed by an approach-withdrawal cycle, and a lateral displacement to the next position. These steps are continued until the number of x curves is obtained (x = 100 in the present case).

The first point of the mapping is always the bottom left point as shown in Fig. 2.8. The force-mapping acquisition can be very time consuming and depends largely on the scan rate, and the number of points chosen. It may last from several minutes, up to several hours per one

mapping. The fast scans are employed in the case of a fast comparison between 2 samples, such as hardness or modulus, while the slow scans are employed in case of heterogeneity differentiations between two samples. The acquired data can be arranged as 2D or 3D maps of properties like stiffness, maximum indentation, adhesion or local modulus, showing the spacial variation of these properties.

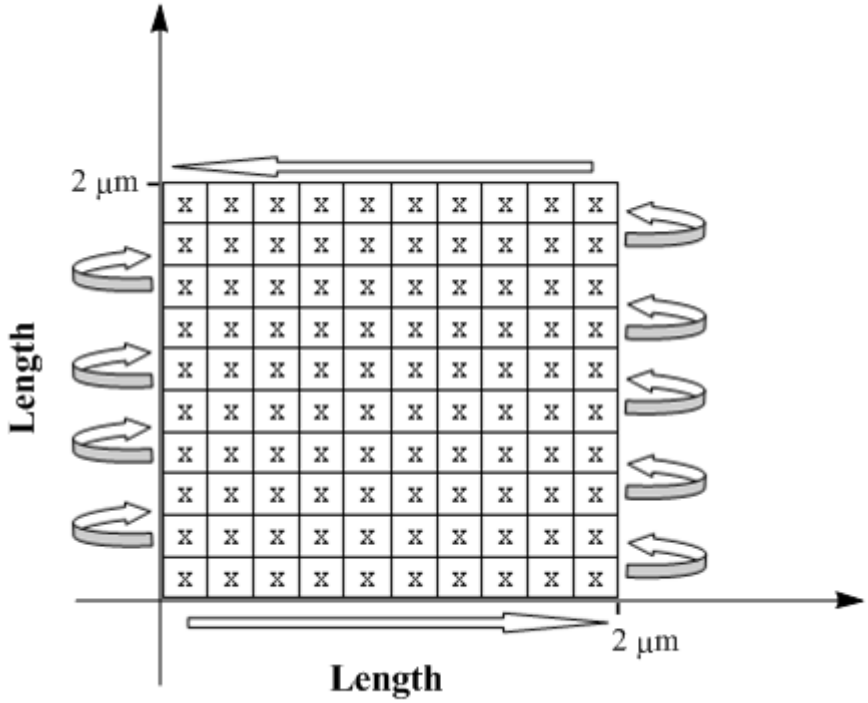

Figure 2.8: *Schematically representation of a force mapping experiment. During a force mapping the cantilever follows the path represented by the arrows in the figure.*

Figure 2.9 show a force mapping experiment on a 48 phr filled EPDM elastomer. In each direction, x and y, 60 force-distance curves were acquired with a distance of 33 nm between the indentation points. The data in the graph show the values for the maximum indentation while using a constant force as set-point.

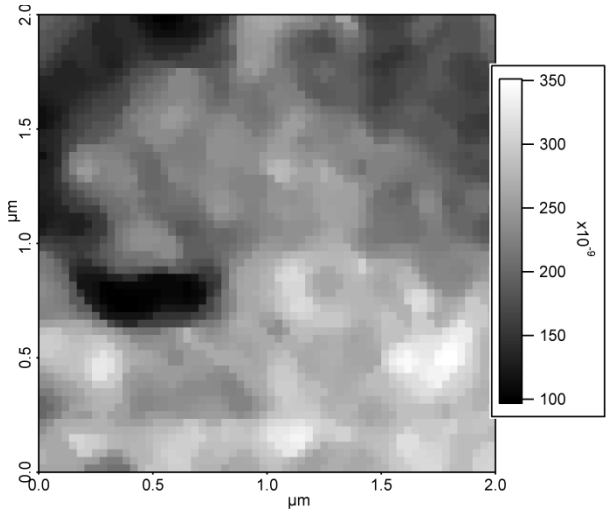

Figure 2.9: *Force mapping experiment consisting of 60x60 force-curves. The first acquired point in a force mapping experiment is the bottom left point. The mapping reveals differences between hard (dark structures) and soft areas (bright structures) at micrometer scales in filled EPDM elastomer*

2.2 Materials

2.2.1 Elastomers

The main characteristic of elastomers is their elastic behaviour after deformation, when an elongation or compression is applied. These materials are able to suffer stretches up to ten times their original lengths and still return to their original shapes and lengths after the tension removal. The performances of an elastomer can be further enhanced by reinforcement with materials such as fillers, fibres, metals and other additives like vulcanization accelerators and anti-aging substances. Depending on the properties of the reinforcing material, the tensile strength can be considerably increased, at the cost of the extendibility. Combining the elasticity of elastomers with the stiffness of the filler materials, the usage of the rubber composites will increase considerably.

An elastomeric network is given by several macromolecular polymeric chains interconnected by chemical and physical cross-links. The chemical cross-links are of great importance because their density depends on the concentration of the vulcanizing agent in the elastomer. In addition to the polymer chains, commercial elastomers contain other components or additives such as carbon black, precipitate silica, clays and calcium carbonate for cost reduction purposes, and reinforcement roles. A rubber material can be easily stretched for several times up to 200% without breaking and it recovers the initial state almost 100% instantly. Rubbers can be classified into two main categories according to their provenience source as natural rubber and synthetic rubber [16].

Natural rubber

Natural rubber (NR) (Fig.2.10) is produced by a special tree, as a milky colloid (latex). The tree Hevea brasiliensis is considered the most important source, being able to produce more latex than trees like Palaquium gutta or Castilla elastica. NR has a very high molecular weight (MW) with long branches.

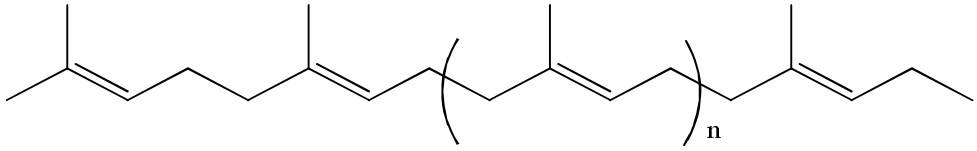

Figure 2.10: *The structural formula of cis-polyisoprene (natural rubber).*

Synthetic rubber

Any type of rubber material that contains polymers obtained through chemical synthesis can be considered as synthetic rubber. Nowadays, the request for improved material properties in the rubber industry is very high; therefore, very often the synthetic rubber is used as a substitute for natural rubber. Synthetic rubber can be obtained from polymerization of different types of monomers, leading to a variety of different types of rubbery materials. A wide range of polymeric materials can be obtained, with different properties like heat aging resistance, chemical resistance, temperature resistance or mechanical properties [17]. This thesis is focused on the ethylene-propylene-diene monomer (EPDM) rubber, belonging to the ethylene-propylene (EPM) class of copolymers.

Ethylene-propylene copolymers (EPM) and ethylene-propylene-diene monomer (EPDM)

EPM is a saturated synthetic elastomer, obtained via insertion polymerization of ethylene, propene and a diene monomer [18]. Due to insertion of diene in the EPM chain, the sulphur vulcanization and enhanced peroxide curing are possible. The most common diene monomers that are used in polymerization process of EP(D)M are: Dicyclopentadiene (DCP), Ethylidene Norbornene (ENB) and Trans-1,4 Hexadiene (HX). The structural forms of the diene monomer and EPDM are presented in Fig. 2.11 [19, 20]. Depending on the ethylene content of the composition, the copolymer has different properties. Higher ethylene content leads to higher loading possibilities, and thus the rubber can be better processed (e.g. by mixing and extrusion) [18].

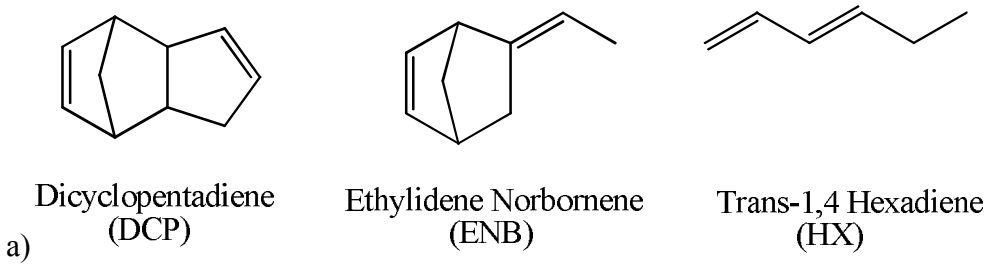

a)

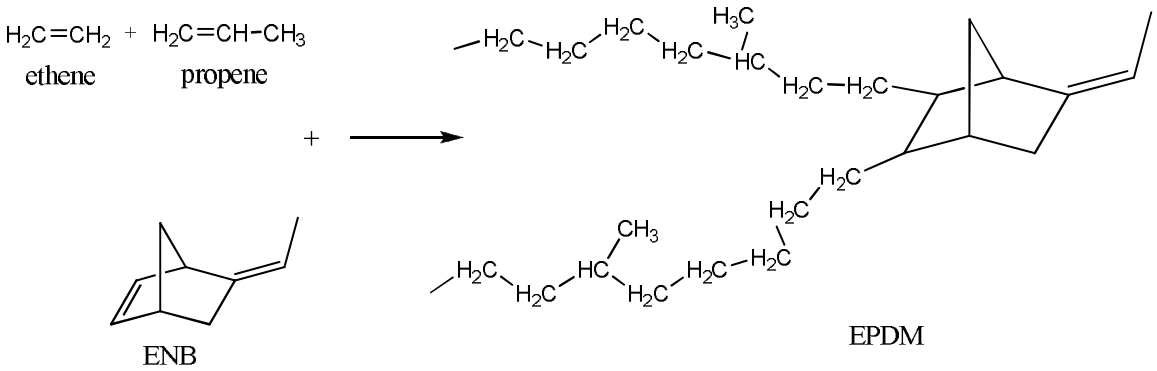

b)

Figure 2.11: *Structural form of common diene (a) and EPDM (b) [18].*

Due to its saturated polymer backbone, EPDM shows higher resistance to chemical attack by oxygen, UV, ozone and heat than natural rubber (NR), polybutadiene rubber (BR) and styrene-butadiene rubber (SBR). Therefore, EPDM is very often used for outdoor applications like automotive sealing systems, window seals and roofing membranes. The compatibility with fireproof fluids, ketones, alkalines, hot and cold water is satisfying, but in case of unpolar fluids, like most oils (aromatic and aliphatic hydrocarbons, gasoline, kerosene, etc.), the resistance is quite low [20].

Vulcanization and crosslinking of EPDM

Vulcanization is the irreversible chemical process applied to rubber compounds to convert them in more durable materials, with the help of curing compounds like sulphur or peroxide [21]. After the vulcanization process, the compound is transformed from a linear polymer into a three-dimensional macromolecule, with cross-links formed between the polymer chains [20].

Cross-links are covalent or ionic bonds that link one polymer chain to another, reducing thus the ability of the polymer chain to move individually; this modifies the physical properties of the material (Fig. 2.12). Cross-links can be formed by chemical reactions in a curing process or can be induced by exposure to a radiation source, such as electron beam, gamma-radiation, or UV light [22].

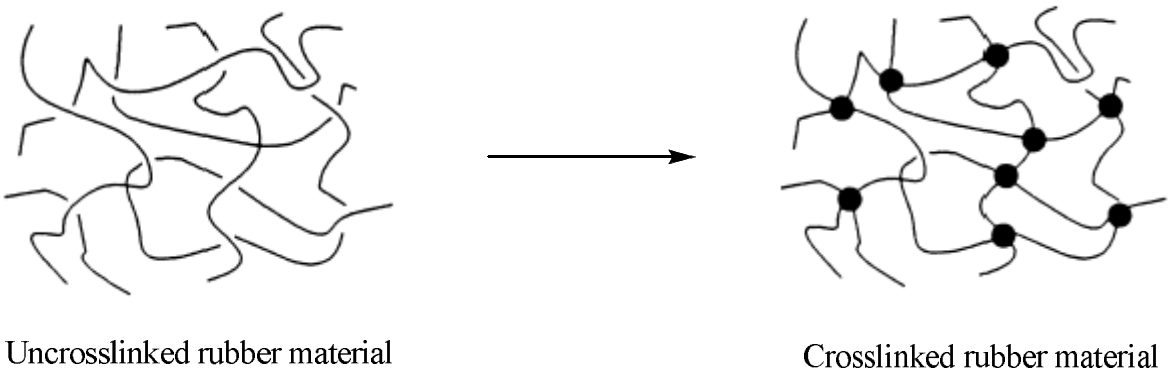

Figure 2.12: *Schematic representation of vulcanization, showing the difference between uncrosslinked and crosslinked rubber materials.*

Because EPDM shows a small amount of unsaturation, the curing with sulfur is relatively slow and a large amount of different types of accelerators is needed. However, curing with peroxide carbon-carbon crosslinks with high thermal stability could be achieved [23, 24]. The chemical process of EPDM rubber curing with peroxide is schematically represented in Fig. 2.13. After the curing process, the cross-links structures and the modification in the polymer chains show a significant increase of the mechanical properties of the vulcanizates [21].

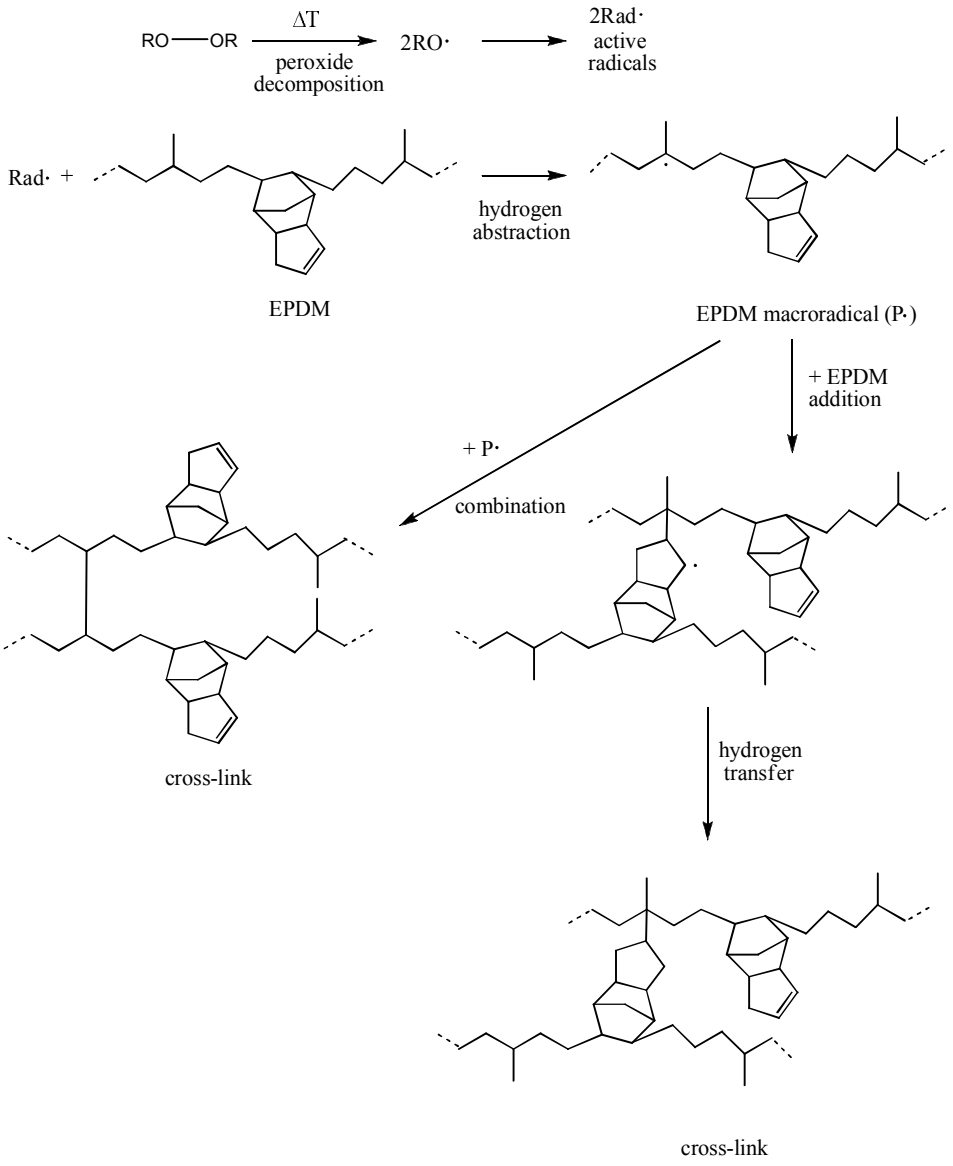

Figure 2.13: *Simplified scheme of peroxide curing of EPDM [25].*

2.2.2 Fillers

The filler reinforcement effect on the vulcanized rubber compounds is to increase the mechanical properties of the resulting material (e.g. tensile strength, resistance to tearing and stiffness). In the rubber industry the most popular reinforcing fillers are carbon black, silica, clay and calcium carbonate also known as chalk [17, 21].

Carbon black

Carbon black is widely used as filler to modify the mechanical, electrical and optical properties of the medium in which it is dispersed. These applications play a major role in elastomers, plastics and in paints and inks.

Carbon blacks are mainly obtained by the chemical decomposition of natural gas or oil. Two classes predominate: the furnace blacks (95% of black usage), with a high surface activity and thermal blacks (5% of usage), with low activity. There are a substantial number of blacks designed for special applications such as electrically conducting and printing ink blacks. The latter consist in particles that are too fine for rubber use [26]. The properties of carbon blacks such as iodine adsorption number or DBP (Dibutyl phthalate) adsorption number are illustrated in Table 2.1.

Table 2.1: *Nomenclature and properties of carbon blacks [20].*

Carbon black properties					
ASTM classification	D6556 N_2SA adsorption m^2/g	D2412-00 DBP adsorption 10^{-5} m^3/kg	D3493-00 DBP no. compressed 10^{-5} m^3/kg	D1510-99 Iodine adsorption g/kg	D3265-00 Tint strength
N110	130	113	98	145	124
N115	143	113	96	160	123
N120	126	114	98	122	131
N121	124	132	109	121	121
N134	145	127	102	142	132
N220	115	114	100	121	115
N234	120	125	103	120	124
N330	79	102	88	82	103
N335	85	110	94	92	110
N339	92	120	101	90	110
N343	96	130	104	92	114
N351	71	120	97	68	100
N550	41	121	86	43	-

Carbon blacks contain 90-99% elemental carbon in combination with hydrogen and oxygen. Typical functional groups located on the blacks surface are phenol, carboxyl, lactol, quinone, ketone, pyrone and lactone (Fig. 2.14).

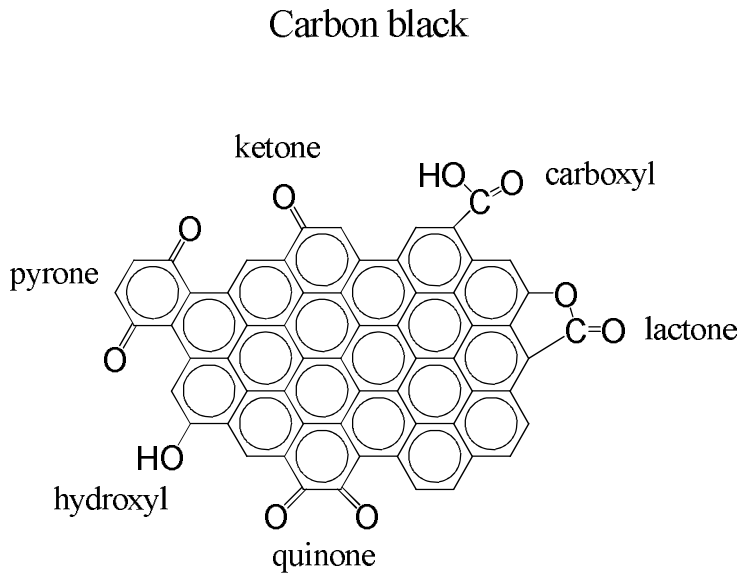

Figure 2.14: *Schematic representation of a carbon black layer interacting with functional groups [26].*

There may also exist traces of chemically combined sulphur, associated with the source of some feedstocks. The surface of the black particle is not smooth, and internal porosity of the particle may be caused by oxidation during the high temperature manufacturing process. In terms of rubber reinforcement, the black surface activity may be defined as the capacity of restricting the mobility of the rubber in contact with its surface. The strongly adsorbed polymer chains on the surface of the carbon black reduces the chains mobility and becomes bound rubber [27, 28] (Chapter 2.3 will explain the polymer filler interaction and bound rubber). Bound rubber strongly depends on the specific surface area of the carbon black and shows significant dependence on the degree of structure development, increasing with both variables [28].

The surface area of blacks ranges from 20 m^2/cm^3 (N990 - Medium thermal black) to 225 m^2/cm^3 (N110 - Super abrasion furnace black) [26]. The primary particle of carbon black produced is basically a spheroid consisting of concentric layers of carbon atoms. These

particles aggregate together during fabrication, forming grapelike and tangled three dimensional structures [25]. These primary aggregates can further associate to form 'secondary' structures (Fig. 2.15) [29]. Atomic force microscopy can easily highlight the size distribution of the carbon black fillers in a mixture (Fig 2.16).

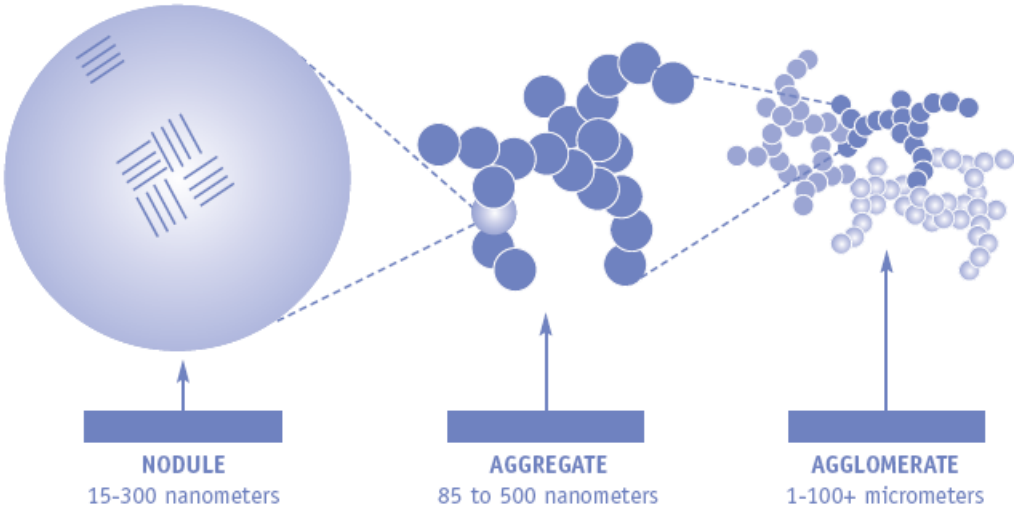

Figure 2.15: *Spatial arrangement of carbon black particles [29].*

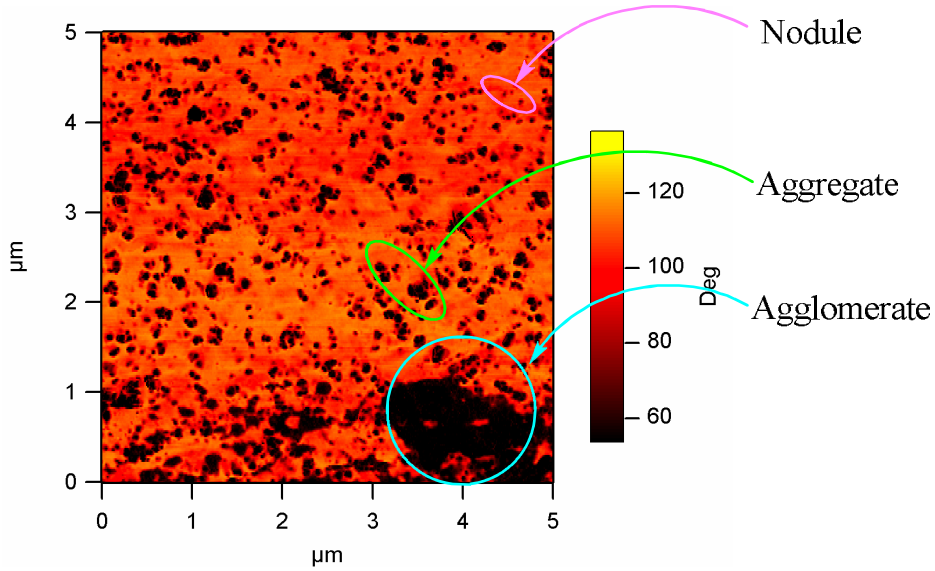

Figure 2.16: *AFM phase contrast image of a 48 phr carbon black filled elastomer showing the dispersion of the carbon black, and the size distribution of the fillers (primary particles, aggregates, agglomerates.)*

This structure is weak in nature and can be partially destroyed during pelletisation. The remainder of the black's 'structure' brakes down during the procedure of black mixing into rubber [29]. The structure of a carbon black depends on the processing conditions and the nature of the oil/gas feedstock. The bigger the structure of the carbon black the more irregular is the shape of the aggregate. The aggregates cling together to form agglomerates (Fig. 2.16). In this form, carbon black is a fluffy, difficult-to-handle product, unsuitable for automatic weighting. Pelletisation produces a roughly spherical, easily broken pellet, which will contain a large number of aggregates [29].

The size of the carbon black particle has a strong influence on its dispersion characteristics within the rubber matrix and determines the final vulcanizate properties of the rubber compound. Blacks of very fine particle size are difficult to disperse adequately and when dispersion is achieved they give a high reinforcement. Large particle size blacks are easy to disperse completely, but do not offer sufficient reinforcement [29, 30].

Atomic force microscopy, together with scanning electron microscopy (SEM) and transmission electron microscopy (TEM) are proper tools to visualize the size and the dispersion of the carbon black agglomerates in a polymer mixture. In this study, a set of mixtures consisting of different filled EPDM elastomers was prepared to show the behaviour of different carbon blacks in AFM analysis. Carbon blacks N115, N339 and N550 were mixed with an amorphous EPDM. Four different concentrations of fillers (10, 30, 48, and 60 phr carbon black) were used for each type of carbon black. The phase contrast images acquired using the AFM technique for all the samples are presented in Fig. 2.17. From left to right an increase of the dark structures number can be observed, representing the carbon black agglomerates (Fig. 2.17). The size of the filler structures shows also an increasing tendency from up to bottom.

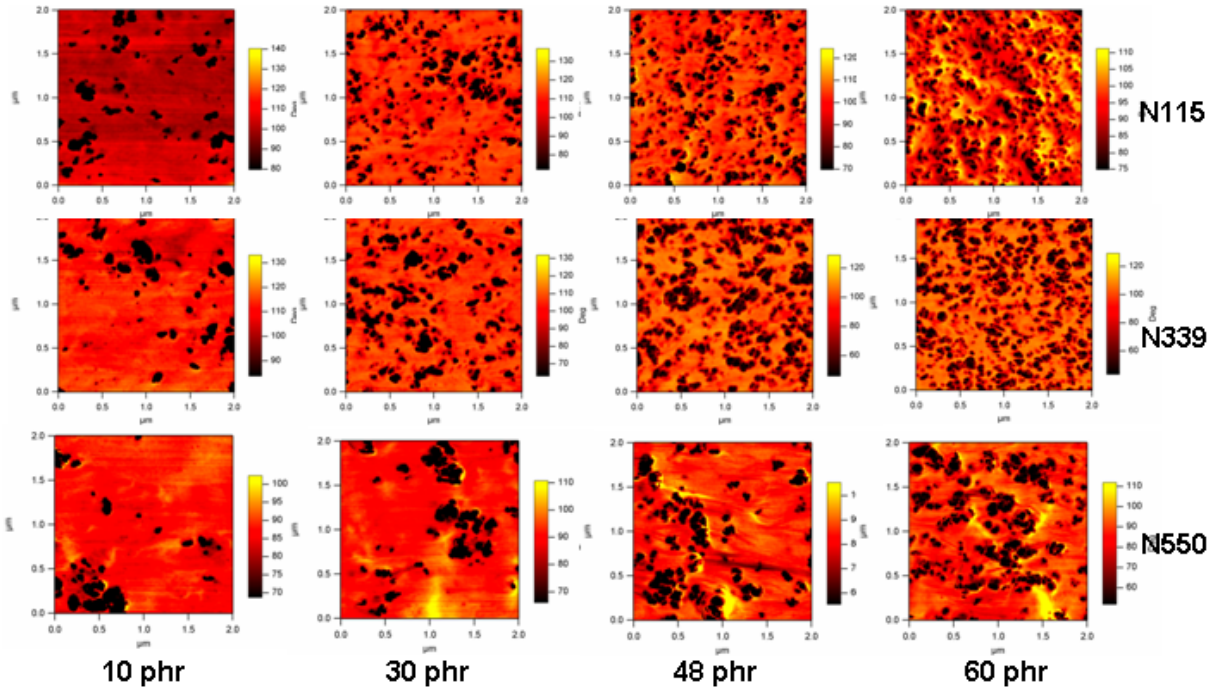

Figure 2.17: *AFM intermittent mode phase images of different filled EPDM elastomers. From up to down an increase of the size of the particles is to be observed, caused by the different carbon black type. From left to right the filler concentration is increased revealing the formation of filler agglomerates and aggregates.*

2.3 Polymer-filler interactions

By mixing an elastomer and a reinforcing filler, strong interactions occur in such a manner that a good polymer solvent can extract only a free rubber portion, leaving a highly swollen rubber-filler gel. The bound rubber is, by definition, the rubber content of this gel [3]. This effect is known for more than 80 years in the case of carbon black filled and is considered one of the major factors in reinforcement and often a global measure of surface activity of the filler. For a given elastomer, the amount of bound rubber for a fixed filler content depends on several factors, namely the surface area, structure and surface activity of the filler, the state of mixing and the storage maturation of the compound. The chemical structure and the macromolecular characteristics (molecular weight, polydispersity, branching, etc.) of the rubber are also important parameters affecting the bound rubber content. It is obvious that the bound rubber is an "all inclusive" macroscopic property surely reflecting many diverse (nanoscopic) effects, some of which became clear only recently, due to developments in advanced analytical instrumentation and techniques (e.g. atomic force microscopy or nuclear magnetic resonance) [3].

Bound Rubber represents the rubber fraction that after an extraction in optimal conditions remains unsolved, because this polymer is really tight bonded and adsorbed on the surface of the carbon black. This rubber fraction is dependent on several parameters and can be controlled and modified through different physical and chemical effects, and mixing parameters. As it was recently discovered, the bound rubber fraction can be increased by increasing the mixing energy (k) [31, 32]. Figure 2.18 illustrates the bound rubber formation during the mixing process.

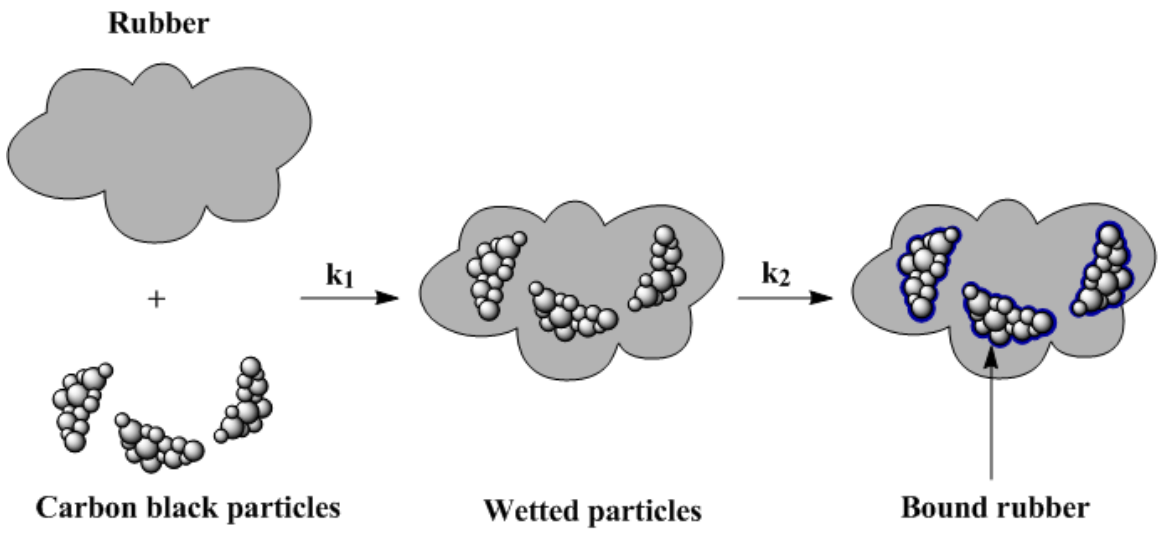

Figure 2.18: *Formation of bound rubber during the mixing process.*

Bound rubber is strongly influenced by the morphological properties of carbon blacks. The higher the surface of primary particle the higher the bound rubber content is [3]. Considering that there is no standard procedure to determine the bound rubber content, special attention must be paid when quantifying these values.

Hints of polymer chains adsorbed onto the filler surface can be extracted from AFM imaging. An overlay of a phase contrast image over the topography acquired on a 48 phr carbon black filled EPDM elastomer reveals three regions of interest (Figure 2.19). The dark structures are clearly attributed to the filler agglomerates, while the yellow regions represent the polymer matrix. However a third region of interest is to be observed, represented by the red coloured region surrounding the filler particles. It is not a clear evidence of the bound rubber, but considering the principle of phase imaging acquisition it is a region with a lower energy dissipation compared to yellow region. This is a hint of a stiffer material, in our case a thin layer of adsorbed polymer chains on the filler particle.

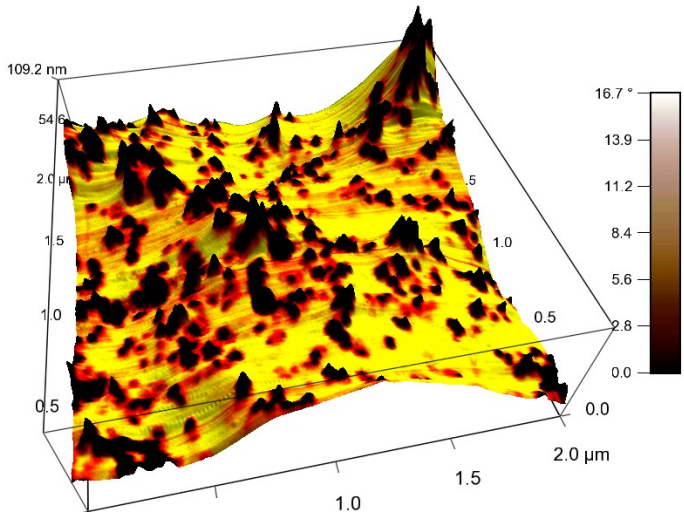

Figure 2.19: *Three dimensional representation of a filled EPDM elastomer obtained by overlaying the phase contrast on the topography of the sample.*

2.4 Filler-filler interactions

Starting with a certain filler concentration in the rubber composite, also known as a percolation point, a change in the reinforcing mechanism can be observed. By increasing the concentration of the reinforcing fillers in the polymer matrix, a three dimensional filler-network is created. An increase in the concentration will drastically reduce the distances between the filler particles, allowing them to connect each other via Van-der-Waals forces. Above this percolation point when the filler-filler network is created, a relationship between the modulus and the filler concentration can be drawn:

$$G' \sim \theta^{3.5}$$

where G' is storage modulus and θ is the filler concentration The exponent 3.5 can be experimentally determined and represents a result of the fractal structure of the filler clusters.

Above the percolation point the modulus of a filled elastomer shows an amplitude dependency. This dependency is also known as “Payne-effect” [2]. With increasing of the deformation, the modulus decreases from a maximum to a minimum. The difference between the two moduli is represented by the reinforcement caused by the filler-filler interactions. The reduction of the modulus is caused by the destruction of the three dimensional filler network built up in the polymer matrix.

At small amplitudes in dynamic experiments the modulus is governed by the filler-filler interactions. At constant small deformations the modulus is dependent on several parameters such as filler dispersion, structure, and temperature. Figure 2.20 shows an RPA amplitude sweep on a filled EPDM elastomer with two different concentrations (30 phr and 60 phr). A decrease of the modulus is observed with increasing amplitude. Two consecutive amplitude

sweep tests were done. At 30 phr the decrease of the modulus between the two sweeps is low, suggesting that the filler network is under the percolation point. In case of a 60 phr filler concentration, a strong decrease of the modulus is observed (from 870 kPa to 650 kPa). At such loads, the existing three dimensional network is destroyed at high amplitudes, causing thus the decrease of the modulus.

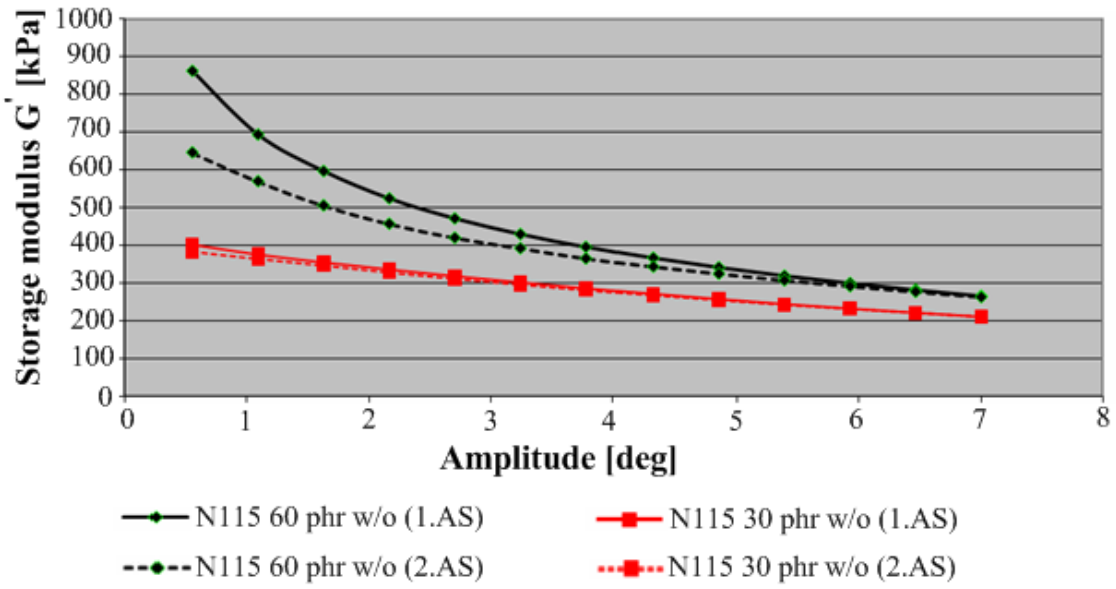

Figure 2.20: *RPA amplitude sweep acquired on different filled EPDM elastomers in an uncured state.*

3. Sample preparation

The sample preparation is one of the key processes in any experimental research work and is often underappreciated in terms of its significance. It is of a crucial importance to make sure that any interpretations of the results are not artefacts caused by the variation of the sample preparation. Unless there is 100% certainty that the prepared samples follow the identical steps during preparation, no meaningful interpretations can be done. Therefore a consistent and careful sample preparation is required since physical and mechanical properties of polymers in our case, may lead to significant variation depending on the preparation procedure.

This careful approach is important during sample preparations preceding AFM or DMA measurements because these methods require small rubber pieces which need to be cut in order to fit the experimental setup. In case of NMR low field measurements which are non-destructive towards the samples, no special preparation is required. However special care must be taken when evaluating NMR results, since effects such as vulcanizing skin may have a big impact on the results.

Boey [33] mentions in his report several aspects where great care should be taken. He focuses on the preparation of the sample from the industrial point of view. Most of the methods described are not subject of this thesis except the cutting of the samples. Since AFM requires very flat structures to be investigated the cutting procedure plays a significant role. Using different cutting methods such as razor, rotary cutter, shear cutter results such as elongation at break and tensile strength may differ for same sample [33].

3.1 Influence of the sample preparation

Further discussion will be focused on the sample preparation for the AFM measurements. AFM is a great tool for surface investigations but due to its build-up it has several limitations regarding the investigated surface. It must as flat as possible to avoid crashing of the cantilever onto the high structures. Another important step during preparation is that the investigated surface must be parallel to the substrate. In case of a tilted surface with a certain degree related to its substrate, a sample can give a different image compared to a parallel one. This can be explained taking into consideration the shape of the cantilever, and the interactions between the tip and the sample. Kashani [34] has performed an extensive study reporting the effects of the sample tilting on the final results. They claim that after experimental methods, and FEM simulations, a tilt of only 5 degrees will result an 8% deviation in the hardness results, and a 4% deviation in the calculated modulus. They have also developed a correlation equation using FEM simulations to correct the obtained values as a function of tilting. A schematically representation is shown in Fig. 3.1.

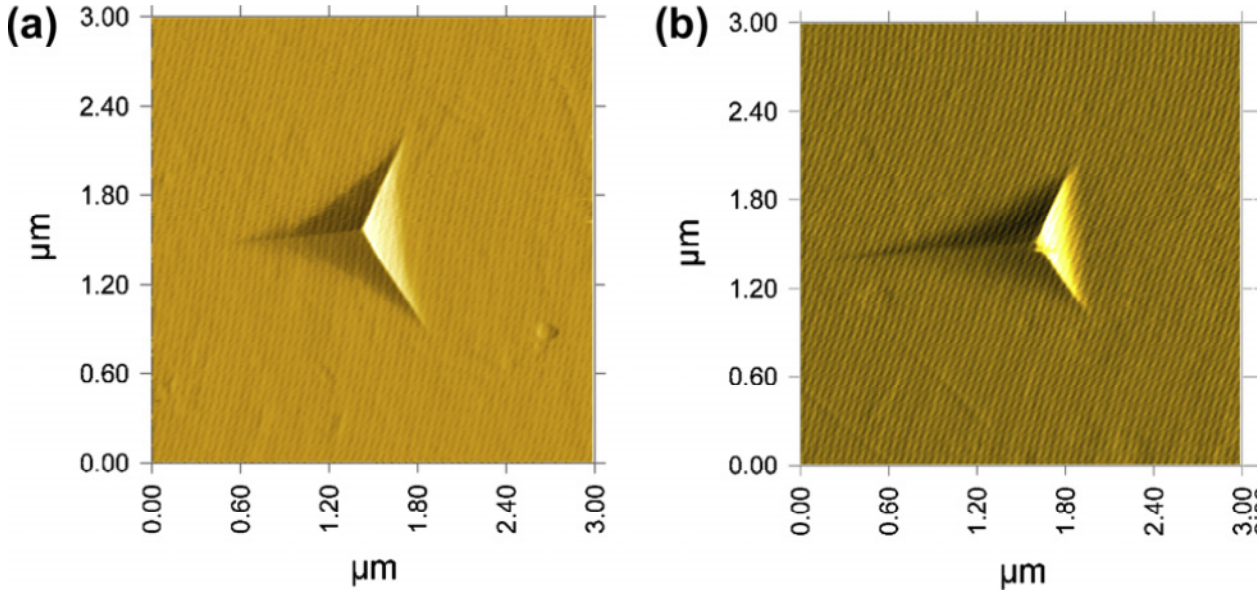

Figure 3.1: *The scanned impression of indentations on fused quartz with nominal contact depth of 150 nm for (a) the untilted sample and (b) the 5degrees tilted sample. (image reproduced from [34])*

A variation of the sample preparation is shown in the following example. A vulcanized EPDM elastomer filled with 48 phr carbon black N115 was used for the comparison. Two different way of preparation were performed. A normal razor blade cut and a crio-microtomed using a steel blade. The results are shown in Fig. 3.2.

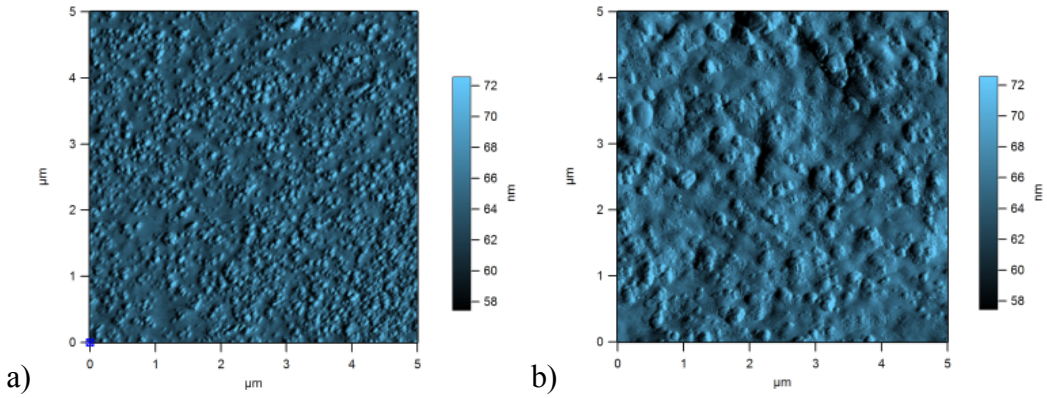

Figure 3.2: *Amplitude image of a filled EPDM with 48 phr. a) Surface prepared using a crio-microtome and a steel knife b) surface prepared using a razor blade cut.*

In case of the microtomed cut (Fig 3.2a.) the resulted surface is a very flat one, with small observable structures. Not the same thing can be said about the razor blade cut, where the structures are visible higher (Fig. 3.2b). In this case the quality and the shape of the steel blade is an important factor.

A closer look at the images presented above, and having in mind that the sample used was the same, it is clear that sample preparation has a key role in data interpretation. Analyzing the cross-sections of the up-mentioned images, if one does not care about the sample preparation, and is interested in particle analysis could come to false results (Fig. 3.3)

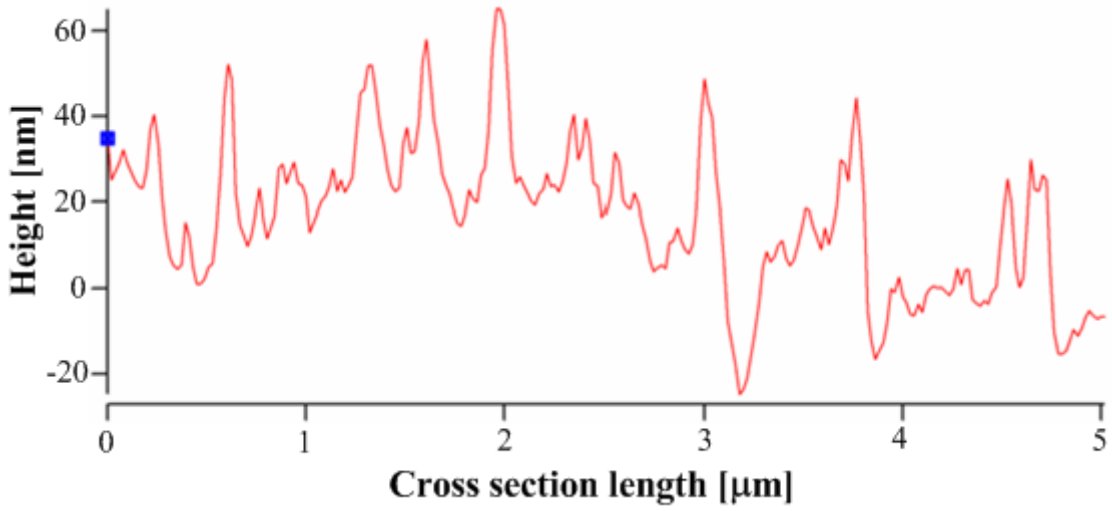

a)

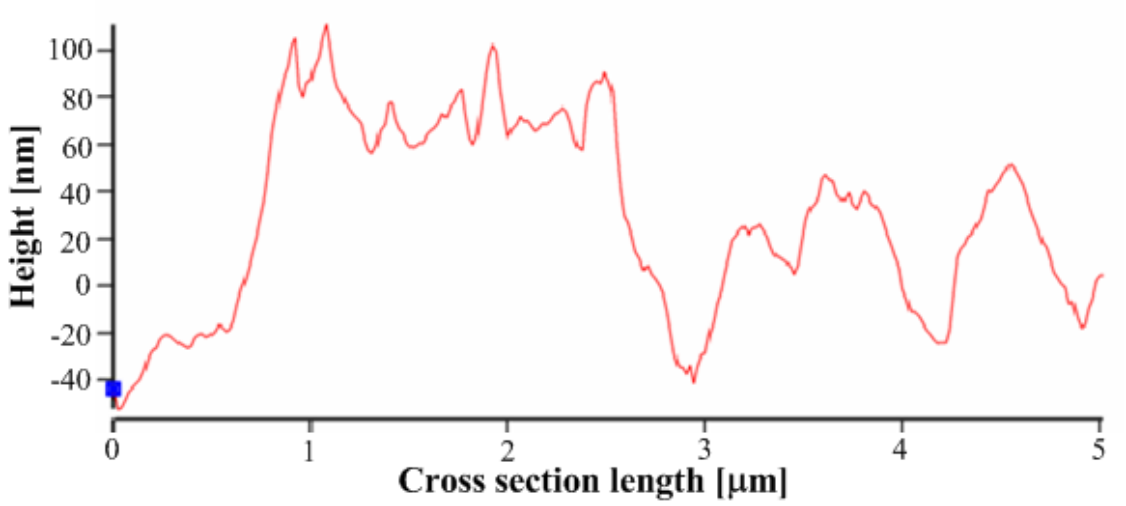

b)

Figure 3.3: *Cross sections of AFM measured surface of a filled EPDM elastomer with 48 phr, using two different preparation methods. A) crio-microtomed cut. B) razor blade cut.*

In case of the microtomed cuts very small structures can be observed, with heights ranging between 30-50 nm and diameters starting from several 100 nanometres (Fig. 3.3a). The same sample, but this time razor blade cut returns about 2 times higher structures, and diameters around one micrometer (Fig. 3.3b). A better insight of the situations described above can be one by taking a look the three dimensional representations of the height images (Fig. 3.4 a) and b)).

a)

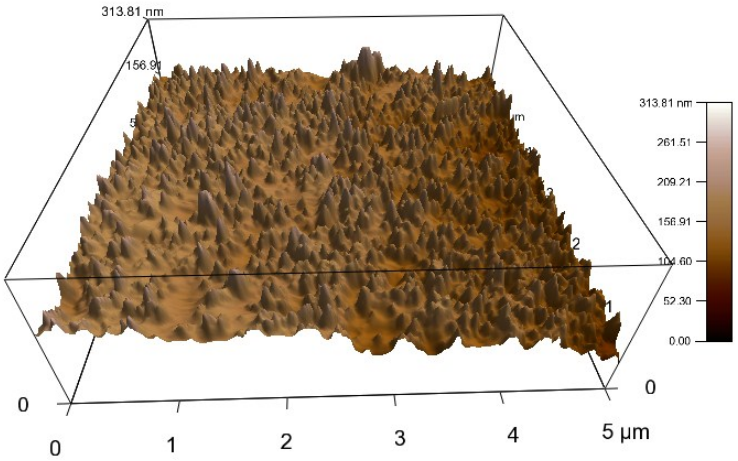

b)

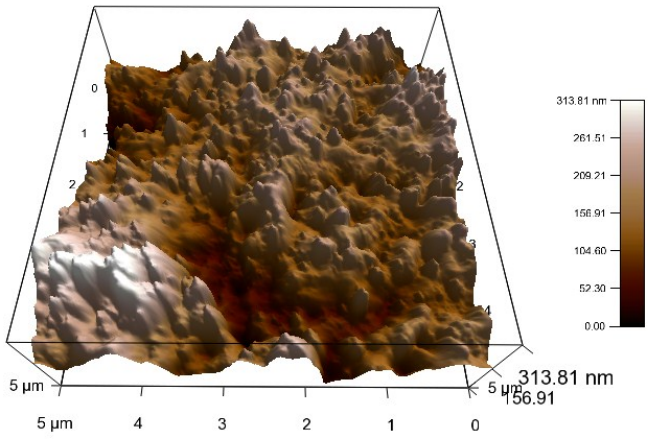

Figure 3.4: *3D representations of the investigated surface using 2 different sample preparation procedures. a) microtome cut b) razor blade cut.*

For the investigations used in this thesis where it is not particularly mentioned, the following sample preparation methods were used. Rubber sheets of 2 and 6 millimetres thickness were prepared using a heat press. For NMR investigations the samples required no further preparation. Care was taken at data interpretation of the properties of the material at the contact edges with the heat press, where it is well known that the so called "vulcanization skin" occurs. In case of AFM measurements small pieces were cut from the frames obtained from the heat pressing. The surface for investigation was further processed using a crio-microtome. The samples were frozen at the glass transition temperature and then thin slices of several micrometers were cut. Therefore a very flat surface is obtained. The opposite side of the prepared surface is glued to a metal chip, which is then fixed on the stage of the AFM using a magnet system. Care should be taken considering the following aspects. The prepared surface has to be parallel with the bottom (glued) surface and the substrate, to avoid a tilted image and the corresponding artifacts. Nevertheless the amount of glue used to fix the sample on the substrate should follow the principle "ass less as needed". A high amount of glue can diffuse into the polymer matrix and thus affect the properties of the investigated sample.

3.2 Influence of the calibration

As described in a previous chapter the calibration of the AFM experimental set-up it is of crucial importance prior to any experiment. In the following it will be shown that a bad, or a lack of the calibration will lead to significant deviations of the final results.

A simple experiment was chosen to show the differences caused by a lack of calibration on the final results. Two different filled EPDM systems where chosen. The only difference

between the 2 samples was the amount of the curing agent. In sample A the curing agent was set to be 50% less as in the sample B; therefore as a result, the sample A will show a lower cross-link density.

Force-mapping experiments were performed as described in paragraph 2.1.5 on each of the sample. Two different experimental set-ups were chosen, a calibrated one and a not calibrated set-up. The experiment was repeated with 2 different cantilevers. The results of the force-mappings are shown in Fig. 3.5.

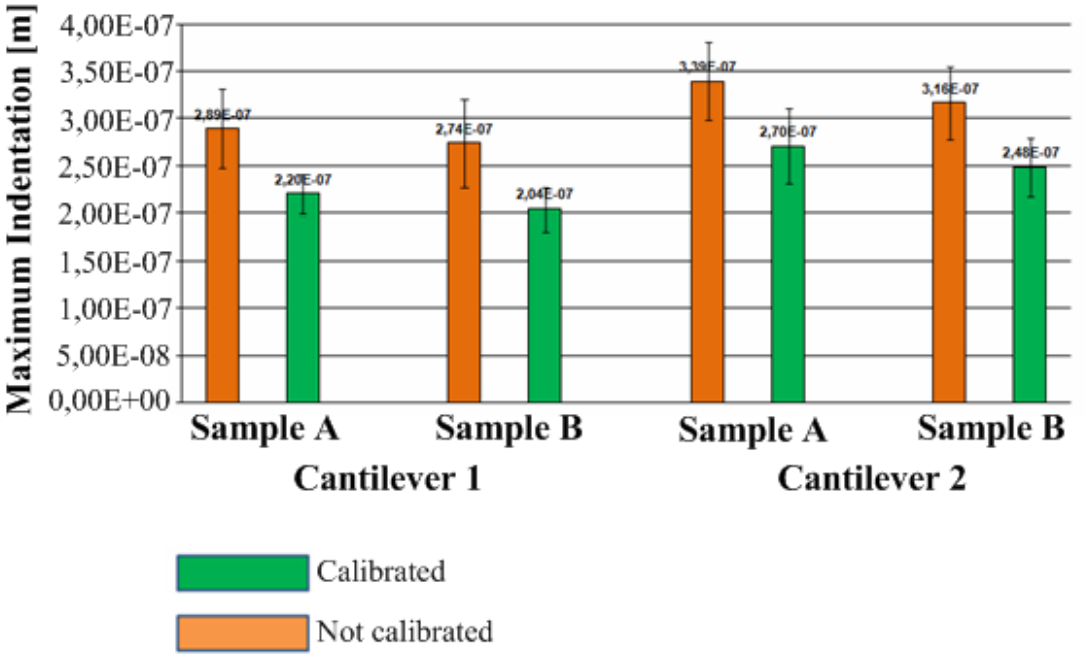

Figure 3.5: *Average values of the maximum indentation parameter extracted from a force mapping experiment.*

The values for maximum indentation were chosen for representation due to its high importance in micromechanical properties characterization. As a first observation we can say that the values measured on the same sample differ significantly when using a calibrated system (green bars) versus an uncalibrated one (orange bars). The obtained values are higher with about 30% in average in case of the non calibrated set-up compared to the calibrated one. This is a significant difference considering that the differences between the two samples (A

and B) are smaller than 15% as can be observed in Fig 3.5. Therefore a good calibration of the experimental set-up is mandatory prior any experimental procedure in order to avoid influences caused by artefacts and lead a false interpretation of the results.

The experiment was repeated with a second cantilever. The differences between the calibrated and not calibrated systems remain similar as with the first cantilever. However differences in results appear between the 2 cantilevers. This aspect will be discussed in the following chapter.

Although a calibration is required most of the time, in some cases when a fast comparison between two samples is needed in terms of relative hardness, the calibration process can be skipped. Figure 3.5 shows that even in case of an uncalibrated system, the relative difference or the trend between the two samples remain similar. However, any procedure other than fast relative comparison between the samples requires a good calibration, since the measured values are directly used in other calculations such as E-modulus.

3.3 Influence of the tip shape of the cantilever

A further aim of the experiment presented in the previous chapter (Fig 3.5) was to check the influence of the tip shape of the cantilever on the results, more exactly the micromechanical properties of a sample. As described in Fig. 3.5 cantilever one, represents a used cantilever while cantilever two is a fresh one. Considering the same parameter as described earlier, the maximum indentation, we can observe strong deviations between the two experimental setups.

Cantilever one (Fig 3.5) was conditioned prior the experiment described above. Several thousand indentations were acquired with the purpose of modifying the shape of the tip. This means the tip radius is drastically increased compared to a fresh, unused cantilever (cantilever 2 in Fig. 3.5). As described in chapter 4.1, the shape of the cantilever can be quantified using the Villarubia's [35] procedure, as a tip area function.

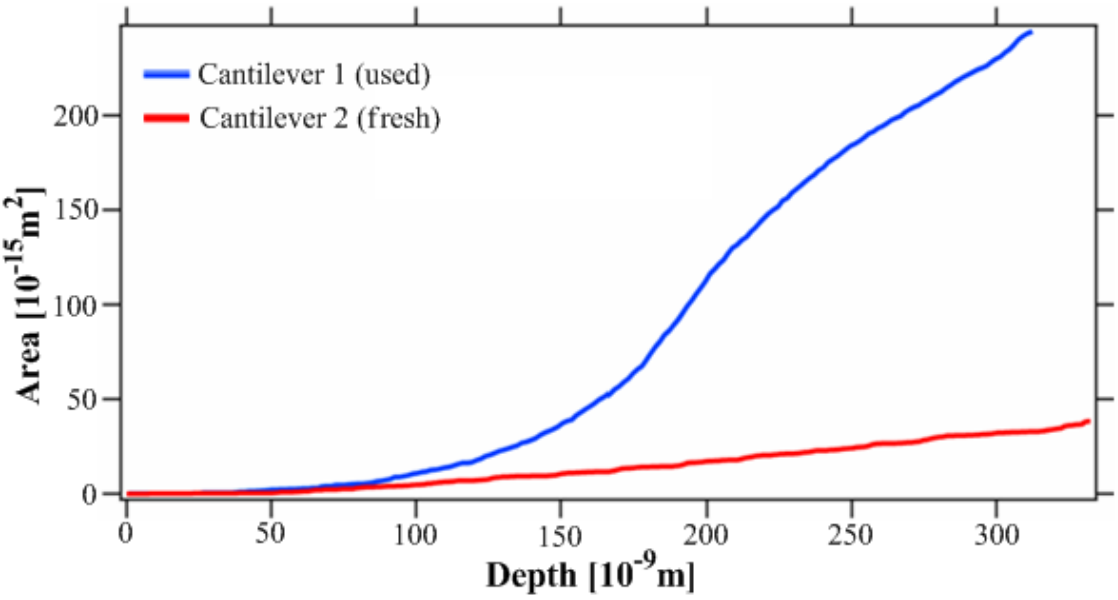

Figure 3.6: *Tip area functions of the cantilevers used for this experiment (fresh and used) determined using the Villarrubia's [35] procedure, described in chapter 4.1.*

Figure 3.6 presents the differences in the tip area functions between the two cantilevers. In case of cantilever one, a strong increase of the area as a function to the distance from its apex, is to be noticed. This means that cantilever one is blunter compared to the second one.

Due to these changes of the shape of the tip, strong deviations of the maximum indentation values are recorded between the two experimental setups (Fig 3.5). The set point for the experiments is kept constant in both cases. Therefore a change of the shape of the cantilever will induce a change in the measured values. As observed in Fig. 3.5 a fresh cantilever returns higher values for the maximum indentation compared to the used one. The relative differences

between samples A and B remain similar as with the used cantilever. However the absolute values in case of fresh cantilever are higher with approximately 30%.

4. Determination of the tip shape of a cantilever

A major drawback for an accurate determination of micro mechanical properties by using force-distance curves is the inaccuracy of the tip shape and radius. It will be shown later that small changes of the tip shape can have big influences on the calculated results. This is of significant importance due to the fact that it is generally accepted that the tip shape changes during measurements. All the measured forces depend on the overall tip shape.

Most of the earlier work done in this field [36-39] used a model for describing the tip shape, and consequently the contact area of the tip, which is mandatory for the E-modulus calculation. The most common model shapes used for the tip are either conical, or tetragonal pyramidal. In real cases, due to tip sample interaction, even with a predetermined shape of the tip before the measurement, the tip is likely to suffer changes during the measurement process as shown by Mermut [40] and later in the present work. Any theoretical model of the shape of the cantilever tip becomes therefore inaccurate for the calculation. Bedoui et al [41] suggested a method to quantify the contact area while performing indentations on plastic materials. The indentation would leave a fingerprint on the investigated surface, which will be later quantified using the tapping mode. The method is suitable for plastic materials only, for which the elastic deformation is neglectable. Other research groups [42-44] have used the SEM images to characterize the tip shape and thus the contact area.

In this work we propose to experimentally quantify the tip shape and to consider it in the analysis as a real time determined parameter. This procedure reduces the uncertainties that arise from the tip shape. The principle that describes the tip shape calculation from AFM images has first been studied by Villarubia [35]. He used the blind reconstruction method, to determine the worst tip shape given by the measured image. Our work applies the method of blind reconstruction suggested by Villarubia [35], using the image obtained from a calibration

grid (Fig. 4.3). The tip shape is illustrated as a function of the projected contact area versus the distance from the apex of the tip (Fig. 4.4).

To deal with the uncertainties related to tip shape, we applied the tip estimation procedure described by J.S. Villarrubia. The shape of the tip can be estimated applying functions of the morphology (dilation, erosion, translation, etc) [35]. As shown in Fig. 4.4 this calculation leads to the worst tip geometry that is admissible to image the measured surface. Furthermore, independent from the real tip geometry, the nature of the surface structures also influences the estimation. Figure 4.1 schematically illustrates the blind reconstruction procedure. An infinite blunt tip R_0 with a reference point is considered as default (Fig 4.1a). This kind of tip is located to each point P_1, P_2, P_n of the surface image (Fig 4.1b). Removing the part of the tip that does not match the surface image gives a restricted tip (R_1, R_2, R_n) for each point as shown in Fig 4.1b. By subtracting the entire number of restricted tips (R_n) from the initial blunt tip (R_0), the mirrored picture of the worst tip able to give the current image can be identified (Fig. 4.1d). To calculate the E-modulus with the help of the tip estimation, it is important to get an accurate estimation that covers the whole contact indentation depth from a force curve (Fig. 4.2).

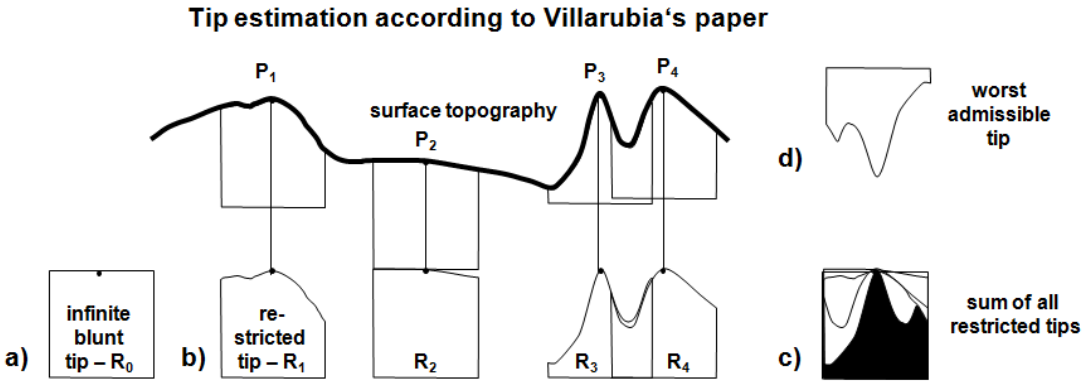

Figure 4.1: *Illustration of the tip estimation procedure introduced by Villarubia [35]. An infinite blunt cantilever R_0 is considered as a reference (a). The reference is located trough each position of the sample P_1, P_2, P_n and a restricted tip R_1, R_2, R_n is obtained from each location (b). Subtracting all the restricted tips from the reference tip, the mirrored picture (c) of the worst admissible tip (d) required to image the surface is obtained.*

Since the rubber sample requires a crio-microtome preparation, the height of the surface structures ranges between 20 and 30 nm. Therefore, the blind reconstruction returns accurate results for tip area functions with a depth in the range of the measured surface structures.

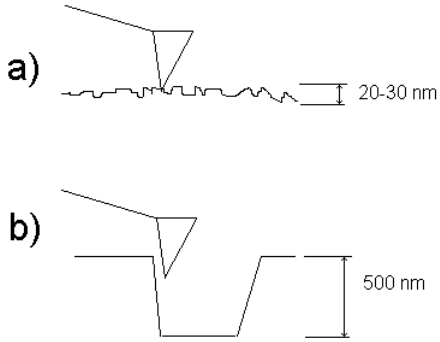

Figure 4.2: a*) Cantilever investigating a polymer surface. b) Cantilever investigating a calibration grid.*

As shown later (Fig. 6.5 forces lower than 300 nN), at small indentations (lower than 30 nm) the standard deviation of the modulus increases. This is attributed to increasing surface effects at decreasing indentations. Therefore, in our experimental setup (set point for maximum force: 500 nN) we determined the E-modulus at indentations in the range of 100-400 nm (Fig. 4.2). Hence, the blind reconstruction of the investigated rubber samples is not sufficient to describe the tip shape over a range of 400 nm (Fig. 4.2a).

Using a special artificial surface (Fig. 4.3), with sidewalls higher than the contact indentation depth and angles smaller than the opening angle of the tip (Fig. 4.2b, 4.3), a more realistic tip area function for the higher indentations, used in our experiments, can be obtained. Figure 4.4 presents tip area functions derived from a measured image of the sample and the grid according to the drawings in Fig. 4.2.

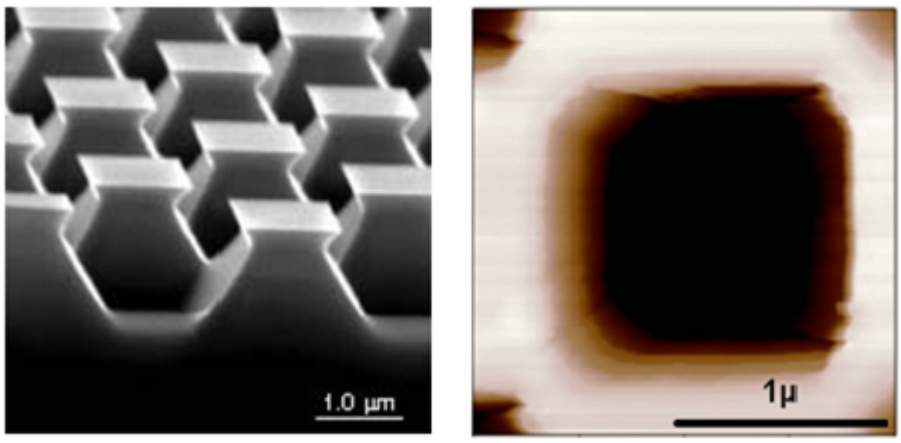

Figure 4.3: *TGX calibration grid used for tip estimations. a) Image obtained using SEM. b) represent height image measured with the AFM.*

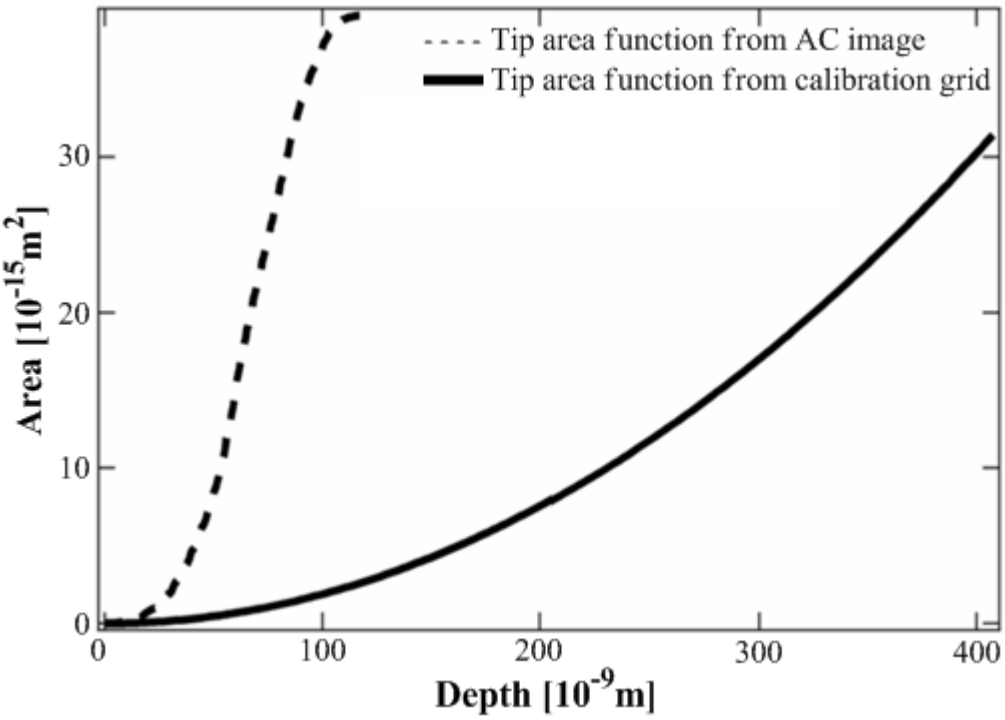

Figure 4.4: *Tip area functions from an AC image of the sample and from the calibration grid.*

It can be observed that the tip area function obtained from the measured topography image (Fig. 4.4 the interrupted line) is in good accordance to the area function from the calibration grid only in the initial part of the graph. The deviation that further appears between the two curves is attributed to the height structure difference for the 2 surfaces used (sample topography and the topography of the calibration grid). The sample has structures with heights up to 30-40 nm, so will return accurate area functions only in this range. Therefore for these types of estimations the grid is a better choice.

When performing a simple scan over the grid surface, an image like the one presented in Fig. 4.3b is obtained. The centred structure in Fig. 4.3b is helpful to obtain a complete profile of the tip, because it comes into contact with its outer limits from each side. With this method even strong deviations (Fig. 4.5a, left) from the original tip geometry (Fig. 4.5a, right) can be taken into account for the calculations of the tip area function and the E-modulus.

a)

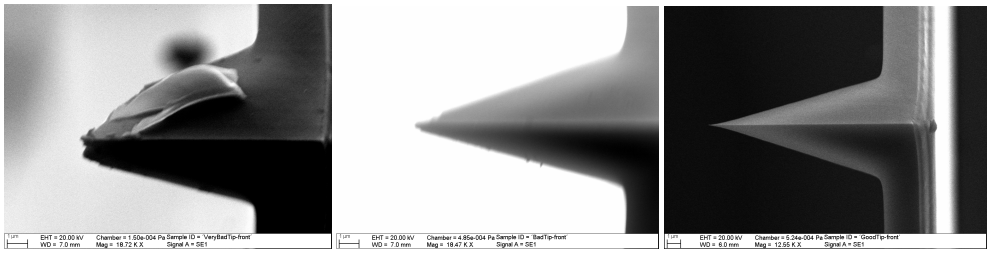

b)

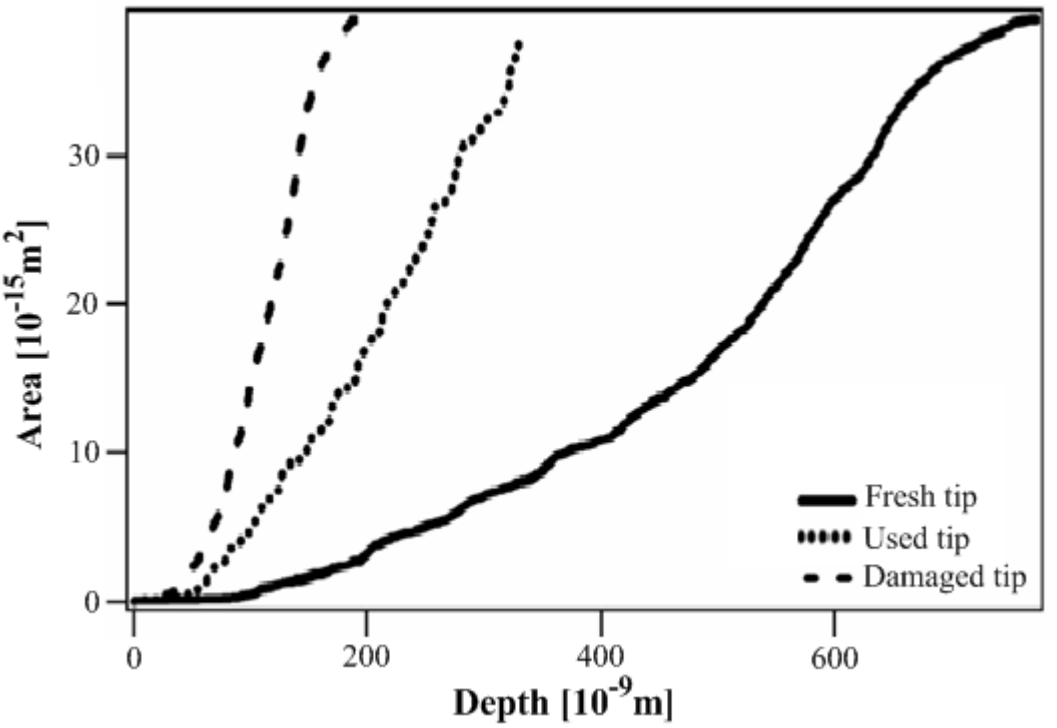

Figure 4.5: *a) SEM images of three different cantilevers, a new one (right), a used one (middle), and a damaged one (left). b) Tip area functions of the three cantilevers calculated using Villarrubia's estimation procedure.*

SEM images of a new, a used and a damaged cantilever reveal clear differences (Fig. 4.5a). The solid line in Figure 4.5b represents the area function of a fresh tip, while the dotted lines correspond to used ones.

5. E-Modulus calculation using AFM force-distance curves

The calculation of the E-modulus by using nanoindentation data gives the possibility to differentiate heterogeneities of the elastic moduli at the nanoscale. In the ideal case of perfect plastic deformations, the method described by Oliver and Phar [45] would fit very well, but in real cases, deformed materials contain also a degree of plasticity. This effect has to be taken into consideration while performing the calculations. In particular, the geometry of the indenter (in our case the tip from the cantilever) must be well known to obtain accurate results. For calculation of the E-modulus only the upper part from the force curve will be taken into account, because right after that the set point has been reached, and the piezo drive starts to retract, so the initial part of the material recovery is determined largely by the elastic deformation, $E_{elastic} >> E_{plastic}$. In this case the theory of elastic deformation can be used successfully.

Dealing with two elastic bodies, the cantilever and the sample, which interact with each other, a reduced modulus E_r can be introduced:

$$\frac{1}{E_r} = \frac{(1-\vartheta^2)}{E} + \frac{(1-\vartheta_i^2)}{E_i} \tag{5.1}$$

where E and ϑ are Young's modulus and Poisson's ratio of the sample, and E_i and ϑ_i are the same parameters for the indenter. If Young's modulus of the indenter is much higher than the modulus of the sample (rubber in our case), equation 1 becomes

$$\frac{1}{E_r} \approx \frac{(1-\vartheta^2)}{E}. \tag{5.2}$$

The interest in experiments that characterize the sample response after an applied load, and determine values for the elastic modulus, began in early 1970's [46-48]. Then, instrumented

micro hardness devices were used to determine load-displacement curves like the one presented in Figure 1. These curves where then analyzed with the following equation

$$S = \frac{dP}{dh} = \frac{2}{\sqrt{\pi}} E_r \sqrt{A} \tag{5.3}$$

where $S = dP/dh$ is the experimentally measured stiffness of the very beginning region of the unloading curve, E_r is the reduced modulus mentioned in Equation 2, and A is the projected area of the contact between the indenter in contact with the sample. This equation has its origins in the elastic contact theory. It was developed first for a conical indenter, but later Buylchev et al.[47] have shown that it can be applied to other geometries (trigonal pyramid, rotational paraboloid) as well [46], if one takes into account a 3.4% deviation [49].

Combining Equation 3 and 4 one obtains the equation that returns the E-modulus:

$$E = \frac{2}{\sqrt{\pi} S} (1 - \vartheta^2) \sqrt{A} \ . \tag{5.4}$$

Equation 4 contains a parameter that has to be accurately determined: the projected contact area A between the indenter and the sample. A tip area function (Eq. 5) was introduced to describe the cross-sectional area of the indenter as a function to its distance from the tip of the cantilever. Knowing the indentation depth and having the tip area function, one can calculate the area of the indenter at a certain indentation depth

$$A(h) = \ ah^m \tag{5.5}$$

The E-modulus can be determined considering the exponential fit of the very beginning of the unloading part in the force-distance curve (Fig. 1), using the equation 6.

$$\mathrm{P} = a\mathrm{h}^m \tag{5.6}$$

Earlier studies used the entire unloading curve to perform the fit, but very high values (far from the macroscopic values) of the resulting E-moduli were obtained. This inaccuracy can be attributed to the influence of both, the elastic and the plastic components during the recovery of the material. In this study, only the upper portion of the unloading curve was taken into account. At the time when the maximum indentation occurs, the material suffers the highest stress. Once the indented surface starts to recover, the recovery is dominated by the elastic component. We chose for our E-modulus calculation only 10% from the unloading curve, i.e. the portion between 95 % and 85 % of the curve. The upper 5 % were intentionally left out, because in that regime other interactions can occur between the cantilever and the sample, interactions that can lead to inaccurate results (e.g. slip of the cantilever or sensitivity of the piezo actuator when it changes the direction from indentation to retracting).

6. AFM nanoindentation to determine Young's modulus of different EPDM elastomers

AFM nanoindentation is investigated as a method to determine micromechanical properties of polymers. It is generally accepted that the shape of the tip of the cantilever in a standard AFM setup changes. Since the shape defines the projected contact area it is a parameter which is directly proportional to the elastic modulus and any change affects the accuracy of the results. The method suggested in this paper relies on the introduction of an experimentally determined tip-area function. Values for Young's modulus were calculated for EPDM samples with different degrees of curing and different degrees of crystallinity. The calculated results correlate well with values determined by DMA. The degree of crystallinity has a higher impact on the mechanical properties of the material than the degree of curing.

6.1 Introduction

Atomic force microscopy (AFM) [5] has become an indispensable tool in various areas of interests related to material science. It has proven itself to be a reliable tool in quite different fields, such as biology, chemistry and physics.

Historically, the first main application of the AFM was to analyze the repulsive and the attractive forces between a given sample surface and an AFM tip, and thus mapping topography of the material with nanometer resolutions and phase contrast in selected regions of the sample. Later on, contact-mode AFM was used to quantify the surface mechanical properties of the sample. This requires the determination and analysis of the dependence between the force applied to the tip and the indentation depth, represented in the so-called force-distance curve. In a simple analysis, this force curve gives access to several important

parameters related to micromechanical properties: maximal indentation (the indentation depth depends on the stiffness of the investigated region, when a constant force is applied as a set point), adhesion between the cantilever and the sample and elastic/plastic deformation energies.

As a tribute to the trend of building smaller and smaller parts, the understanding of the micromechanical behavior of reduced-size materials has become a necessity. A view at a reduced scale may reveal material properties different from those of the bulk state. For example standard hardness measurements can be adjusted to nanoindentation measurements, and heterogeneities at nanoscales can be mapped. It is of a critical importance to locate heterogeneities at the nanoscale to accurately be able to predict the behavior of the bulk material.

Important factors, such as surface preparation, surface orientation, the radius of the indenter, and even the composition of the indenter, pay an important role in the acquired information [50-53]. Several research groups [54-57] performed extended studies analyzing the tip sample interactions in more detail. Until to now most of the studies using the AFM in force mode [54-57] concentrated on extracting information from the attractive and transition regions of the force curves. Only a few groups have paid attention to the examination of the contact region, or the repulsive part of the force curve (Fig 6.1) [58].

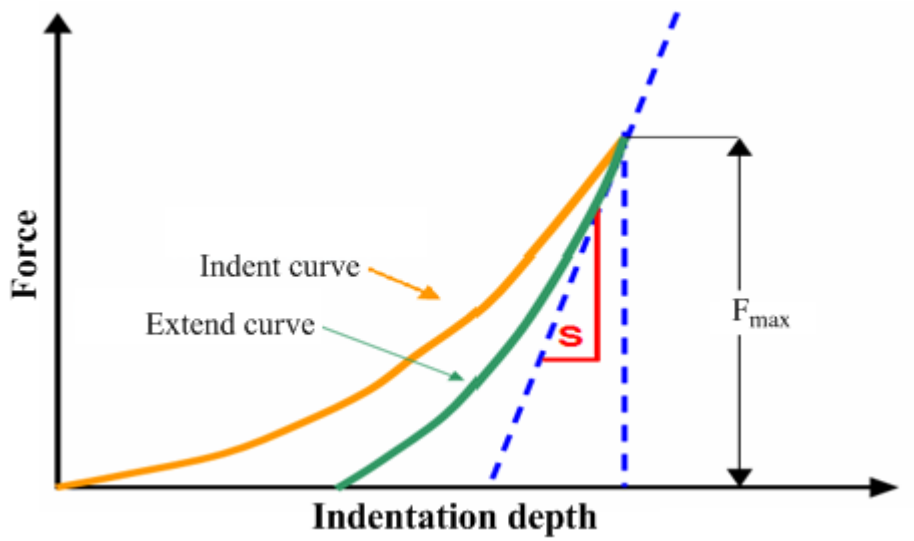

Figure 6.1: *Typical force versus indentation curve obtained in an AFM indentation cycle.*

The pioneering work in this area was done by Oliver and Phar [45, 59]. They used a micro indenter and calculated elastic moduli for different materials varying in stiffness such as aluminum, sapphire and quartz, based on the Hertz model for describing the contact between two elastic spheres, and applying equations derived by Sneddon. Bielinski's team [60] has applied the principle described by Oliver and Phar [45, 59] to study the aging of different rubber composites using micro indenters. Herrmann [61] has built a similar indenter to characterize micromechanical properties of elastomers in his work.

Later on Vanlandingham [38, 62] replaced the micro indenter with the AFM, and was able to obtain E-modulus values on polyurethane applying the method described by Oliver and Phar to force indentation curves from AFM experiments. Lin et al [63] have improved the method by taking the Hertz model which describes the contact between two elastic spheres without adhesion, and applying it to the theory of Jonshon et al [64, 65], which considers also the adhesion factor. With this method they were able to generate AFM maps of Young's modulus on different gels with a resolution of 30 x 30 μm^2.

Nakajima et al [37, 39] have used the same Hertz model to successfully analyze elongated rubber materials at different elongations in terms of E-moduli. However, when comparing their theoretical model to standard DMA tests they find that the calculated values for the E-modulus are higher by factors of 10^1-10^2. They argue that the reason for these differences is that the indentations are performed perpendicular to the elongation direction, which lead to a much stiffer behavior. Also they argue that the indenter properties such as tip shape and spring constant plays a role.

So far all earlier work done in this field [10, 14, 43, 45, 55, 61-63, 66, 67] uses a model for describing the tip shape, which is used for the E-modulus calculation. The most common model shapes for the tip are either conical, or tetragonal pyramidal. In real cases, due to tip sample interactions, even if we have a predetermined shape of the tip before the measurement, the tip is likely to suffer changes during the measurement process: any theoretical model of the shape of the cantilever tip becomes therefore inaccurate.

In this work we propose to improve the E-modulus determination by using AFM and by quantifying the tip shape and adding it to the equation. This procedure eliminates the uncertainties coming from the tip shape.

The principle of describing the tip shape has been first studied by Villarubia [35]. He used the blind reconstruction method, to determine the worst tip shape which can give the measured image. This work applies the method of blind reconstruction suggested by Villarubia, except for a small difference: the image used for estimating the tip shape is obtained from a calibration grid (Fig. 4.3). A description of how this estimates the tip shape and the theory of the E-modulus was given in chapters 4 and 5.

6.2 Theoretical aspects

The calculation of the E-modulus using nanoindentation data from AFM gives the possibility to differentiate heterogeneities of the elastic moduli at the nanoscale. In the ideal case of perfect elastic deformations the method described by Oliver and Phar [45] would fit very well, but in real cases, deformed materials contain also a degree of plasticity. This effect has to be taken into consideration while performing the calculations. In particular the geometry of the indenter, in our case the tip from the cantilever, must be well known to obtain accurate results. For calculation of the E-modulus only the upper part from the force curve will be taken into account, because right after the set point has been reached, and the piezo drive starts to retract, the initial part of the recovery of the material is determined largely by the elastic deformation, $E_{elastic} >> E_{plastic}$. In this case the theory of elastic deformation can be used successfully.

6.3 Experimental

To check the viability of the method, some rubber samples with extreme properties were chosen, an amorphous one Buna EP 3440 and Buna EP 6770, an EPDM with a high amount of ethylene groups which confers a high degree of crystallinity. Each of these two polymers was mixed with 48 phr Carbon black N115, and 5 phr cross linking agent (dicumyl peroxide). Unfilled samples were also prepares and the results are included in this study. Each sample was vulcanized to 50 % and to 100%, resulting in a total of 8 samples. The following notations are introduced (Table 1): FHC50 (filled highly crystalline polymer cured to 50%), FHC100 (highly crystalline polymer cured to 100%), FLC50 and FLC100 (amorphous polymer cured to 50% respectively 100%). For the unfilled materials, the letter F is substituted with letter N.

Table 6.1. *Samples description.*

	Degree of Crystallinity	Degree of vulcanization	Sample description
F	HC	50	Filled EPDM, high crystallinity with 48phr CB, 50% curing
		100	Filled EPDM, high crystallinity with 48phr CB, 100% curing
	LC	50	Filled EPDM, amorphous with 48phr CB, 50% curing
		100	Filled EPDM, amorphous with 48phr CB, 100% curing
N	HC	50	Unfilled EPDM, high crystallinity with 48phr CB, 50% curing
		100	Unfilled EPDM, high crystallinity with 48phr CB, 100% curing
	LC	50	Unfilled EPDM, amorphous with 48phr CB, 50% curing
		100	Unfilled EPDM, amorphous with 48phr CB, 100% curing

DMA measurements were performed on each of the sample, to determine the macroscopic E-Modulus. In case of the AFM measurements, three different reproducible locations were first scanned using the tapping mode, and on each of the locations a force mapping experiment of 60x60 curves was executed. For comparison with the DMA results, only average curves from the force mapping experiments were used.

6.4 Results and discussions

The E-modulus can be determined with the help of an exponential fit of the very beginning of the unloading part of the force-distance curve (Fig. 1) using the equation 6.

$$P = a h^{m} \tag{6.1}$$

Earlier the entire unloading curve was chosen for the fit, but problems came up in this case, with the very high values of the resulting e-moduli, which were far from the macroscopic

values. This can be attributed to the influence of both, the elastic and the plastic components during the recovery of the material. In this study, only the upper portion of the unloading curve was taken into account. As the time when the maximum indentation occurs the material suffers the highest stress. Once the indented surface starts to recover, the recovery is dominated by the elastic component. We chose for our E-modulus calculation only 10% from the unloading curve, i.e. the portion between 95 % and 85 % of the curve. The upper 5 % were intentionally left behind out in that regime other interactions can occur between the cantilever and the sample such as slip of the cantilever or sensitivity of the piezo actuator at the moment it changes the direction, from indentation to retracting, which may lead to inaccurate results.

Table 6.2. *E-modulus values (Pa) from DMA measurements and AFM calculations.*

		Filled		**Unfilled**	
		HC	**LC**	**HC**	**LC**
AFM Emodul	T50	4.77E+07	2.99E+07	6.99E+06	2.48E+06
	T95	5.27E+07	3.26E+07	7.66E+06	3.18E+06
DMA Emodul	T50	5.96E+06	2.96E+06	2.90E+05	1.10E+05
	T95	6.36E+06	3.05E+06	3.00E+05	1.50E+05

DMA measurements were performed at room temperature and 1 Hz frequency (Table 6.2). AFM measurements were performed in a manner that reproduces the conditions from the DMA measurements, i.e. at room temperature and one indentation per second (Table 6.2). However the frequency of the DMA measurements cannot directly be compared with the frequency of the AFM measurements, because for the AFM measurement 1 Hz means one indentation per second, while in DMA 1 Hz represents one shear cycle per second.

The moduli determined by both methods correlate linearly on double linear scale (Fig. 6.2). This is an important first step in the process of correlation of the 2 methods, and moreover, a correlation between macroscopically determined values, and the microscopically ones. The graph shows similar trends for both ways of investigation. Applying values for tip area function from an unused cantilever for each of our experiments would mean that the evolution of the tip shape is not taken into account. Doing so, we get very high values of modulus (Fig. 6.2). Therefore it is important to take into consideration the tip shape before and after each measurement. Moreover the linear correlation between AFM and DMA disappears when the tip area function is omitted.

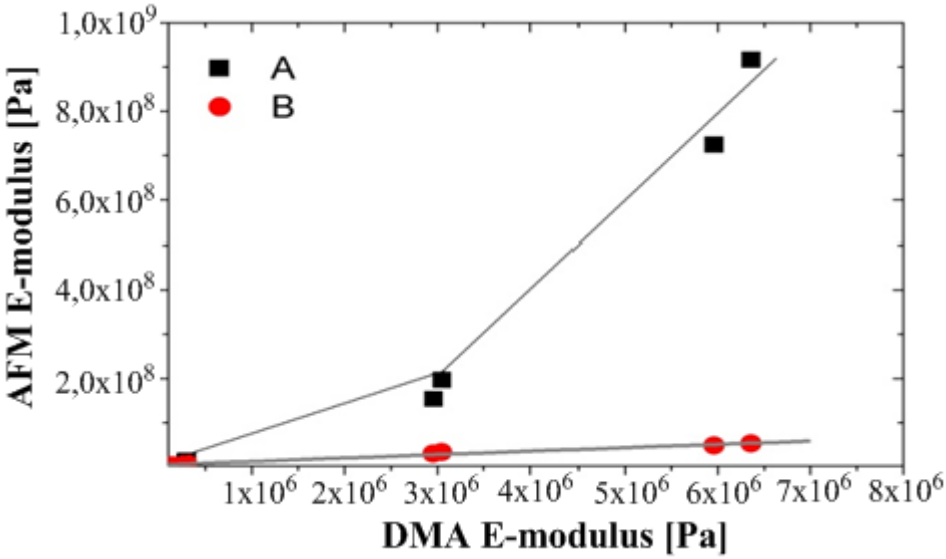

Figure 6.2. *Schematically representation of the correlation between the values of the E-modulus measured with DMA and the calculated values using AFM for filled and unfilled as well as full cured and 50% cured materials. The circle shape dots correspond to modulus values determined applying the tip estimation after each measurement. The square dots are values calculated using a single estimation for all measurements.*

Interestingly, values determined with the two methods differ by a factor of about 8 in the case of filled materials, and a factor of about 20 in case of unfilled materials. These differences in the values of the E-modulus can be explained when taking a closer look at the differences

between both methods. DMA uses shearing to determine the E-modulus, while with the AFM the modulus is computed after a recovery from a compression. The factor differences can be associated with the filler-filler and polymer-filler interactions which are present in the filled material. These interactions seem to have a higher impact on the elastic properties of the material in shear experiments than in the compression experiment. For filled elastomers other interactions such as filler-filler, polymer-filler interactions may play a role, which may impact the results. The presences of these interactions in filled materials are particularly evident when looking at the higher factor differences in the case of unfilled materials. Also with the DMA the bulk modulus is measured, while with AFM local moduli are determined at microscopic scales, where sample heterogeneity and the random nature of rubber at molecular level becomes more important. The third, and most important observation, is that a DMA measurement is based on the recovery after an elongation of the sample, while with AFM the E-modulus is determined from a recovery after a compression. With these observations in mind, the method seems to be a promising tool of probing locally distributed E-modulus values at micro and nanoscales.

A further experiment was performed to validate the values for the E-modulus determined by AFM. It consists of modifying the frequency of the measurements. In both cases, DMA and AFM, the frequency was increased and the evolution of the E-modulus was recorded. However in the case of AFM measurements, when we talk about frequency we refer to indentation speed. As expected, an increase of the frequency lead to a slight increase of the E-modulus in case of DMA experiments as can be observed in Fig. 6.3. Doing the same with the AFM experiments by increasing the speed of the indentation we obtain a similar trend (Fig. 6.4).

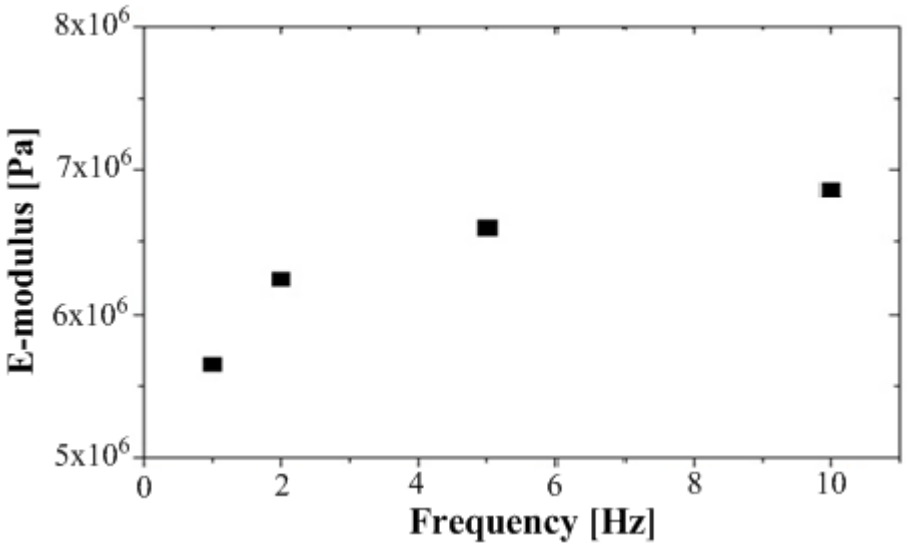

Figure 6.3: *E-modulus values plotted versus the frequency in the DMA measurements.*

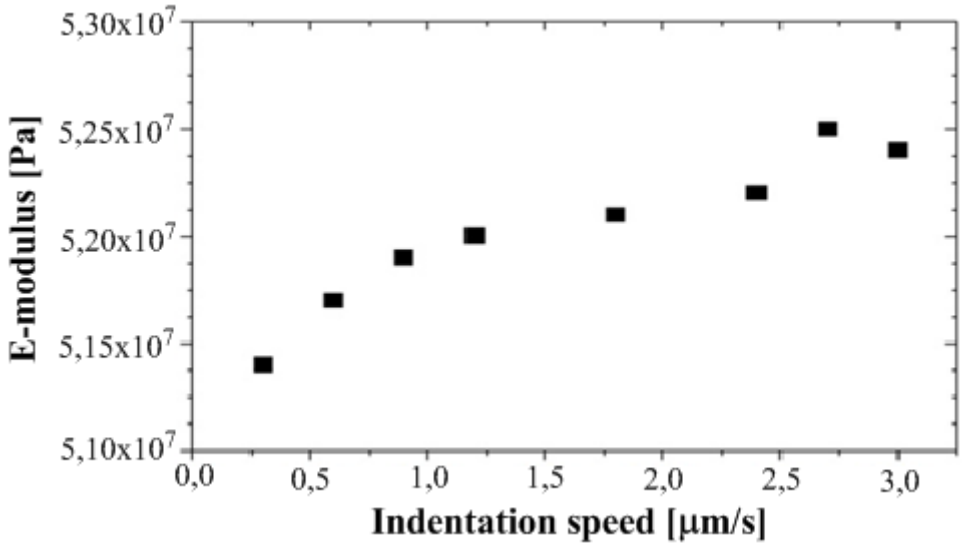

Figure 6.4: *Variation of moduli obtained by AFM, as a function of the indentation speed.*

In both of the cases we notice an increase of E-modulus as a function of frequency. Fillers and Tschoegl [68] mention in their studies of mechanical properties of polymers under applied pressure, that a transition similar to the glass transition occurs when the applied pressure is increased and reaches a certain value. It is called the glass transition pressure. They also mention that the "glasses" formed by the application of pressure seem to be denser than those

which are formed by reduction of the temperature. It is commonly expected that denser "glasses" show a higher modulus [69, 70]. Following the line of thought, a variation of the set point force applied during indenting should lead to different moduli, more exactly, an increase of the maximum force would result in an increase of the modulus. Using this approach, we tested again the accuracy of the values measured with the AFM, by varying the applied maximum force (Fig. 6.5).

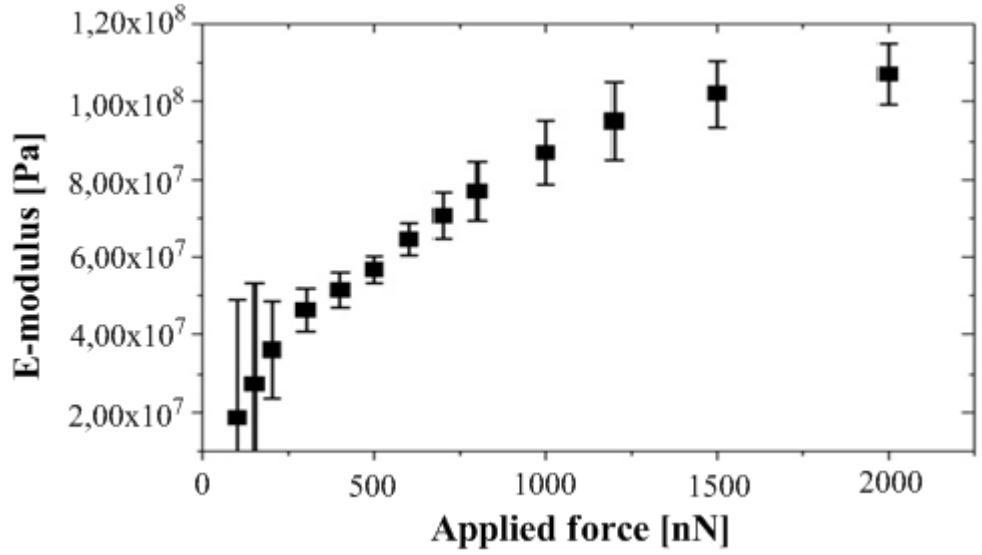

Figure 6.5: *Plot of calculated E-Modulus as a function of the maximum force applied.*

The maximum force values were varied between 100 nN and 2 µN. This was the optimum range of the investigation limited by the experimental set-up. Using forces lower than 100 nN provided inaccurate measurements due to the increasing influence of background noise. Moreover, adhesion forces gain impact on the overall tip-sample interactions. Forces higher than 2 µN are also not recommended for the cantilevers as used our experiments, due to their high sensitivity. The risk of destroying the cantilever increases with the force applied.

Interestingly when lowering the indentation forces we reach values of moduli comparable with the DMA ones. However low indentation forces are not subject of this work since the reproducibility of the results is very low. The optimum applied force for the indentations was determined to be about 500 nN.

As expected, one observes the increase of the E-modulus with increasing the applied force and the indentation speed as well.

6.5 Conclusions

The introduction of an experimentally determined tip area function in the equation for the E-modulus calculation using AFM leads to successful results, by obtaining a better correlation with the DMA measured values. With this method we eliminate an unknown parameter from the E-modulus equation which until now had to be estimated. Using experimental data to replace the cross-section area of the indenter makes the determination of the modulus using AFM nanoindentation more accurate.

The comparison of the E-modulus values determined by AFM and DMA shows that the data from both methods correlate well. Even though the values measured by the AFM are still high, the trend is the same. One observes that the cured material shows a higher modulus, than the half-cured materials, and that the highly crystalline material is stiffer than the one with low crystallinity.

To prove that the results are not arbitrary we showed how the modulus changes with the variation of the frequency in both AFM and DMA setups. In each case the modulus increases with the frequency.

However the AFM does not for compete with standard DMA tests regarding modulus determination. DMA applies to bulk materials and probing macroscopic mechanical properties, while AFM measurements apply to microscopic scales. The importance of the AFM method is that it enables the imaging of E-moduli at micro- and even nano-scales, with better accuracy, due to the introduction of the experimentally determined tip area function. In this case heterogeneities at very small scales can be identified, providing information which cannot be obtained with standard physical testing machines. In future work, materials with different heterogeneities at micro-scales will be investigated with the help of AFM calculated E-moduli, which show minimal or no difference in standard physical tests. Understanding the behavior at micrometer scales will also improve our understanding of the material properties at macroscopic scales.

7. Effects of induced heterogeneities in semi-crystalline EPDM elastomers

7.1 Introduction

Atomic Force Microscopy (AFM) was successfully used to characterize micron and submicron scaled structures in semi crystalline EPDM compounds (Fig. 7.1). Micromechanical properties in terms of E-Modulus and surface deformation were used to characterize induced heterogeneities. An annealing process was done to create different local microscopic heterogeneities. The basic mechanical properties like tensile experiments or E-modulus were nearly independent from the cooling rate. In the present work we used the AFM successfully to demonstrate that at low cooling rates the size of observed structures and the heterogeneity of the material are increased. Even more the average value of the local E-modulus at small amplitudes fit with the macroscopic E-modulus measured with the DMA [71]. This example confirms that the micromechanical analysis leads to a more detailed characterization of elastomer materials.

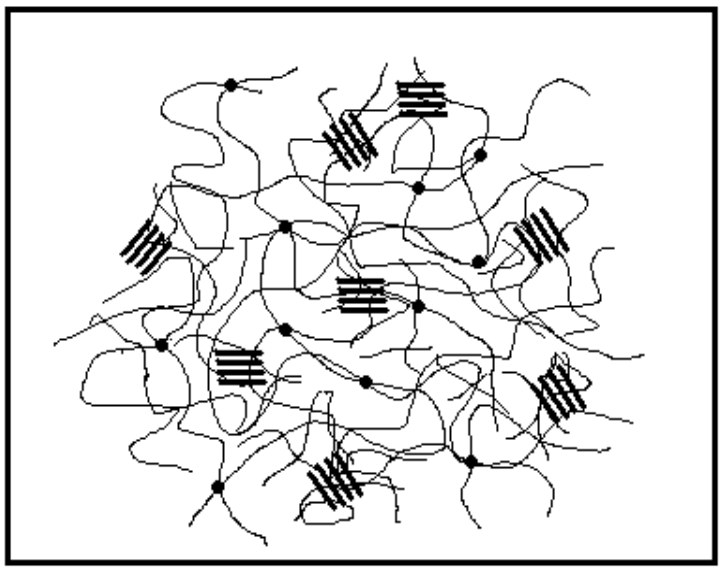

Figure 7.1: *Mixed amorphous crystalline polymer matrix*

Semi crystalline polymers are often use in modern application due to their improved properties. They combine the properties of amorphous polymers (i.e. flexibility at low temperatures) with the stiffness of the rigid parts (crystalline regions). In such compounds, the amount of crystalline phase determines the macroscopic mechanical properties. There are several investigation methods which can observe and quantify the crystalline fractions, such as XRD or magnetic resonance, even electron microscopes, but the atomic force microscope can visualise the distribution of such "hard" phases, and even determine local micromechanical properties in terms of hardness or modulus.

A heat treatment applied to a filled semi crystalline sample can cause several effects. As described by Sanchez [72] in his work a heat treatment leads to heterogeneities in the sample caused by the filler-filler flocculation. Nevertheless, exposure to high temperatures could also lead to the melting of the crystalline structures. At high temperatures the chain mobility increases and thus to "unpack" the chains, leading to a destruction, or melting of the so called crystallites. Allowing the polymer to cool down to room temperature, the polymer chains are able to pack themselves back into an ordered structure. However this is strongly dependent on the cooling rate. A slow cooling rate would allow the polymer chains to create a crystalline structure while a fast cooling rate, would immobilize the polymer chains faster, thus the overall particles size will be reduced [73, 74]. A filled semi-crystalline material was used and heterogeneities were induced using an annealing process. It is of a critical importance to locate heterogeneities at the nanoscale to accurately be able to predict the behaviour of the bulk material.

This chapter is aimed toward identifying and mapping heterogeneities at submicron scale on samples with comparable macroscopic properties. Well known heterogeneities will be induced on a filled EPDM elastomer with a high percent of ethylene content by heating up the samples and using two different cooling rates. The characterization of the induced

heterogeneities will be further discussed in this chapter. AFM will be used as main investigation tool.

7.2 Experimental

In the present study an EPDM with a high amount of ethylene fraction was chosen. Due to high amount of ethylene groups, the overall crystallinity of the polymer is increased. A commercially EPDM (Buna EP 6775) with 75% ethylene ratio was used as investigation polymer, filled with 48 phr Carbon Black N115 and 5 phr peroxide as vulcanizing agent. The samples were mixed in internal mixer and vulcanized for 30 min at 160^{o}C. Sheets of 180 mm x 80 mm x 6 mm were prepared from the vulcanizing press for investigation. Two rubber frames were annealed at 150^{o}C for 30 minutes. Right after annealing one of the sample is cooled down in a mixture of water and ice (sample a), and the other sample is cooled down slowly, in normal atmosphere at room temperature (sample b).

As investigation tools standard physical tests were performed on the samples to determine e-modulus, hardness, elasticity. DMA was also used to determine the macroscopic shear moduli. For the observation of the crystallite structures and micromechanical properties AFM was successfully used. Standard tapping mode method and force mapping measurements were used for sample characterization. According to the improved method described by the author previously [71], micromechanical properties in terms of E-modulus were also compared. A cryo-microtome preparation was employed to obtain flat surfaces.

7.3 Results and discussions

Table 7.1 illustrates the macroscopic mechanical properties determined using tensile tests of the reference sample (A) as well as the two different cooled samples (B fast cooled, C slow cooled). Analyzing the data in the Table 7.1 it can be observed that the mechanical properties of the annealed samples (B and C) are slightly decreased compared to the reference one (A). This can be explained by considering the preparation method of the rubber samples. A two roll mill was used for the preparation of the samples.

Table 7.1: *Mechanical properties of samples A to C*

EPDM High crystallinity, 48 phr N115 CB, 5 phr peroxide			
Sample	A	B[1]	C[2]
Hardness	80	79	80
σR [MPa]	29.1	27.8	26.7
σ50[4] [MPa]	2.7	2.5	2.5
σ100[4] [MPa]	4.1	3.9	3.9
σ200[4] [MPa]	11.3	10.8	10.7
σ300[4] [MPa]	23.8	23.2	22.7
εR[3] [%]	334.1	330.1	326.6
Elasticity	56	54	54

1- Fast cooled sample, 2- slow cooled sample, 3- elongation at break (in percent)

4- Tensile strength at (50%, 100%, 200% and 300%) elongations

Especially for anisotropic filler like fibres or layered silicate the orientation of the filler-filler networks [75] will not be destroyed during the vulcanization. Due to the high aspect ratio of these filler materials, anisotropic moduli are observed.

In Fig 7.2 the phase contrast of the tapping mode experiment shows a slight orientation. Single force curves performed in the low phase shift areas are comparable with the force

curves in Fig. 7.4, which were attributed to the filler clusters in the material. Therefore the slightly higher reinforcement of the reference material can be explained by the filler-filler networks.

Annealing the reference sample 30 minutes at 150^{o} C the orientation is removed. During the annealing the crystallites have been molten (40^{o} C) and the filler-filler flocculation lead to a relaxation of the orientation of the filler-filer networks [72, 76]. Both effects, the crystallization of the polymer and the filler-filler interactions are generated by the high cooling rate in ice water. Therefore smaller crystallites and filler clusters are expected. The effects of the orientation caused by the sample preparation are excluded, because the cuts were done perpendicular to the X-axis while the orientation shown in Fig. 7.2 has 45^{o} related to X-axis.

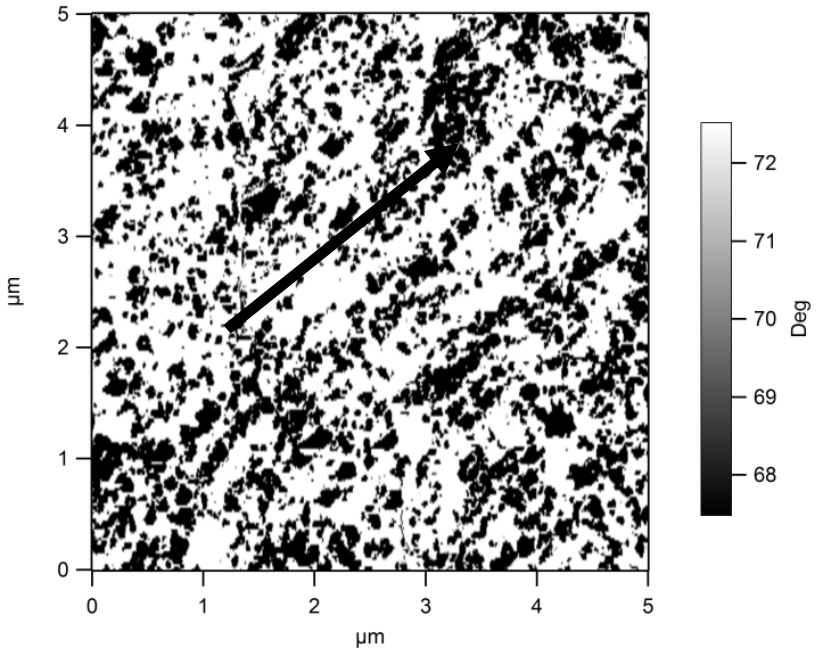

Figure 7.2: *Depict of the phase contrast of reference sample using AFM Tapping Mode. A slight orientation according to the arrow direction can be observed.*

Considering the work of Hou et al. [77] and Li [78] where they induced crystallization and an orientation of the crystallites by stretching on polymer materials to obtain improved mechanical properties, the higher modulus of our reference sample can be explained. Zhao [79] and Ben Daly [80, 81] also mention in their studies that the moulding process induces an orientation of the crystallites.

Heating up the sample to 150° C, the crystalline structures are melted, and combined with a filler-filler flocculation the orientation is reset. Cooling the sample will allow the crystallites to be formed back, their size being proportional to the cooling rate. Comparable effects are well known in the DSC analysis of semi crystalline polymers.

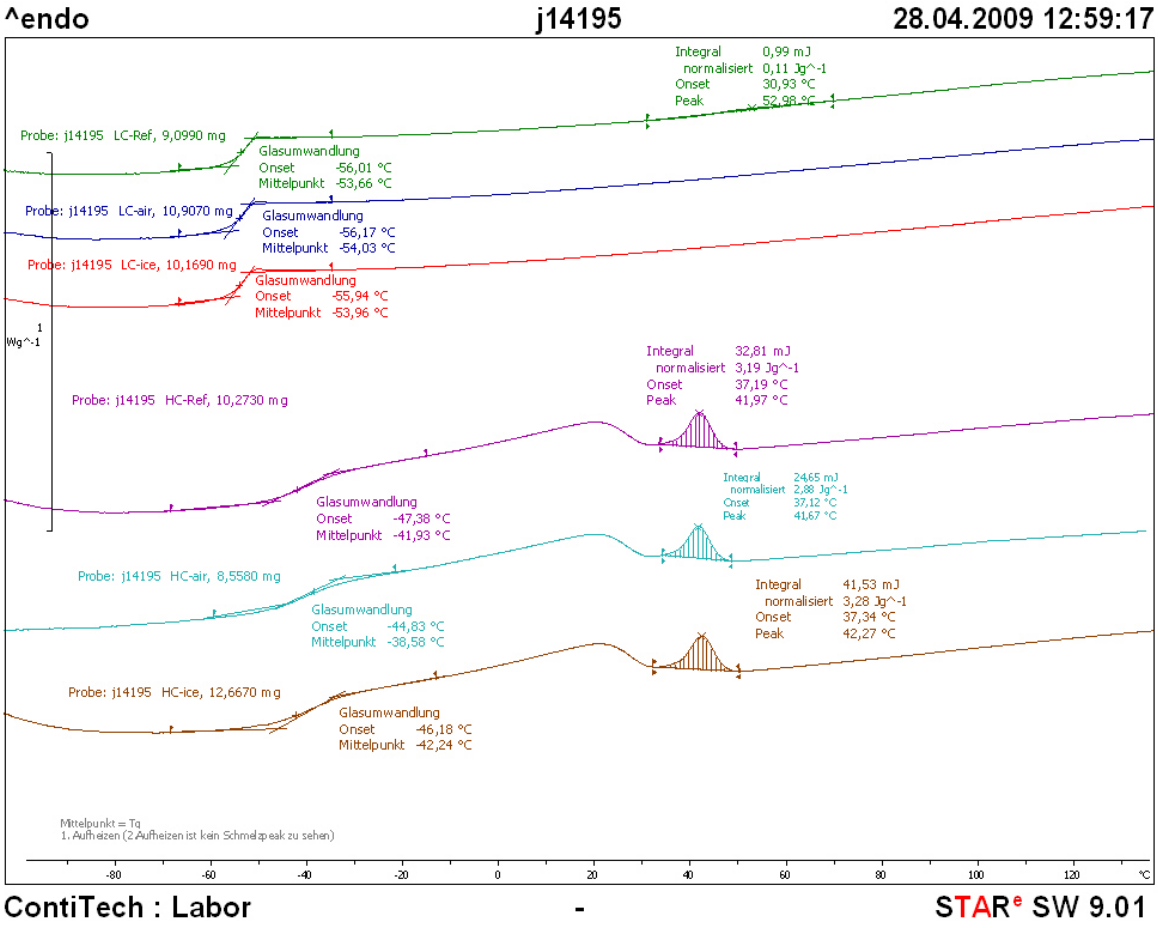

Figure 7.3: *DSC analysis on amorphous and semicystalline filled EPDM elastomers. Contrary to the amorphous material the semicrystalline elastomer shows a melting energy at approximately 45°C corresponding to the melting of the crystallites.*

DSC performed in the range of -100°C – 140°C shows the presence of the crystalline structures in the sample (Fig 7.3 the lower 3 curves). As a reference material, an amorphous sample was subjected to the similar experimental procedures followed by a DSC investigation. No hints of crystalline fractions could be observed (Fig. 7.3 upper 3 curves). In case of the crystalline material no significant differences between the cooling rated could be observed. A reason for that could be that the amounts of crystallites remain similar after the heating-cooling procedure, differing just in size.

The standard physical tests reveal no difference between the two materials. The stress-strain test stretches the sample up to 300 % elongations. Therefore the method could not be sensitive enough to detect heterogeneities at nanoscale domains. DMA could be a more suitable tool to investigate such inhomogeneities. Using a frequency of 1 Hz and very small shear amplitudes, DMA is a much more sensitive device to detect the above mentioned changes in submicron scales.

DMA measurements were performed on each of the sample, to determine the macroscopic shear modulus. In a first approximation the E-modulus is calculated using the DMA measured values with:

$$E = 2G(1 + \vartheta), \tag{7.1}$$

Where E is the Young modulus, G is the shear modulus measured with DMA and ϑ is the Poisson's ratio of the material. For filled elastomers the Poisson ratio can be approximated to a value of 0.5. Therefore the Young's modulus is calculated to be three times higher than the shear modulus.

DMA measurements show a slight difference between sample B and sample C (Table 7.2). The slow cooled sample (C) show a higher modulus compared to the fast cooled one (B). The

increase in modulus can be attributed to the build-up of a higher heterogeneous structure in the slow cooled sample compared to the fast cooled one.

Table 7.2: *E-modulus of the annealed samples.*

	DMA[1] [MPa]	AFM[2] [MPa]
B	13,7	47
C	15,2	67

[1] *E-modulus calculated from the shear modulus of the DMA experiment using Eq.1.*

[2] *Modulus calculated from the average force distance curve of an AFM experiment.*

AFM tapping mode imaging reveal differences in heterogeneities between the two samples (Fig. 7.3). The surface of slow cooled sample (Fig. 7.3d) shows bigger structures compared to the fast cooled one (Fig. 7.3b), as observed in the amplitude pictures. A very fine dispersion with small structures can be observed in the fast cooled sample (Fig. 7.3a, 7.3b).

Comparing both the phase image and the amplitude image, one can observe that the structures can come either from the filler agglomerates, or from the crystallites. To make sure that in case of the slow cooled sample the heterogeneities are formed due the build-up of the crystalline structures, further AFM nanoindentation was used for characterization.

Analyzing the surface of the slow cooled sample (Fig. 7.3c, 7.3d) three regions of interest can be distinguished. Single force-distance curves were extracted from the three different regions (Fig. 7.4). The soft region represented by the red curve, which belongs to the polymer matrix, is characterized by a high indentation (soft material), and a high adhesion. The extracted values from the force curves are presented in Table 7.3. Second region is characterized by a very stiff surface, with very low adhesion and low maximum indentation of the tip of the

cantilever into the sample. These types of properties are attributed to filler agglomerates near the surface of the sample. The force curve performed on the third region of interest returns us properties in middle between the two other regions (polymer and filler). This region could be attributed to filler particles coated with a larger polymer layer or to the crystallites.

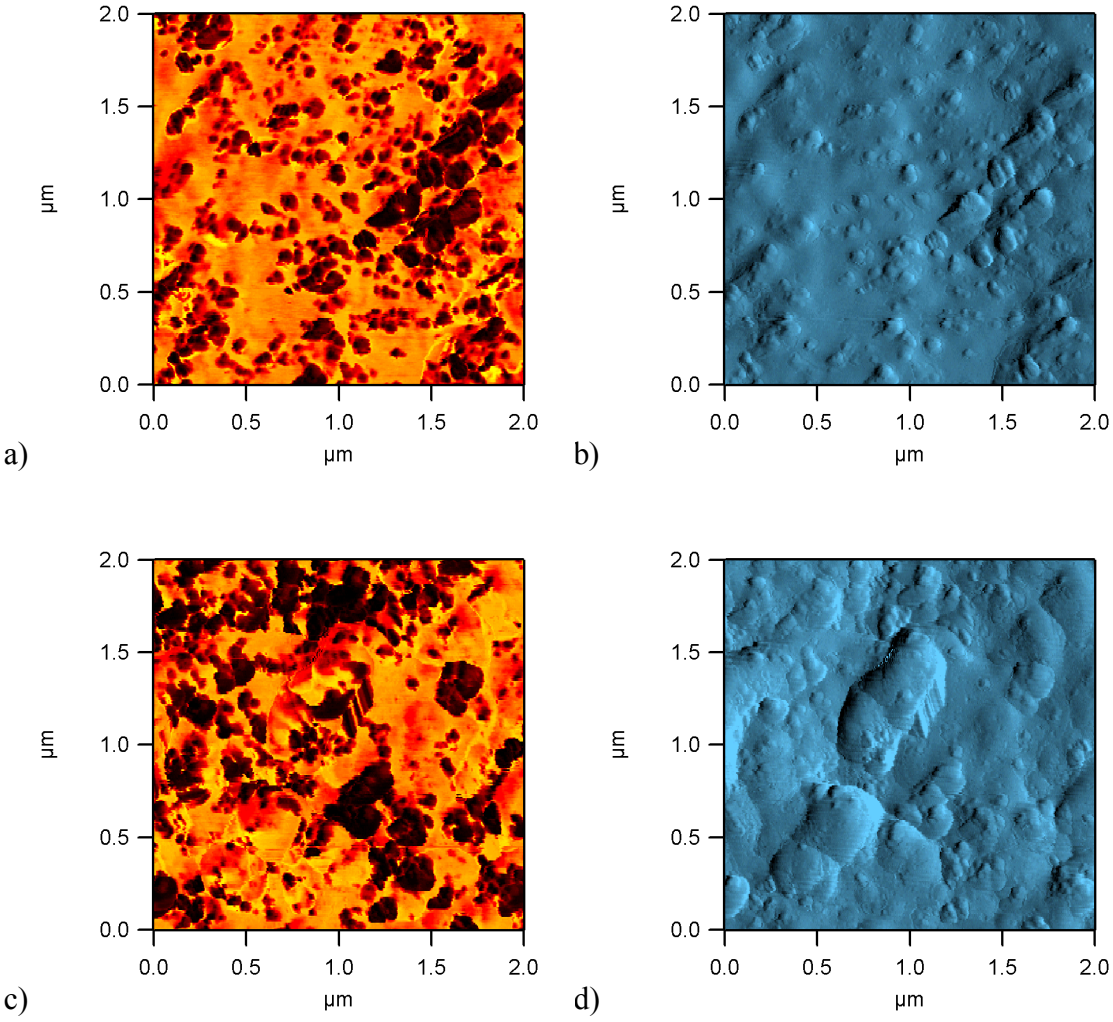

Figure 7.3: *2µm AFM images. From up to down: Fast cooled sample (B), Slow cooled sample (C). From left to right: Phase contrast image, Amplitude image.*

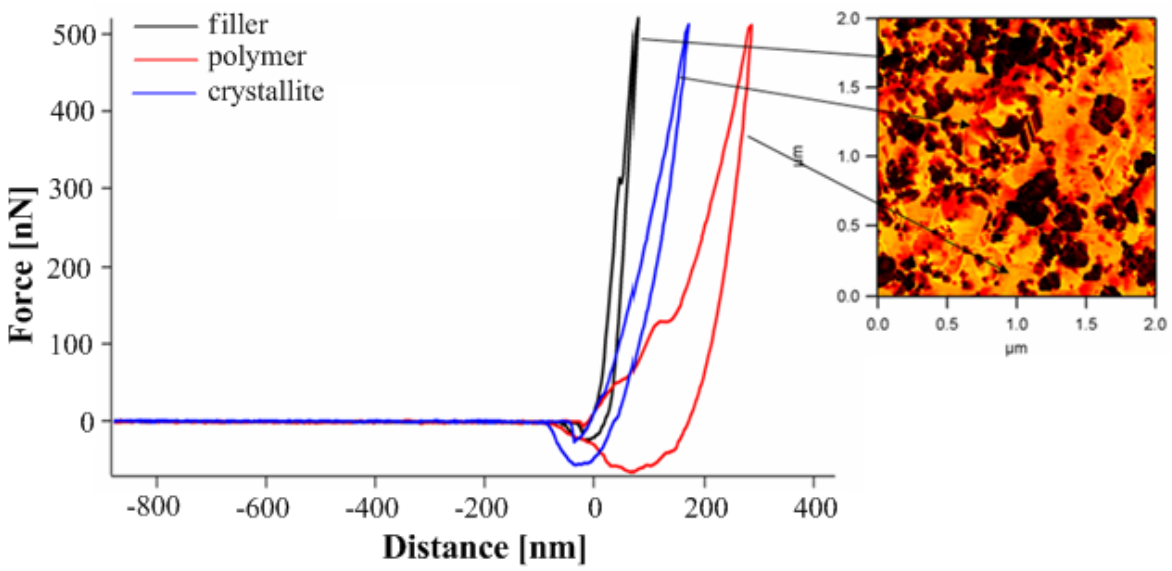

Figure 7.4: *Force-Distance curves recorded from: Red – polymer matrix, Black – filler particle and Blue – Crystallite.*

The data in Table 7.3 shows that among the soft polymer regions characterized by high adhesion and high indentation, and the filler agglomerates with stiff behaviour and low adhesion, a third region of interest is noted. It is characterized as a region with intermediate properties between the above mentioned 2 regions.

Table 7.3: *Micromechanical properties extracted form Force-Distance curves*

	MaxIndent [m]	ElastWork [J]	PlastWork [J]	Adhesion [J]	LossRatio
Polymer	3.36E-07	2.88E-14	3.65E-14	11.9E-15	1.27E+00
Crystallite	1.73E-07	2.16E-14	1.44E-14	3.70E-15	6.60E-01
Filler	0.83E-07	1.19E-14	0.77E-14	1.20E-15	6.40E-01

Force mapping experiments were further performed to characterize the micromechanical properties of the investigated samples. An area of interest with a square shape with the length of 2 µm was chosen. 60 x 60 force curves, equally displaced in the 2 µm length were extracted from this square. The set point for the maximum indentation force was set to 500 nN.

Applying the E-modulus calculation based on Oliver and Phar [45, 59] description and adapted by the author [71], plots of heterogeneity in terms of E-modulus can be drawn (Fig. 7.5). Regions with high values of e-modulus can be observed. These regions are attributed to the filler-filler network, polymer-filler interactions, as well as the build-up of the crystalline structure.

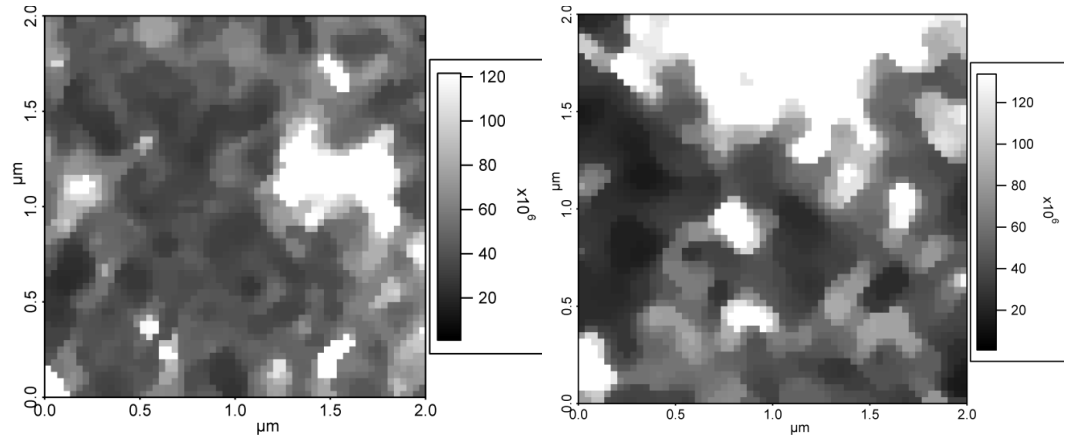

Figure 7.5: Plots *of E-modulus calculated after the O&P method. Left sample B, right sample C*

Comparing the two different samples (B and C) one can see that the heterogeneity in sample C is much higher. For a better observation histograms from the E-modulus plots were extracted for both mappings (Fig.6). The observed broad range and extremely high moduli are in good accordance to the work of Nishi [82]

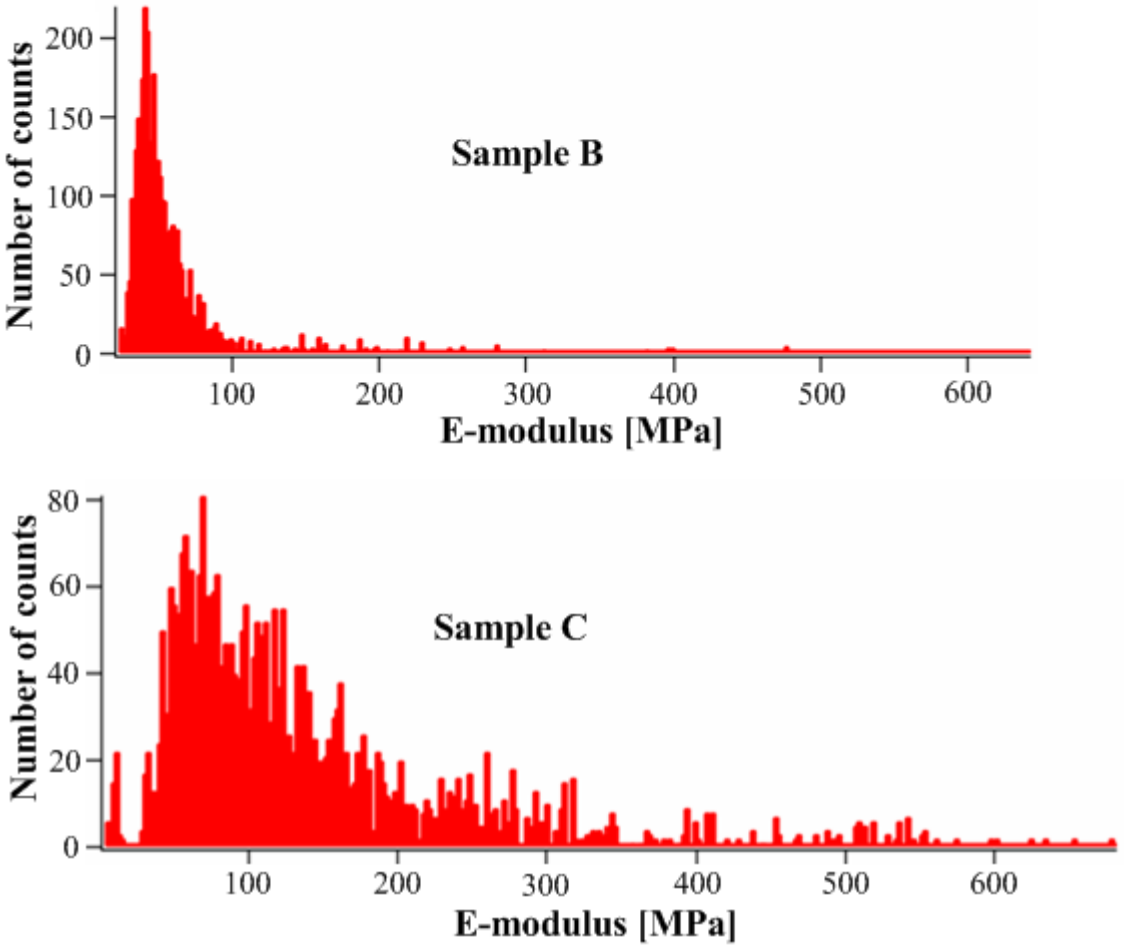

Figure 7.6: *Histograms of E-Moduli drawn according to Fig 7.5. Up sample B, down, sample C. The horizontal axis shows the distribution of the modulus, while the vertical axis describes the number of moduli.*

As can be observed, the calculated values for the average modulus from the AFM force mapping experiment are higher compared to the calculated value from the DMA shear experiment (Table 7.2). It has been shown that using higher forces for the set-point leads to a systematically deviation of the microscopic moduli compared to the macroscopic ones [71]. Moreover by extrapolating the modulus to zero forces, by performing a force-variation experiment, one could obtain values that fit to the macroscopic ones [71]. The explanation for

these results comes from the Hertz theory principle [83], which is accurate only for small amplitudes, in our case for small forces used as set point. Therefore approaching to zero indentation in our experiments, comparable results with the macroscopic values could be obtained. However higher forces were used, due to the increase of the surface effects with decreasing the maximum indentation.

The macroscopic modulus is determined by the large soft areas in the polymer matrix [71, 82]. Performing a force variation experiment on a soft region (polymer), and extrapolating to zero force, values comparable to the macroscopic ones are obtained [71]. On the other hand the occurrence of the extremely high local moduli can be explained by a different dependency of the measured modulus with increasing the amplitude.

A force variation experiment was performed on the samples (B and C). The set-point forces were varied between 100 nN and 500 nN force. The average force curves were calculated and the moduli obtained from these curves were plotted against the set-point force (Fig. 7.7). The average force curves were chosen to include also the properties of stiff areas from the mapping experiment. Figure 7.7 shows different slopes for the different cooled materials. In the case of the slow cooled sample, the modulus increase is much faster related to the set point force. It can be explained by the different heterogeneities of the materials. At 500 nN set-point sample C shows a higher modulus with about 50% compared to B. Despite these differences, by extrapolation to zero force, the macroscopic moduli, which differ only with 2 MPa between the two samples (Table 7.4), are obtained.

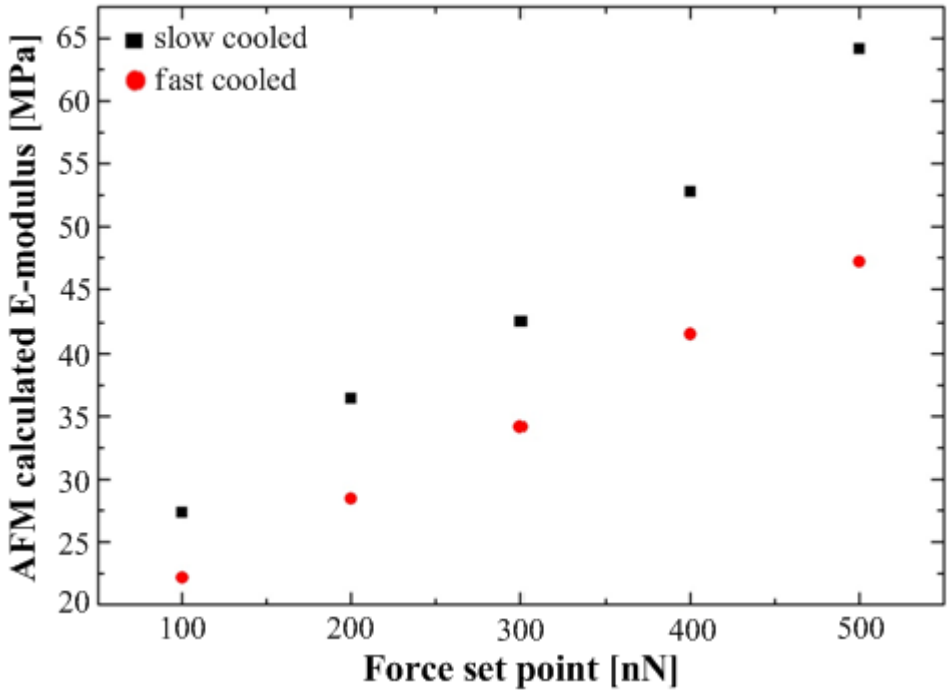

Figure 7.7: *Plots of calculated E-Modulus using nanoindentation versus the set point force.*

Therefore we show that in the case of microscopic determination of the moduli, using nanoindentation, it is not necessary to choose the soft areas for comparisons with the macroscopic modulus. The average force curve, which includes also information regarding the stiff areas, can be successfully used as well.

Table 7.4: *Values of E-Modulus measured with DMA, and calculated by AFM upon extrapolation to zero force.*

	DMA [MPa]	Extrapolated AFM [MPa]
B	13,74	15,76
C	15,21	17,32

7.4 Conclusions

It is of a critical importance to locate heterogeneities at the nanoscale to accurately be able to predict the behavior of the bulk material. This is even more important when the macroscopic characterizations show no significant hints. In this direction AFM proved to be a very powerful tool for surface characterization at micro scales in terms of topography, material phase contrast and micromechanical properties.

Different cooling rates lead to modification of the structures observable only at micron and submicron scales. In terms of micromechanical behavior AFM proved to be an adequate tool being able to distinguish between 3 phases from a polymer mixture: high stiffness (filler particle) very low stiffness (polymer), and intermediate stiffness (crystallite) Fig. 7.4. The heterogeneous build up is higher in the slow cooled material (Fig 7.3c), which leads to inhomogeneities in the material. The fast cooled shows a higher homogeneity (Fig. 7.3a).

It has been previously showed that the macroscopic modulus is determined by the soft regions from a polymer matrix. Therefore it has been speculated the microscopic modulus should be determined in the soft areas of the polymer materials in order to get comparable results to the macroscopic ones. This work shows that the stiff areas represented by the filler agglomerates can also be included in the modulus calculation trough an average curve. Doing so, the modulus obtained trough extrapolation is calculated to be similar to the macroscopic values.

Doing a force variation experiment on the two different samples, an increase of the modulus is observed with the increase of the force. However due to the formed heterogeneities in the slow cooled sample, the increase is faster compared to the fast cooled sample.

8. Formation of barrier materials using oriented organoclays in SBR/BR mixtures reinforced with in-situ silica, obtained by sol-gel process

Using a mixture of oriented organoclay and SBR/BR polymer, subjected to a sol-gel process in TEOS, a new "barrier material" was created. Due to the organoclay orientation, which is perpendicular to the swelling direction the silica particles agglomerates at the edge of the material, up to a depth of 0.4 mm. A new material is obtained, having great interfacial properties (high reinforcement at the contact with the medium), and medium reinforcement in the centre of the material. An unfilled material was used as reference. The resulted material was examined using a profile NMR Mouse, to compare the relaxation times of the material between the centre and the edge. Atomic Force Microscope (AFM) was used to investigate the micromechanical properties, between the two regions of interest.

8.1 Introduction

In recent years, the development of new composite materials to fulfil the increasing demand for high performance products has been a topic of interest for both academic and industrial research. In the domain of high performance materials, composite materials resulting from the combination of polymers and fillers play a major role. Indeed, these hybrid materials combine advantageously the properties of both components: for example increased stiffness with respect to the pure polymer, but reduced fragility when compared to the inorganic pure material. A careful selection of the components leads to high performance

materials with improved mechanical properties, increased heat distortion temperatures and improved flame resistance or oxygen permeability.

Contrary to soot, carbon black represents a microscaled filler material prepared from gas and oil in a special combination process. Therefore different types are available. Depending on the geometrical structure, the surface activity and the specific surface area, rubber materials with different macroscopic and microscopic properties can be prepared.

A second important class of fillers - named silica – is based on SiO_2. The main synthetic routes for the preparation of these microscaled filler are based on the precipitation (precipitated silica) and combustion of silica (pyrogenic or fumed silica).

The incorporation into the polymer of all these conventional fillers occurs during the mixing process on the two roll mills or internal mixers. Due to the high viscosity of rubbery polymers, during the mixing process the microscaled filler particles can be dissipated into nanoscaled dimensions. Having nanoscale dispersion is a precondition to achieve high performance rubber materials.

The sol-gel process is considered a new technique on the laboratory scale for silica incorporation into rubbers [84, 85]. The generation of in-situ sol-gel derived silica nanoparticles is a promising route for proper dispersion of filler in the polymer matrix [84-90]. The procedure consists of swelling a rubber piece in tetraethyl orthosilicate (TEOS), and then subjecting the TEOS-swollen rubber to a sol-gel process i.e. hydrolysis and condensation reaction [84, 91, 92]. Upon the hydrolysis and condensation reactions, the TEOS contained in the rubber is converted into silica according to:

$$Si(OC_2H_5)_4 + 2H_2O \rightarrow SiO_2 + 4C_2H_5OH \quad (8.1)$$

Ideally, 2 moles of water are required to convert one mole of TEOS into anhydrous silica. Thus, due to the formation of silica particles, the TEOS-swollen rubber is converted into a silica-reinforced composite [92].

Moreover if we think at materials such as hoses, pipes, even tires, which require special coatings and extra reinforcement at the contact interface, standard reinforcement with carbon black may become very problematic. Hence, the development of new gradient materials with barrier properties in these fields is of great importance in this research field. The advantage of these materials is that the diffusion of the fluids/media, for example in hoses, is significantly reduced, conferring thus higher stability for the material.

However, few reports have been published regarding the formation of new materials with barrier effects. Ikeda [93] has studied graded vulcanizates obtained by heat pressing together 3 layers of rubbers with different chain densities, and additionally reinforcing the materials with in situ silica generation. The expected results were an increase in elastic modulus by tensile experiments due to in situ experiments. No hints regarding a barrier formation or changes in material properties with respect to depth were mentioned. Yoshikai et al [91] have shown that there is a big influence in the silica formation related to the amount of TEOS used. The H_2O/TEOS ratio was varied to control the diameter of the silica particle. Other reports mentioned an increase in mechanical properties after in situ silica formation [94-96]. Das et al [97] have presented a further improvement in the sol-gel method of reinforcing with silica, by adding TESPT (3-triethoxysilypropil tetrasulphane) to the raw mixture. A significant increase in reinforcing efficiency was noticed when using TESPT compared with the mixtures without TESPT.

An alternative route for obtaining barrier materials is the incorporation of platelets as filler materials like organoclays. During the mixing due to high shear forces the clay platelets

exfoliate. Calendaring leads to an orientation of the platelets along the calendaring direction (Fig. 8.1).

Due to the preparation procedures the sample swells largely perpendicular to the nanoclay orientation. For the aim of obtaining the desired "barrier" materials, perfect parallel oriented nanoclays would be the ideal case. To achieve the requirements of different materials several layers are laminated in the products. In hoses for example several layers are employed: an inner layer, which consists of a material with low permeability, and an outer layer or a cover consisting of high permeability material and a high filler load. In such laminated products a sharp geometrical interface, smaller than 0.01 mm is formed between the layers. In the swelling process of the in-situ silica formation a gradient in the filler distribution will be formed. Therefore it could be an advantage in order to avoid the interface caused by the lamination processes.

The aim of this experiment is to develop a new route for creating so called "barrier" materials. This goal can be obtained by mixing of organoclay together with the polymer before the sol-gel process. The term "organoclay" refers to a class of materials generally made up of modified layered silicates that are similar to mica. While these clay particles can span centimetres in lateral dimensions, the in-plane dimensions of the individual clay layers are on the order of a micron, and the thickness of a single clay nanoplatelet is on the order of a nanometres. Due to their shape they can easily be oriented during the preparation process. The orientation can be achieved if paying special attention on the calendaring process.

During the sol-gel process, the silica particles are formed in the rubber matrix. The formation of the silica particles can be understood by following the principle of "first come, first settled". This rule, cumulated with the perpendicular orientation of the organoclay filler

compared to the relative direction of the silica formation, leads to formations of blockades, and thus, a higher concentration of silica at the surface of the material.

An improvement in mechanical properties is expected due to reinforcement with in situ silica. As explained above, a heterogeneous dispersion of the created silica particles is expected to occur due to the organoclay fillers added to the mixture. AFM and NMR techniques can be used to investigate this improvement in mechanical properties and the barrier formation, and to correlate the observable parameters.

8.2 Experimental Part

Materials

For the following investigations, 50:50 by weight mixture of SSBR (Solution Styrene Butadiene Rubber) and BR (Butadiene Rubber) rubbers was used. The investigated material was reinforced with 5.5 phr modified organoclay. A non-filled sample was also characterized for comparison. These formulations are summarized in Table 1. Both chemicals used in the experiment, TEOS and Butylamine, were purchased from MERK, Darmstadt, Germany. All reagents were used as received.

Sample Preparation

The mixtures were prepared in a POLYMIX 110 L mixer from Servitec in two steps. In the first step, the polymers together with the organoclay were mixed at 80^{o} C. In the second step the additives (Table 1) were added and mixed together at 40^{o} C. Vulcanization was performed at 160^{o} C. The crosslinking reagent was sulphur. Stearic acid and ZnO were used as accelerators. The resulted rubber sheets (filled and unfilled) were immersed in TEOS for 48

hours. After swelling, the samples were soaked in a 10% Butylamine solution for 72 hours, to obtain silica particles by the condensation reaction of TEOS. After this process, the final compounds were dried 4 hours in vacuum at 50° C [97, 98].

Table 8.1: *Sample composition (in phr)*

Composition	unfilled	filled
SSBR	50	50
BR	50	50
ZnO	2.5	2.5
Stearic Acid	2.5	2.5
Organoclay	-	5.5
Aromatic oil	9	9
DPG	2	2
CBS	1.7	1.7
Sulfur (soluble fine)	1.4	1.4

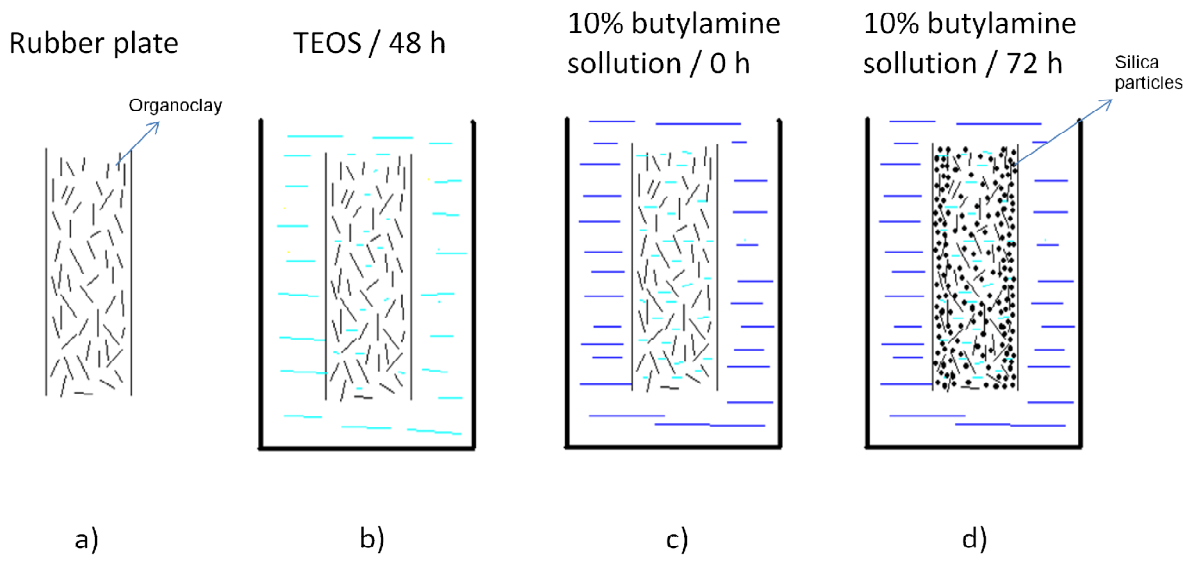

Figure 8.1: *Schematic illustration of the experimental setup. a) After calendaring, the filler is expected to gain an orientation slightly parallel to the calendaring direction. b) Swelling in TEOS for 48 hours. c) Sample immersed in 10% Butylamine solution. d) Silica formation due*

to sol-gel process. The nanoclay orientation is expected to lead to the formation of a "barrier" in the material.

Characterization methods

Standard physical tests were performed on the samples to observe the effects of reinforcing, changes in tensile strength and elongation at break. As first step, the optical microscope was used to characterize cross section sample inhomogeneities. A gradient or a barrier was observed, as expected in the optical examinations.

A special single-sided sensor with an improved magnetic field profile, the Profile NMR-MOUSE® [99-104], was used. High resolution ^{1}H NMR depth profiles have been obtained from the measured swollen and not swollen samples. An NMR observable related to the sum of the spin echoes in the Carr-Purcell-Meiboom-Gill pulse sequence was used to characterize changes produced by the action of the swelling procedure. To characterize the behaviour of the elastomers after swelling, a set-up consisting of the NMR-MOUSE®, able to produce displacements on the Z axis using a precision lift was employed. The NMR-MOUSE® has a flat sensitive volume at a fixed distance of 5 mm above its surface. The object is positioned on top of the lift that contains the NMR-MOUSE® (Fig. 8.2a) [105]. The lift changes the distance between the NMR-MOUSE® and the object with a precision of at least 10 μm: the sample can then be scanned to acquire ^{1}H-NMR parameters as function of depth into the object (Fig. 8.2b). In the work reported below, depth profiles were measured in increments of 30 μm at a resonance frequency of 18.1 MHz in uniform field gradient of 22.3 T/m.

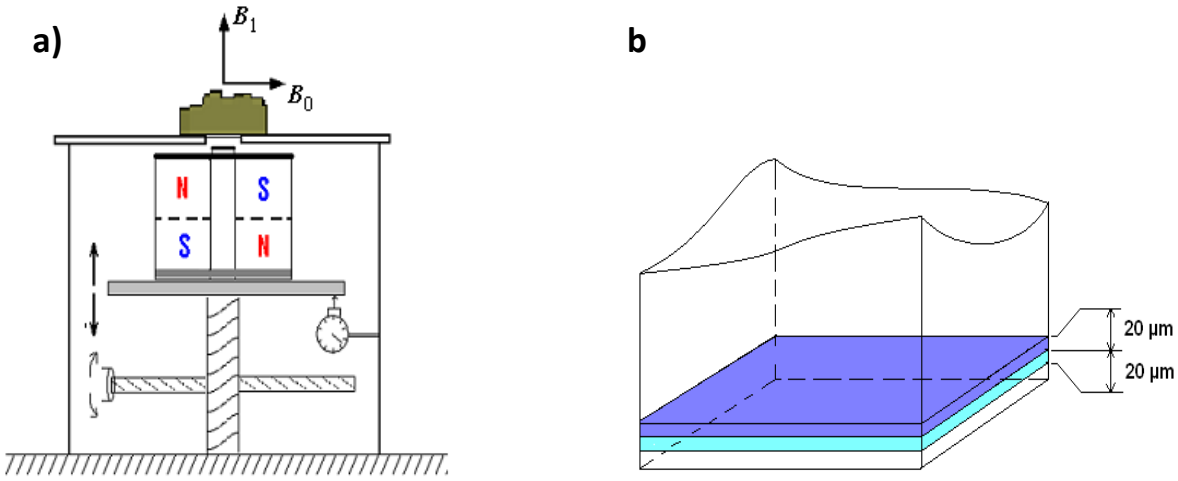

Figure 8.2. *(a) Experimental setup for the measurement of microscopic profiles across the samples. The Profile NMR-MOUSE is mounted on a high precision lift by which the distance between the NMR-MOUSE and the object on top of the lift can be changed with micrometer resolution. (b) Schematic representation of a section of the object and the sensitive volume at two positions [105].*

Usually, AFM is used to image surface properties and material distributions through phase difference and topography. Furthermore the AFM was used as a micro indenter. The plot of the tip deflection signal versus the vertical motion of the piezo actuator, named force curve, contains information regarding local properties (at the nanometric level) of the materials such as elasticity, plasticity, stiffness and adhesion. Force distance plots were used to characterize the micromechanical behaviour of un-swollen and swollen materials.

8.3 Results and discussions

An unfilled and a filled material were prepared according to the recipes shown in Table 8.1, curing the mixtures using sulphur at 160°C [97]. The resulted 2 mm thickness

sheets were then subjected to the sol-gel process. Same conditions were applied to both samples, filled and unfilled.

Table 8.2 shows the results from the mechanical tests. Due to a low amount of layered silicate added to the mixture (5.5 phr), the differences between the filled and the unfilled materials (both unswollen) at low strains are small. Significant differences are observed at higher strains (>200% elongation).

Table 8.2: *Mechanical data*

Sample		σ(100%) MPa	σ(200%) MPa	σ(300%) MPa	σMax MPa	εB %
Unfilled	**Unswollen**	0.79	1.14	-	1.26	239,1
	In-situ	1.25	1.66	2	2	298,36
Filled	**Unswollen**	0.81	1.13	1.4	1.65	389,32
	In-situ	1.83	2.78	3.74	4.22	351,54

The results of the in situ process show a significant reinforcement. The build-up of silica particles into the polymer matrix was successful, and as expected, the increase in E-modulus after swelling in TEOS is clearly visible. Tensile strength of the swollen filled material shows an increase of about 200 %. Even for the unfilled material, reinforcement of about 50 percent is noticed. The elongation at break of the filled swollen sample is slightly decreased after the swelling process.

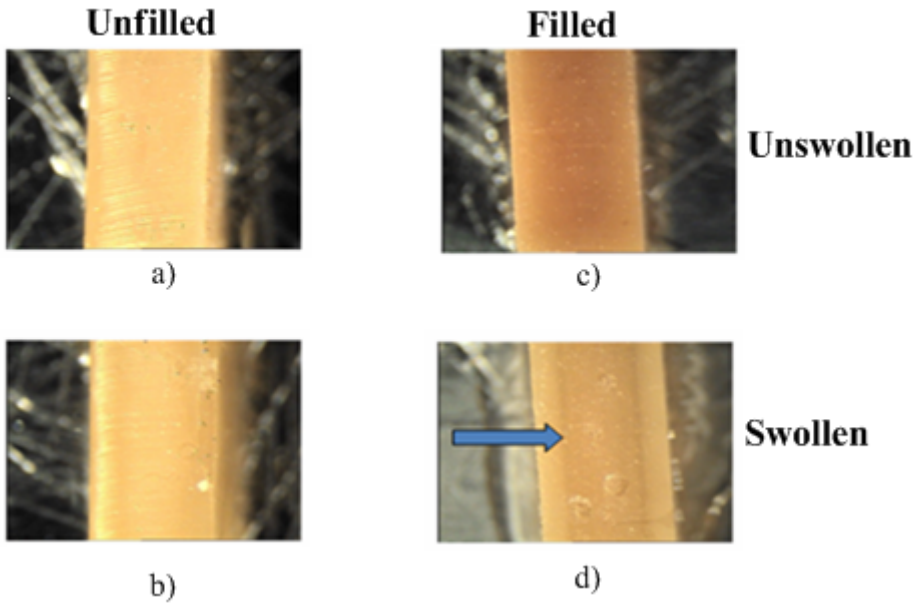

Figure 8.3: *Optical microscopy images taken on cross-section of each material. a) Unfilled and unswollen material. b) Swollen and unfilled; c) Filled and unswollen; d) A coloured gradient can be observed in the filled and swollen sample.*

Optical microscopy images were taken from cross-sections of the investigated materials (Fig. 8.3). The unfilled material shows no difference after the swelling process. However, for the filled material, a "colour gradient" is observed in the cross section. Taking a closer look we can argue that a "barrier" is formed inside the material up to a depth of 0.4 mm. As represented in Fig. 8.1, the relative orientation of the organoclay platelets becomes perpendicular to the swelling direction. The growth of silica particles into the material takes place in several steps. The first step consists of a homogeneous dispersion of the in-situ generated fillers into the polymer matrix. After certain saturation, the generated particles, together with the oriented organoclay, will fill up the spaces between the polymer chains, and thus drastically reduce the mobility. In the second step, the silica particles grow further, but, due to reduced gaps between the polymer chains, the formation takes place largely at the edge of the material, thus creating a so-called "barrier", and only in small amount in the centre. In

the third step, the silica particles are formed only at the edge of the material, and fill the remaining gaps in the material. The growth mechanism creates a heterogeneous material, with two zones of interest, edge and centre. The edge area consists of a high concentration of silica formed fillers, with highly homogeneous dispersion, while the centre of the material contains lower concentration of fillers.

A strong filler-filler and polymer-filler interaction is expected at the edge of the material. Relating the filler-filler and polymer-filler interactions to NMR terms, one can say that with an increase of these interactions, the overall polymer chain mobility is reduced, and thus, the material is expected to show a shorter NMR T_2 relaxation time. To probe this, NMR relaxation measurements were performed, with the Profile NMR MOUSE. The relaxation time was measured as a function of depth. Profiles were acquired with a resolution of 30 μm. (Fig. 8.4). The experimental data was smoothed with an adjacent average function provided by Microcal Origin software.

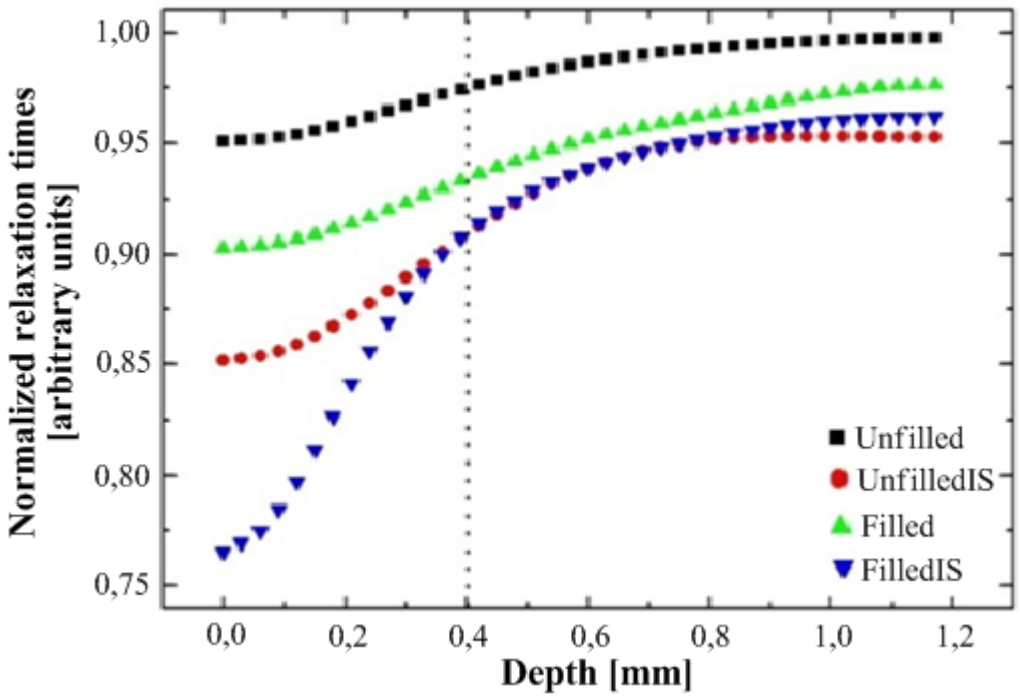

Figure 8.4: *Depth profiles acquired with the NMR MOUSE. The graph plots the normalized relaxation time with respect to the depth of the sample.*

The data shows the impact of the swelling process and silica formation on the overall chain mobility. As expected, the swollen samples show a reduced mobility compared to the untreated ones. A reduced mobility is also observed for the filled material compared to the unfilled one. This is due to the polymer-filler interaction, which occurs with the incorporation of organoclay in the matrix. Interestingly, the results measured for the swollen and filled sample revealed a strong gradient as function to depth. This gradient shows a reduced mobility at the edge of the material compared to the unfilled and swollen sample. This difference in terms of chain mobility between the two is present until a depth of about 0.4 mm. These results are consistent with the optical microscopy pictures where this gradient can also be seen (Fig. 8.3). In this case, a difference in contrast between the centre of the sample and the edge can be observed, indicating a heterogeneous reinforcement with in-situ silica.

Due to the barrier created by the oriented organoclays in the filled material, less silica is formed in the middle of the sample. This assumption is supported by the slightly higher mobility in the centre, compared to the unfilled material, where the dispersion of the in-situ silica is expected to have a higher homogeneity across the material.

AFM imaging was further used to investigate the heterogeneities of the samples. Four AFM AC images were acquired across the sample starting with several microns distance to the surface (Fig. 8.5a) towards the middle of the sample (Fig 8.5d), with a distance of approximately 200 µm between them. The experimental set-up excludes the possibility of a measurement artefact caused by the tip erosion and therefore an increase in the particle size, since the order of the measurements is from a) (first) to d) (last).

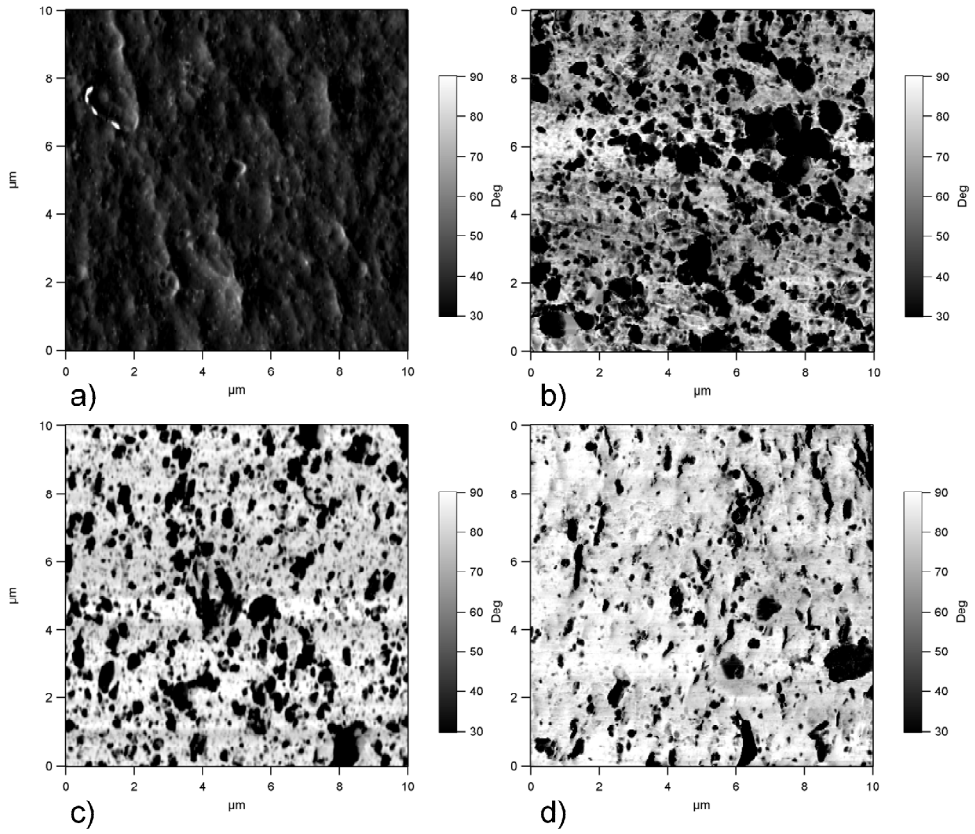

Figure 8.5. *AFM phase contrast images taken from the cross-section of the filled-IS material. A) Phase contrast of the material several microns under the surface. b) to d) Phase contrast of the sample as a function of depth, with increments of 200 µm.*

Figure 8.6a shows the phase contrast image scanned at the surface of the sample. The lower phase shift compared to that of the other positions shows reduced energy dissipation, which is a hint for higher stiffness. This can be explained by the existence of so many particles, which are covered with polymer, that they cannot be differentiated. As explained above, the in situ silica was precipitated extensively at the edge of material, filling up all available space. Due to polymer-filler interactions, silica particles are covered with a layer of polymer, which confers to the material a high grade of homogeneity. In Fig. 8.5b, the phase contrast measured at a 200 µm distance from the edge of the sample is shown. A heterogeneous dispersion can be observed. Silica growth takes place here until the spaces between the polymers chains at the surface of the material are completely filled due to the sol-gel process. As one measures deeper in the sample, the silica concentration decreases, supporting thus the theory suggested above.

As a further step in the investigation of the barrier formation at the edge of the sample, AFM was used to analyze the micromechanical properties, which can be extracted from force volume experiments. A force volume experiment or a force mapping consists of a collection of force-distance curves performed at equal distance one of each other over a pre-specified range as described in chapter 2.1.5.

Force mapping experiments were performed for both filled and unfilled samples. The swollen samples were scanned at the edges and in the centre of the material. The mean values of the maximum indentation were calculated and plotted in Fig. 8.6, for the filled materials, and in Fig. 8.7 for the unfilled materials.

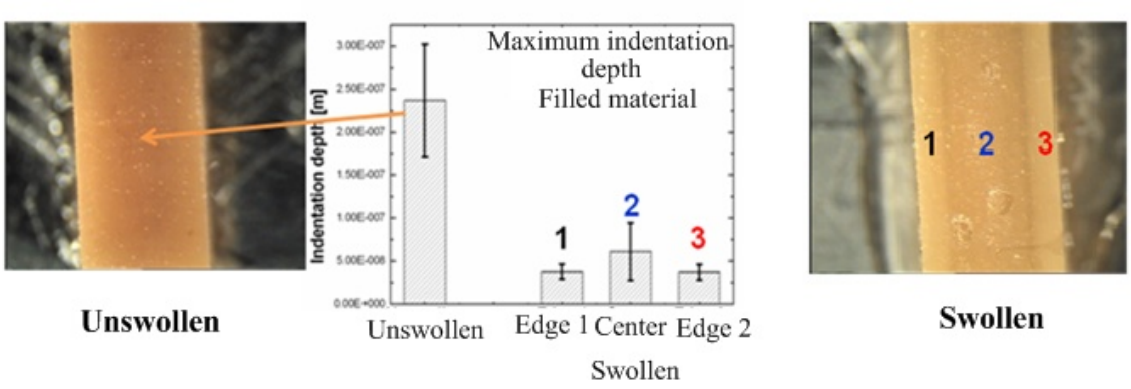

Figure 8.6: *Representation of mean values for maximum indentation acquired from force mapping experiments on the filled sample (unswollen and swollen).*

The maximum indentation is the calculated value from the force distance curve. It depends on several factors such as the experimental parameters, the tip shape and the sample stiffness. Having the first two factors constant, we argue that the maximum indentation is a measured value representative for the "hardness" of the material: the lower the indentation, the harder the material. The "error" bars in the graph show the standard deviation of the values from the force mapping experiments related to the mean value. They are not actually an error, but an indication of the heterogeneity of the material.

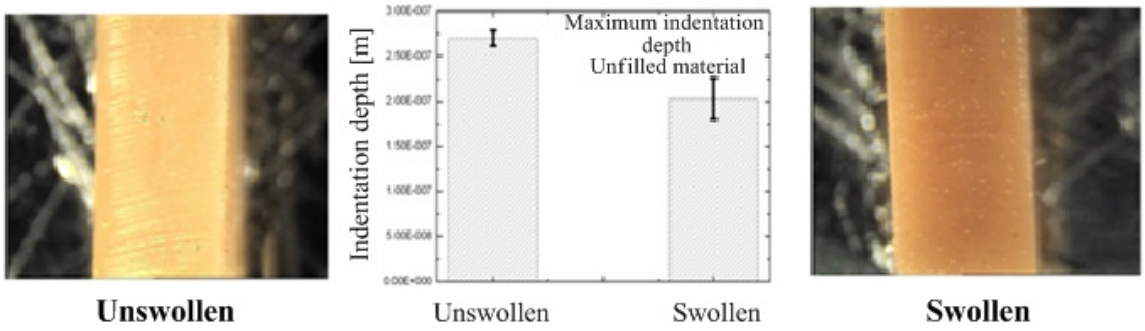

Figure 8.7: *Representation of the mean values for maximum indentation acquired from force mapping experiments of the unfilled sample (unswollen and swollen).*

As shown in Fig. 8.8 several force curves were extracted from the force mapping experiments performed on the filled materials, swollen and unswollen. The curves where chosen from the two areas of interest: the polymer surface (solid line) and the filler surface (dotted line). In case of the unswollen materials, a high indentation depth is observable compared to the swollen ones. Even when indenting on the filler surface of the unswollen the returned indentation is higher compared to swollen samples. This is attributed to the low concentration of the filler in the polymer network which allow to a denser polymer-filler interactions rather than filler-filler interaction. The filler particle is covered with a polymer layer which is further surrounded by polymer chains. Therefore an indentation on such particles returns higher values, since it not only indents the filler particle, but it also displaces the filler particle into the polymer matrix. Another hint for that is the adhesion peak that can be observed under the base line in case of the indentation on the filler for the unswollen material. The peak can be attributed to the polymer layer on the filler surface. This peak disappears in case of the swollen samples (IS). In case of the IS samples a much stiffer behaviour is observed. The indentation on the filler particles returns force curves similar to the ones performed on glass. Even on the polymer regions of the IS samples, although we have a higher indentation, the surface is very stiff, which gives us a hint regarding the structures under the polymer surface. These curves support the theory described earlier, that a strong reinforcement is obtained at the edge of the material. Nevertheless after the in situ process a significant increase of the reinforcement in the centre of the material was also obtained.

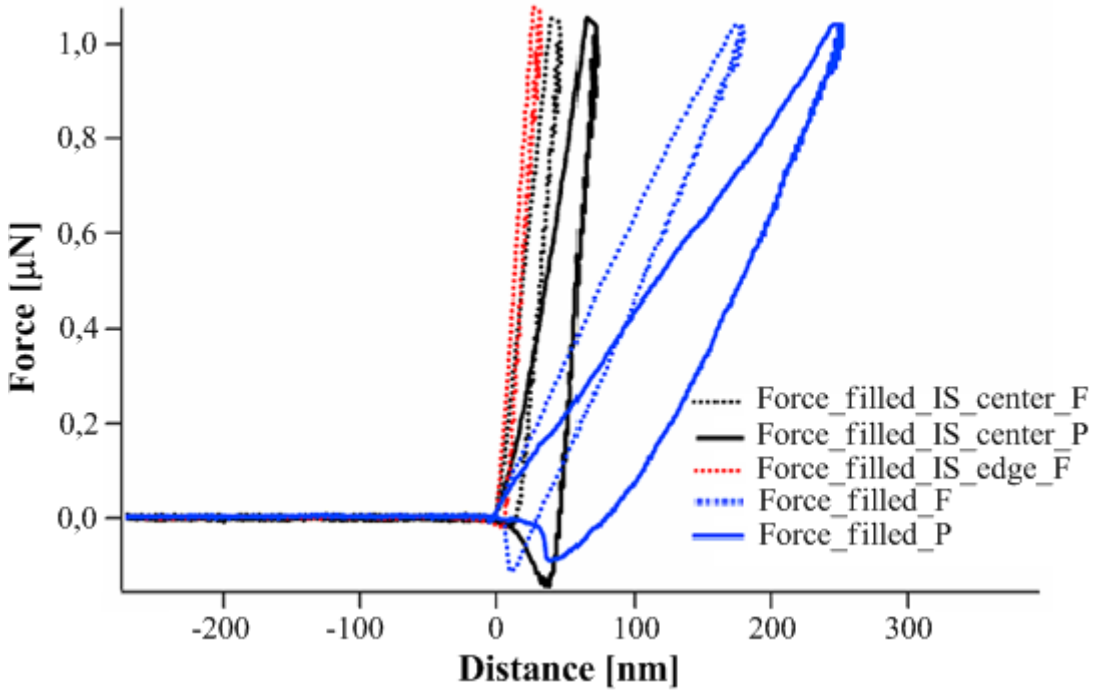

Figure 8.8: *Representative force curves extracted from the force-mapping experiments performed on the filled materials (swollen-IS and unswollen); letters F and P, from the legend represent the location where the force curve was taken: F on top of a filler particle, and P, above a polymer region.*

The force mapping experiments show good correlation with the physical data, and the NMR profile scans. The increase in E-modulus observed by physical tests can be correlated with the increase in maximum indentation observed by the force mapping experiments. The NMR signal versus depth plots revealed that there is a decrease in chain mobility at the edge of the material compared to the centre. The force mappings performed at the edge and in the centre of the material, show a difference in hardness too. At the edge, the sample is stiffer compared to the centre (Fig. 8.6). The decrease of the NMR values measured at the edge of the sample indicates lower chain mobility, which can be associated with a more rigid material (Fig. 8.4). A rigid material compared to a softer one shows lower maximum indentation. Here we can

conclude that the lower the mobility of the chains measured with the Profile NMR-MOUSE is, the lower is the maximum indentation calculated from the force mapping experiments.

8.4 Conclusions

Incorporation of the organoclay fillers in the rubber matrix can be a viable way to create so called “barrier materials”. A condition which has to be fulfilled is that the filler platelets orient perpendicular to the swelling direction. This can be achieved during the mixing step, by repeatedly calendaring the bulk material in the same direction.

Due to the added organoclay the in-situ process was a successful method to achieve a graded reinforcement in our material. This method could be an attractive way of preparing materials which require high reinforcement at the interface with different media, such as hoses, pipes, and belts. This procedure could increase the quality and life time of the products.

The Profile NMR-MOUSE was a simple and helpful tool to measure the overall relaxation of the material as a function of depth. Using this technique, a gradient could be observed in the swollen material. Complementary to this method, AFM was able to investigate the micromechanical properties of the sample, differentiating between hard area near the surface and in the centre of the material (rich in silica formation), and dispersion of the in-situ silica particles at micron scales.

9. General conclusions

The world as we know it today wouldn't exist without the small contributions that people gave to the society. Such contributions exist since Stone Age. Considering "the wheel" or "electricity" which can be considered milestones in the humankind history that had an enormous impact on the quality of life, nowadays they seem routine. Nothing will move or work without them. Meanwhile the science became so broad and complex that such significant contributions are more and more difficult to make. It is still advancing but with smaller steps as earlier. These steps are known as "patents", scientific publications", or even PhD thesis.

The aim of a PhD is often focused on the importance of the research, which should create a new knowledge in a specific field of interest. Besides that, another objective of a PhD is to develop a graduate student into a competent scientist who can conduct independent research in his/her area of interest.

In this work force-distance curves were acquired on a series of amorphous and semi crystalline polymers. In order to obtain accurate Young's modulus values comparable to the macroscopic values measured by DMA, an improved method to determine microscopic moduli was developed using AFM nanoindentation. The method relies on the proportionality between the contact area of the indentation and the stiffness. While the second (stiffness) can be calculated using an exponential fit to the unloading part of a force-distance curve, the contact area determination is a parameter difficult to estimate. In the past, a model for describing the tip shape, and consequently the contact area of the tip, which is mandatory for the E-modulus calculation, was used. The most common model shapes used for the tip are either conical, or tetragonal pyramidal. In any AFM experimental set-up the tip shape of a

cantilever is likely to suffer changes in its shape. Therefore any theoretical model of the shape of the cantilever tip becomes therefore inaccurate for the calculation. In the present work the tip shape has been experimentally quantified in real time, therefore reducing the uncertainties that aroused from the tip shape.

Introducing an experimentally determined tip area function in the equation for calculating the E-modulus from AFM data yields useful results that correlate well with DMA data. Our method rids the E-modulus equation of an unknown parameter that, until now, had to be estimated. The accuracy of modulus values determined by AFM nanoindentation is considerably increased when experimental data is used to determine the cross-sectional area of the indenter. E-modulus values determined by AFM and DMA then show a high degree of correlation. Nevertheless, with the optimal experimental setup at finite indentation depth, the values measured by AFM are higher than those obtained by means of DMA, although the trend remains the same. Extrapolating the calculated values at zero force, similar moduli – deviating by only about 10% – are obtained for both methods.. To prove that the results are not arbitrary, we showed how the modulus changes with variations in frequency in both the AFM and DMA setups. In each case, the modulus increases with frequency. The use of AFM does not, however, compete with standard DMA tests in the case of modulus determination. DMA is suitable for bulk materials and for probing macroscopic mechanical properties, while AFM measurements are suitable at microscopic scales. The importance of the AFM method is that it improves the accuracy of imaging E-moduli at micro- and even nano-scales, due to the introduction of an experimentally determined tip area function. In this case, heterogeneities at very small scales can be identified, providing information that cannot be obtained with standard physical tests.

It has been showed that the macroscopic modulus is determined by the soft regions from a polymer matrix. Therefore it has been speculated that the microscopic modulus should be determined in the soft areas of the polymer materials in order to get comparable results to the

macroscopic ones. This work shows that the stiff areas represented by the filler agglomerates can also be included in the modulus calculation trough an average curve. Doing so, the modulus obtained trough extrapolation is calculated to be similar to the macroscopic values. Doing a force variation experiment on the two different samples, an increase of the modulus is observed with the increase of the force. However due to the formed heterogeneities in the slow cooled sample, the increase is faster compared to the fast cooled sample.

Different cooling rates lead to modification of the structures observable only at micron and submicron scales. In terms of micromechanical behavior AFM proved to be an adequate tool being able to distinguish between 3 phases from a polymer mixture: high stiffness (filler particle) very low stiffness (polymer), and intermediate stiffness (crystallite) Fig. 7.4. The heterogeneous build up is higher in the slow cooled material (Fig 7.3c), which leads to inhomogeneities in the material. The fast cooled shows a higher homogeneity (Fig. 7.3a).

In the last chapter it was shown that incorporation of the organoclay fillers in the rubber matrix can be a viable way to create so called “barrier materials”. A condition which has to be fulfilled is that the filler platelets orient perpendicular to the swelling direction. This can be achieved during the mixing step, by repeatedly calendaring the bulk material in the same direction. Due to the added organoclay the in-situ process was a successful method to achieve a graded reinforcement in our material. This method could be an attractive way of preparing materials which require high reinforcement at the interface with different media, such as hoses, pipes, and belts. This procedure could increase the quality and life time of the products. The NMR-MOUSE was a simple and helpful tool to measure the overall relaxation of the material as a function of depth. Using this technique, a gradient could be observed in the swollen material. Complementary to this method, AFM was able to investigate the micromechanical properties of the sample, differentiating between hard area near the surface

and in the centre of the material (rich in silica formation), and dispersion of the in-situ silica particles at micron scales.

The characterization of filled EPDM elastomers (crystalline and amorphous) using Atomic Force Microscopy nanoindentation, the development of a new testing method to calculate values of Young's modulus comparable to the macroscopic measured ones, the development of a new material with high perspectives for the rubber industry have contributed to the achievement of the goal of this PhD. Nevertheless, the method to determine Young's modulus that creates spatially resolved measurements to show local mechanical properties at micro- and nanometre scales, places the AFM as an unique tool in this field.

References

1. Goodyear, C., *Improvement in India-rubber fabrics*, in *Letters Patent*, U.S.P. Office, Editor. 1844: USA.

2. Payne, A.R., *The Dynamic Properties of Carbon Black-Loaded Natural Rubber Vulcanizates. Part I.* J. Appl. Polym. Sci., 1962. **6**(19): p. 53-57.

3. Leblanc, J.L., *Rubber-filler interactions and rheological properties in filled compounds.* Progress in Polymer Science, 2002. **27**(4): p. 627-687.

4. Binnig, G., et al., *Surface Studies by Scanning Tunneling Microscopy.* Physical Review Letters, 1982. **49**(1): p. 57-61.

5. Binnig, G., C.F. Quate, and C. Gerber, *Atomic Force Microscope.* Physical Review Letters, 1986. **56**(9): p. 930-933.

6. Binnig, G., et al., *7 x 7 Reconstruction on Si(111) Resolved in Real Space.* Physical Review Letters, 1983. **50**(2): p. 120-123.

7. D.W. Pohl, W. Denk, and M. Lanz., *Optical stethoscopy: Image recording with resolution λ/20.* Applied Physical Letter, 1984. **44**: p. 651.

8. Lewis, A., M. Isaacson, A. Harootunian and A. Murray. , *Development of a 500-A spatial resolution light microscope.* Ultramicroscopy, 1984. **13**: p. 227-232.

9. Cappella, B. and G. Dietler, *Force-distance curves by atomic force microscopy.* Surface Science Reports, 1999. **34**(1â€“3): p. 1-104.

10. Butt, H.-J.r., B. Cappella, and M. Kappl, *Force measurements with the atomic force microscope: Technique, interpretation and applications.* Surface Science Reports, 2005. **59**(1â€“6): p. 1-152.

11. Israelachvili, J.N., *Intermolecular and Surface Forces*. 1992: London: Academic Press.

12. Sader, J.E., et al., *Method for the calibration of atomic force microscope cantilevers.* Review of Scientific Instruments, 1995. **66**(7): p. 3789-3798.

13. Neumeister, J.M. and W.A. Ducker, *Lateral, normal, and longitudinal spring constants of atomic force microscopy cantilevers*. Review of Scientific Instruments, 1994. **65**(8): p. 2527-2531.

14. Kaliappan, S.K., *Characterization of physical properties of polymers using AFM force-distance curves*. 2007.

15. Hutter, J.L. and J. Bechhoefer, *Calibration of atomic-force microscope tips.* Review of Scientific Instruments, 1993. **64**(7): p. 1868-1873.

16. Nakajima, N., *The Science and Practice of Rubber Mixing*. 1999: Rapra Technology Ltd.

17. Ciesielski, A., *An Introduction to Rubber Technology*. 1999: Rapra Technology Ltd.

18. Noordermeer, J.W.M., *Ethylenepropylene polymers*, in *Encyclopedia of Chemical Technology*, K. Othmer, Editor. 1980, Wiley InterScience: New York.

19. T. Meyer, J.K., *Handbook of Polymer Reaction Engineering*. 2005, Weinheim: WILEY-VCH Verlag GmbH & Co. KGaA.

20. Sadhan K. De, J.R.W., *Rubber Technologist's Handbook*. 2001: Rapra Technology Limited.

21. James E. Mark, B.E., Frederick R. Eirich, *The Science and Technology of Rubber, Third Edition*. 2005: Elsevier Inc.

22. *Crosslinking Reagents Technical Handbook*. 2006: Pierce Biotechnology, Inc.

23. Tobolsky, A.V. and P.F. Lyons, *Tensile strength of rubbers.* Journal of Polymer Science Part A-2: Polymer Physics, 1968. **6**(9): p. 1561-1566.

24. Lal, J. and K.W. Scott, *Properties and structure of elastomers.* Journal of Polymer Science Part C: Polymer Symposia, 1965. **9**(1): p. 113-134.

25. Victor M. Litvinov, P.P.D., *Spectroscopy of Rubber and Rubbery Materials*. 2002 Rapra Technology Limited.

26. Donnet, J.-B., *Carbon Black: Science and Technology, Second Edition*. 1993: CRC Press.

27. Addad, J.P.C., *NMR and fractal properties of polymeric liquids and gels.* Progress in Nuclear Magnetic Resonance Spectroscopy, 1993. **25**(13): p. 1-316.

28. Litvinov, V.M. and P.A.M. Steeman, *EPDM - Carbon Black Interactions and the Reinforcement Mechanisms, As Studied by Low-Resolution 1H NMR.* Macromolecules, 1999. **32**(25): p. 8476-8490.

29. Simpson, R.B., *Rubber Basics*. 2002: Rapra Technology Limited.

30. McBrierty, V.J., Kenny, J.C. , Kautsch. Gummi Kunstst., 1994. **47**(5): p. 342.

31. Choi, S.-S., *Difference in bound rubber formation of silica and carbon black with styrene-butadiene rubber.* Polymers for Advanced Technologies, 2002. **13**(6): p. 466-474.

32. Fan, Y.C., *Effect of maleic anhydride on the damping property of magnetorheological elastomers.* Smart Materials and Structures, 2010. **19**(5): p. 055015.

33. Boey, F., *Sample Preparation*, in *Handbook of polymer testing : physical methods*, R. Brown, Editor. 1999: New York.

34. Kashani, M.S. and V. Madhavan, *Analysis and correction of the effect of sample tilt on results of nanoindentation.* Acta Materialia, 2010. **59**(3): p. 883-895.

35. Villarrubia, J.S., *Algorithms for Scanned Probe Microscope Image Simulation, Surface Reconstruction, and Tip Estimation.* J Res Natl Inst Stand Technol, 1997. **102**: p. 425.

36. Jee, A.-Y., & Lee, M., *Comparative analysis on the nanoindentation of polymers using atomic force microscopy.* Polymer Testing, 2010. **29**(1): p. 95-99.

37. Nakajima, K., Watabe, H., J. Soc. Rubber Ind. Jpn., 2006. **79**: p. 466.

38. Vanlandingham, M.R., et al., *Nanoscale Indentation of Polymer Systems Using the Atomic Force Microscope.* The Journal of Adhesion, 1997. **64**(1-4): p. 31-59.

39. Watabe, H., Nakajima, K., *Polimeric Nano-Materials*. 2005, Tokio, Japan.

40. Mermut, O., Lefebvre, Julie , Gray, Derek G. , and Barrett, Christopher J., *Structural and Mechanical Properties of Polyelectrolyte Multilayer Films Studied by AFM.* Macromolecules, 2003. **36**: p. 8819-8824.

41. F. Bedoui, F.S., N.S. Murthy, *Incidence of nanoscale heterogeneity on the nanoindentation of a semicrystalline polymer: Experiments and modeling.* Acta Materialia, 2008: p. 2296–2306.

42. J.K. Deuschle, G.B., H.M. Deuschle, S. Enders, J. Michler, E. Arz, *In situ indentation testing of elastomers.* Acta Materialia, 2008. **56**: p. 4390-4401.

43. Monclus, M., T. Young, and D. Di Maio, *AFM indentation method used for elastic modulus characterization of interfaces and thin layers.* Journal of Materials Science, 2010. **45**(12): p. 3190-3197.

44. Muller, M.K.G., R.H. and Hurley, D.C, Ultramicroscopy, 2006. **106**: p. 466-474.

45. Oliver, W.C., Pharr, G.M., *An improved technique for determining hardness and elastic modulus using load and displacement sensing intentation experiments.* J. Mater. Res., 1992. **7**(6): p. 1564.

46. Bulychev, S.I., Alekhin, V.P. , Zavod. Lab., 1975. **14**: p. 1137.

47. Bulychev, S.I., Alekhin, V.P., Prob. Prochm., 1976. **9**: p. 79.

48. Ternowskii, A.P., Alekhin, V.P. , Zavod. Lab., 1973. **39**: p. 1242.

49. King, R.B., Int. J. Solids Structures, 1987. **23**(12): p. 1657-1664.

50. Jennet, N.M., Meneve, J., *Fundamentals of Nanoindentation and Nanotechnology.* Mater. Res. Soc. Symp. Proc. , 1998. **522**: p. 239.

51. Lucas, B.N., *Thin Films - Stress and Mechanical Properties VII.* Materials Research Society, 1998. **97**.

52. VanLandingham, M.R., Microscopy Today, 1997(97-10): p. 12-15.

53. VanLandingham, M.R., Dagastine, R.R., *Characterization of nanoscale property variations in polymer composite systems: 1. Experimental results.* Composites Part A: Applied Science and Manufacturing, 1999. **30**(1): p. 75-83.

54. Aime, J.P., et al., *Comments on the use of the force mode in atomic force microscopy for polymer films.* Journal of Applied Physics, 1994. **76**(2): p. 754-762.

55. Burnham, N.A., *Interpretation of force curves in force microscopy.* Nanotechnology, 1993. **4**(64).

56. Hues, S.M., Colton, R.J., MRS Bull., 1993. **XVIII**: p. 41.

57. Mizes, H.A., et al., *Submicron probe of polymer adhesion with atomic force microscopy: Dependence on topography and material inhomogeneities.* Applied Physics Letters, 1991. **59**(22): p. 2901-2903.

58. Hues, S.M., C.F. Draper, and R.J. Colton, J. Vacuum Sci. Technol. B, 1994. **12**: p. 2211.

59. Oliver, W.C., et al., *Microindentation Techniques in Materials Science and Engineering*. 1986. 90.

60. Bielinski, D.M., Kautsch. Gummi Kunstst., 2009. **62**: p. 50-54.

61. Herrmann, V., *Characterization of Elastomers using Dynamical Indentations and Comparable Methods*. 2002.

62. Vanlandingham, M.R., et al., *Relating elastic modulus to indentation response using atomic force microscopy.* Journal of Materials Science Letters, 1997. **16**(2): p. 117-119.

63. D.C. Lin, E.K.D., F. Horkay, *Robust strategies for automated AFM force curve analysis - I. Non-adhesive indentation of soft, inhomogeneous materials.* J. Biomech. Eng., 2007. **129**: p. 430–440.

64. Johnson, K.L., *Contact Mechanics*. 1985: Cambridge University Press.

65. Johnson, K.L., K. Kendall, and A.D. Roberts, Proc. Roy. Soc. A, 1971. **324**: p. 301.

66. Calabri, L., Pugno, N. , *AFM nanoindentation: tip shape and tip radius of curvature effect on the hardness measurement.* Journal of Physics: Condensed Matter, 2008. **20**(47): p. 474208.

67. Schlapbach, M.H.a.G.D.a.L., *Mapping the local Young's modulus by analysis of the elastic deformations occurring in atomic force microscopy.* Nanotechnology, 1995. **6**(1): p. 12.

68. Fillers, R.W., Tschoegl, N. W. , Trans. Soc. Rheol., 1977. **21**: p. 51.

69. Binachi, B., Turturro, A. , J. Chem. Phys., 1967. **71**: p. 3555.

70. Quach, A. and R. Simha, *Pressure-Volume-Temperature Properties and Transitions of Amorphous Polymers; Polystyrene and Poly (orthomethylstyrene).* Journal of Applied Physics, 1971. **42**(12): p. 4592-4606.

71. Ferencz, R., et al., *AFM nanoindentation to determine Young's modulus for different EPDM elastomers.* Polymer Testing, 2012. **31**(3): p. 425-432.

72. Sánchez, J.I.M., *Rasterkraftmikroskopie zur Untersuchung von realen polymeren Komposit-Werkstoffen*. 2008: Hannover.

73. Zerda, T.W., et al., *The Effects of Heating and Cooling Rates on the Structure of Carbon Black Particles.* Rubber Chemistry and Technology, 1998. **71**(1): p. 26-37.

74. Khanna, Y.P., *Rheological mechanism and overview of nucleated crystallization kinetics.* Macromolecules, 1993. **26**(14): p. 3639-3643.

75. Uhl, C., *Entwicklung und Charakterisierung von Elastomerkompositen auf Basis neuerer mikro- und nanoskaliger Füllstoffe*. 2007: Dresden.

76. Klüppel, M., Schuster, R. H. , Schaper, J. , *Carbon Black Distribution in Rubber Blends: A Dynamic-Mechanical Analysis.* Rubber Chem. Technol., 1999. **72**: p. 91.

77. Hou, P.P., Cebe, P., J. Polym. Sci. Polym. Phys. Ed., 1992. **30**: p. 1459.

78. Li, L., de Jeu, Wim H. , *Shear-Induced Crystallization of Poly(butylene terephthalate): A Real-Time Small-Angle X-Ray Scattering Study.* Macromolecules, 2004. **37**: p. 5646-5652.

79. Zhao, J., Mascia, L. , *Evolution of Orientation in Polymer Products Produced by Solid State Extrusion.* International Polymer Processing, 1994. **9**(1): p. 60-66.

80. Ben Daly, H., Nguyen, K.T, *The Build-Up and Measurement of Molecular Orientation, Crystalline Morphology, and Residual Stresses in Injection Molded Parts: A Review.* Journal of Injection Molding Technology, 1998. **2**(2).

81. Ben Daly, H., et al., *Effect of polymer properties on the structure of injection-molded parts.* Polymer Engineering & Science, 1999. **39**(9): p. 1736-1751.

82. Nishi, T., Nakajima, K. , *Recent Developments in Rubber Research Using Atomic Force Microscopy*, in *Current Topics in Elastomers Research*, A.K. Bhowmick, Editor. 2008, CRC Press.

83. Hertz, H., *"Über die Berührung fester elastischer Körper".* Journal f. d. reine u. angewandte Mathematik, 1881. **92**: p. 156-171.

84. Hashim, A.S., S. Kohjiya, and Y. Ikeda, *Moisture cure and in-situ silica reinforcement of epoxidized natural rubber.* Polymer International, 1995. **38**(2): p. 111-117.

85. Mark, J.E., J. Appl. Polym. Sci., Appl. Polym. Symp. , 1992. **50**: p. 273.

86. Kohjiya, S., J. Appl. Polym. Sci., 1992. **50**: p. 213.

87. Brinker, J., Scherer, G. W., Sol-Gel Science: The Physics and Chemistry of Sol-Gel Processing; Academic Press, San Diego, 1990: p. 97.

88. Jain, S., Goossens, H., *Synthetic aspects and characterization of polypropylene-silica nanocomposites prepared via solil-state modification and sol-gel reactions.* Polymer, 2005. **46**: p. 6666-6681.

89. Sun, D., Zhang, R., *Polypropylene/Silica nanocomposites prepared by in-situ sol-gel reaction with the aid of CO_2.* Macromolecules, 2005. **38**: p. 5617-5624.

90. Bounor-Legare, V., Angelloz, C., *A new route for organic-inorganic hybrid material synthesis through reactive processing withouth solvent.* Polymer, 2004. **45**: p. 1485-1493.

91. Yoshikai, K., Ohsaki, T., *Silica reinforcement of synthetic diene rubbers by sol-gel process in the latex.* J. Appl. Polym. Sci., 2001. **85**: p. 2053-2063.

92. Poompradub, S., Chaichua, B., *Synthesis of silica in natural rubber solution via sol-gel reaction.* Kautsch. Gummi Kunstst., 2008: p. 152.

93. Ikeda, Y., *Graded styrene-butadiene rubber vulcanizates.* J. Appl. Polym. Sci., 2002. **87**: p. 61-67.

94. Fitzgerald, J.J., Landry C.J.T., *Dynamic studies of the molecular relaxations and interactions in microcomposites prepared by in-situ polymerization of silicon alkoxides.* Macromolecules, 1992. **25**: p. 3715-3722.

95. Clement, F.L., A., *Atomic force microscopy investigation of filled elastomers and comparison with transmission electron microscopy - application to silica-dilled silicone elastomers.* Polymer, 2001. **42**: p. 6259-6270.

96. Rocha, T.L.A.C., Jacobi, M.M., *Evaluation of the influence of the polymer-filler interaction on compounds based on epoxidized elastomeric matrix and precipitated silica.* Polimeros: Ciencia e Technologia, 2006. **16**(2): p. 111-115.

97. Das, A., et al., *Silica-Ethylene Propylene Diene Monomer Rubber Networking by In Situ Sol-Gel Method.* Journal of Macromolecular Science, Part A, 2007. **45**(1): p. 101-106.

98. Das, A., et al., *Routes to Rubber Nanocomposites.* Macromolecular Symposia. **291-292**(1): p. 95-105.

99. Eidmann, G., Savelsberg, R., Blümich, B., *The NMR MOUSE, a mobile universal surface explorer.* Journal of Magnetic Resonance, Series A, 1996. **122**: p. 104-109.

100. Guthausen, G., Guthausen, A., Balibanu, F., Blümich, B., *Soft-matter analysis by the NMR-MOUSE.* Macromol. Mater. Eng. , 2000. **276**.

101. Blümich, B., Blümler, P., Eidmann, G. , *The NMR-MOUSE: construction, excitation and applications.* Magnetic Resonance Imaging, 1998. **16**(5/6): p. 479-484.

102. Perlo, J., Casanova, F., Blümich, B., *Profiles with microscopic resolution by single-sided NMR.* Jorunal of Magnetic Resonance, 2005. **176**: p. 64-70.

103. Blümich, B., Casanova, F., *Mobile NMR*, in *Modern Magnetic Resonance*, G.A. Webb, Editor. 2006, Springer. p. 369-378.

104. Kolz, J., Martins, J., Kremer, K., Blümich, B, *Investigation of the elastomer-foam production with single-sided NMR*. Kautsch. Gummi Kunstst., 2007(April): p. 179-183.

105. Goga, N.O., Demco, D.E., Kolz, J., Ferencz, R., Blümich, B, *Surface UV agigng of elastomers investigated with microscopic resolution by single-sided NMR*. Jorunal of Magnetic Resonance, 2008. **192**(1): p. 1-7.